Cell Reports
Medicine

Article

CYP19A1 mediates severe SARS-CoV-2 disease outcome in males

Graphical abstract

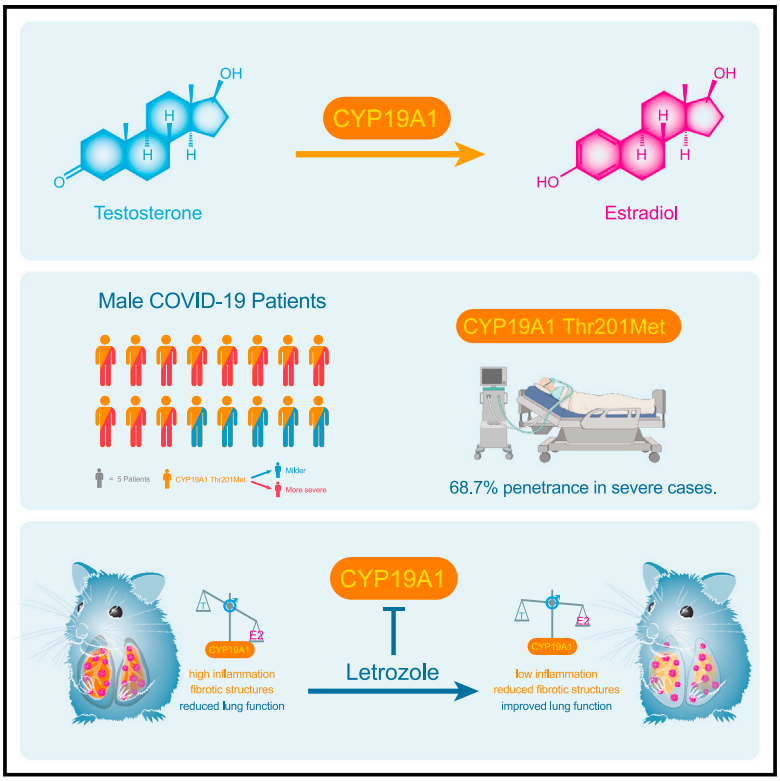

Highlights

- CYP19A1 Thr201Met shows a penetrance of 68.7% in severely ill male COVID-19 patients
- CYP19A1 is highly expressed in the lungs of deceased male COVID-19 patients
- CYP19A1 is associated with sex hormone imbalance in SARS-CoV-2-infected male hamsters
- CYP19A1 inhibition improves long-term lung health in SARS-CoV-2-infected male hamsters

Authors

Stephanie Stanelle-Bertram, Sebastian Beck, Nancy Kouassi Mounogou, ..., GEN-COVID Multicenter Study Group, Alessandra Renieri, Gülsah Gabriel

Correspondence

guelsah.gabriel@leibniz-liv.de

In brief

Stanelle-Bertram et al. identify a CYP19A1-activity-increasing gene variant in male patients with severe COVID-19. Increased pulmonary *CYP19A1* expression is associated with dysregulated sex hormone levels and impaired lung function in SARS-CoV-2-infected male hamsters. The clinically approved CYP19A1 inhibitor letrozole improves long-term lung health in SARS-CoV-2-infected male hamsters.

Stanelle-Bertram et al., 2023, Cell Reports Medicine *4*, 101152
September 19, 2023 © 2023 The Author(s).
https://doi.org/10.1016/j.xcrm.2023.101152

CellPress

Cell Reports Medicine

CellPress
OPEN ACCESS

Article

CYP19A1 mediates severe SARS-CoV-2 disease outcome in males

Stephanie Stanelle-Bertram,[1,31] Sebastian Beck,[1,31] Nancy Kouassi Mounogou,[1,31] Berfin Schaumburg,[1,31] Fabian Stoll,[1] Amirah Al Jawazneh,[1] Zoé Schmal,[1] Tian Bai,[1] Martin Zickler,[1] Georg Beythien,[4] Kathrin Becker,[4] Madeleine de la Roi,[4] Fabian Heinrich,[5] Claudia Schulz,[6] Martina Sauter,[7] Susanne Krasemann,[8,9] Philine Lange,[5] Axel Heinemann,[5] Debby van Riel,[10] Lonneke Leijten,[10] Lisa Bauer,[10] Thierry P.P. van den Bosch,[11] Boaz Lopuhaä,[11] Tobias Busche,[12] Daniel Wibberg,[13] Dirk Schaudien,[14] Torsten Goldmann,[15] Anna Lüttjohann,[1] Jenny Ruschinski,[1] Hanna Jania,[1] Zacharias Müller,[1] Vinicius Pinho dos Reis,[1] Vanessa Krupp-Buzimkic,[1,6] Martin Wolff,[16] Chiara Fallerini,[17,18] Margherita Baldassarri,[17,18] Simone Furini,[17] Katrina Norwood,[19,20] Christopher Käufer,[21] Nina Schützenmeister,[22]

(Author list continued on next page)

[1]Department for Viral Zoonoses - One Health, Leibniz Institute of Virology, Hamburg, Germany
[2]Institute of Virology, University of Veterinary Medicine Hannover, Hannover, Germany
[3]German Center for Infection Research (DZIF), Braunschweig, Germany
[4]Department of Pathology, University of Veterinary Medicine Hannover, Hannover, Germany
[5]Institute of Legal Medicine, University Medical Center Hamburg-Eppendorf, Hamburg, Germany
[6]Research Center for Emerging Infections and Zoonoses, University of Veterinary Medicine Hannover, Hannover, Germany
[7]Institute for Pathology and Neuropathology, University Hospital Tübingen, Tübingen, Germany
[8]Institute of Neuropathology, University Medical Center Hamburg-Eppendorf, Hamburg, Germany
[9]Core Facility Experimental Pathology, University Medical Center Hamburg-Eppendorf, Hamburg, Germany
[10]Department of Viroscience, Erasmus Medical Center, Rotterdam, the Netherlands
[11]Department of Pathology, Erasmus University Medical Center, Rotterdam, the Netherlands
[12]Medical School East Westphalia-Lippe & Center for Biotechnology (CeBiTec), Bielefeld University, Bielefeld, Germany
[13]Microbial Genomics and Biotechnology, Center for Biotechnology (CeBiTec), Bielefeld University, Bielefeld, Germany
[14]Fraunhofer Institute for Toxicology and Experimental Medicine ITEM, Hannover, Germany

(Affiliations continued on next page)

SUMMARY

Male sex represents one of the major risk factors for severe COVID-19 outcome. However, underlying mechanisms that mediate sex-dependent disease outcome are as yet unknown. Here, we identify the *CYP19A1* gene encoding for the testosterone-to-estradiol metabolizing enzyme CYP19A1 (also known as aromatase) as a host factor that contributes to worsened disease outcome in SARS-CoV-2-infected males. We analyzed exome sequencing data obtained from a human COVID-19 cohort (n = 2,866) using a machine-learning approach and identify a CYP19A1-activity-increasing mutation to be associated with the development of severe disease in men but not women. We further analyzed human autopsy-derived lungs (n = 86) and detect increased pulmonary *CYP19A1* expression at the time point of death in men compared with women. In the golden hamster model, we show that SARS-CoV-2 infection causes increased *CYP19A1* expression in the lung that is associated with dysregulated plasma sex hormone levels and reduced long-term pulmonary function in males but not females. Treatment of SARS-CoV-2-infected hamsters with a clinically approved CYP19A1 inhibitor (letrozole) improves impaired lung function and supports recovery of imbalanced sex hormones specifically in males. Our study identifies *CYP19A1* as a contributor to sex-specific SARS-CoV-2 disease outcome in males. Furthermore, inhibition of CYP19A1 by the clinically approved drug letrozole may furnish a new therapeutic strategy for individualized patient management and treatment.

INTRODUCTION

The COVID-19 pandemic has continued to threaten the human population since its first emergence in China. To date, approximately 764 million people have been infected and ~6.8 million have died worldwide since the pandemic declaration on March 11, 2020 (as of July 2023).[1] Retrospective analysis of epidemiologic data has revealed that male sex, older age, and underlying

This is an open access article under the CC BY-NC-ND license (http://creativecommons.org/licenses/by-nc-nd/4.0/).

Maren von Köckritz-Blickwede,[6,23] Maria Schroeder,[24] Dominik Jarczak,[24] Axel Nierhaus,[24] Tobias Welte,[25,26] Stefan Kluge,[24] Alice C. McHardy,[3,19,20,27] Frank Sommer,[28] Jörn Kalinowski,[13] Susanne Krauss-Etschmann,[16,29] Franziska Richter,[21] Jan von der Thüsen,[11] Wolfgang Baumgärtner,[4] Karin Klingel,[7] Benjamin Ondruschka,[5] GEN-COVID Multicenter Study Group, Alessandra Renieri,[17,18,30] and Gülsah Gabriel[1,2,3,32,*]

[15]Pathology of the University Medical Center Schleswig-Holstein, Campus Lübeck and the Research Center Borstel, Research Center Borstel, Leibniz Center for Medicine and Biosciences, German Center for Lung Research (DZL), Borstel, Germany
[16]Early Life Origins of Chronic Lung Disease, Research Center Borstel, Leibniz Lung Center, Member of the German Center for Lung Research (DZL), Borstel, Germany
[17]Med Biotech Hub and Competence Center, Department of Medical Biotechnologies, University of Siena, Siena, Italy
[18]Medical Genetics, University of Siena, Siena, Italy
[19]Department for Computational Biology of Infection Research, Helmholtz Center for Infection Research, Braunschweig, Germany
[20]Braunschweig Integrated Centre of Systems Biology (BRICS), Technische Universität Braunschweig, Braunschweig, Germany
[21]Department of Pharmacology, Toxicology, and Pharmacy, University of Veterinary Medicine Hannover, Hannover, Germany
[22]Department of Pharmaceutical Sciences, University of Vienna, Vienna, Austria
[23]Department of Biochemistry, University of Veterinary Medicine Hannover, Hannover, Germany
[24]Department of Intensive Care Medicine, University Medical Center Hamburg-Eppendorf, Hamburg, Germany
[25]Department of Respiratory Medicine, Hannover Medical School, Hannover, Germany
[26]Biomedical Research in Endstage and Obstructive Lung Disease, Member of the German Center for Lung Research, Hannover, Germany
[27]Cluster of Excellence RESIST (EXC 2355), Hannover Medical School, Hannover, Germany
[28]Division Men's Health, University Medical Center Hamburg-Eppendorf, Hamburg, Germany
[29]Institute for Experimental Medicine, Christian-Albrechts-Universität zu Kiel, Kiel, Germany
[30]Genetica Medica, Azienda Ospedaliero-Universitaria Senese, Siena, Italy
[31]These authors contributed equally
[32]Lead contact
*Correspondence: guelsah.gabriel@leibniz-liv.de
https://doi.org/10.1016/j.xcrm.2023.101152

metabolic diseases such as obesity pose high risks for fatal COVID-19.[2–6] Increased COVID-19 case-fatality rate in males is not reflected by increased incidence compared to females.[3,4,7] Thus, it is unlikely that male prevalence in COVID-19 mortality can be explained by elevated susceptibility to viral infection.

Factors that mediate sex disparity in COVID-19 outcome might include a complex interaction of biological sex differences (e.g., genes, sex hormones) and/or gender aspects (e.g., social behavior).[6,8] Sex differences of genetic origin are constant throughout life irrespective of age or comorbidity. Sex differences involving sex hormones (e.g., testosterone, estradiol) are dynamic and may change with increasing age and/or metabolic comorbidities.[9]

Several independent studies highlighted that men hospitalized with COVID-19 present testosterone levels significantly below age-adjusted reference values.[10–13] Moreover, low testosterone levels were repeatedly reported in independent cohorts to present a poor prognostic marker in COVID-19 males.[10,12–14] In general, low testosterone levels were associated with the highest risks of requiring mechanical ventilation, intensive care unit (ICU) admission, or fatal outcome in several independent studies.[10,13] However, after recovery from COVID-19, total testosterone levels increased over time in men, although at 7-month follow-up ~50% still had testosterone levels below healthy reference values.[14] Moreover, 1 year later ~30% of men who recovered from COVID-19 still showed low testosterone levels suggesting manifesting hypogonadism.[15] Long-term hypogonadism in men is associated with elevated morbidity and mortality in general, also independently of COVID-19,[16] which, however, seems to induce and promote sustained hypogonadism. This hypothesis is further strengthened by studies reporting that recovery from hypogonadism is strongly associated with COVID-19 survival in male patients, while failure to reinstate physiological testosterone levels is associated with COVID-19 death.[17] In some studies where the assessed hormone profile also included the measurement of additional hormones, low testosterone levels were reported to be associated with elevated estradiol levels in parallel, which were both predictive of ICU admission and extracorporeal membrane oxygenation treatment in COVID-19 men.[11,13] Thus, there is increasing evidence that dysregulated sex hormone levels are associated with COVID-19 sex disparities. However, underlying mechanisms, as well as the nature of their involvement being either associative or causal, remain elusive.

Sex hormones may act as important regulators of host cell immunity and exert functions far beyond reproduction. Intracellular androgen and estrogen receptors act as transcription factors by binding to hormone response elements of many genes, thereby regulating cell responses to various environmental changes. Cell-surface-bound androgen and estrogen receptors may additionally affect host responses. Both intracellular and cell-surface-mediated sex hormone receptors may upon activation affect local cell-to-cell signaling (paracrine effects) or systemic hormone signaling pathways via the blood system (endocrine effects).[18]

In the last decades, evidence has grown that sex hormones play a pivotal role in lung health. Sex differences are known in various lung diseases, such as asthma, chronic obstructive pulmonary disease, and pulmonary fibrosis.[19] Research in preterm neonates, where respiratory distress is one of the major causes of death, highlighted a protective role of androgens in lung development.[20] Conversely, clinical and experimental studies identified an inflammatory function for estrogens and their metabolites, such as estradiol.[5,21] Physiological changes in sex hormone levels, such as those occurring during the menstrual cycle,

CellPress
OPEN ACCESS

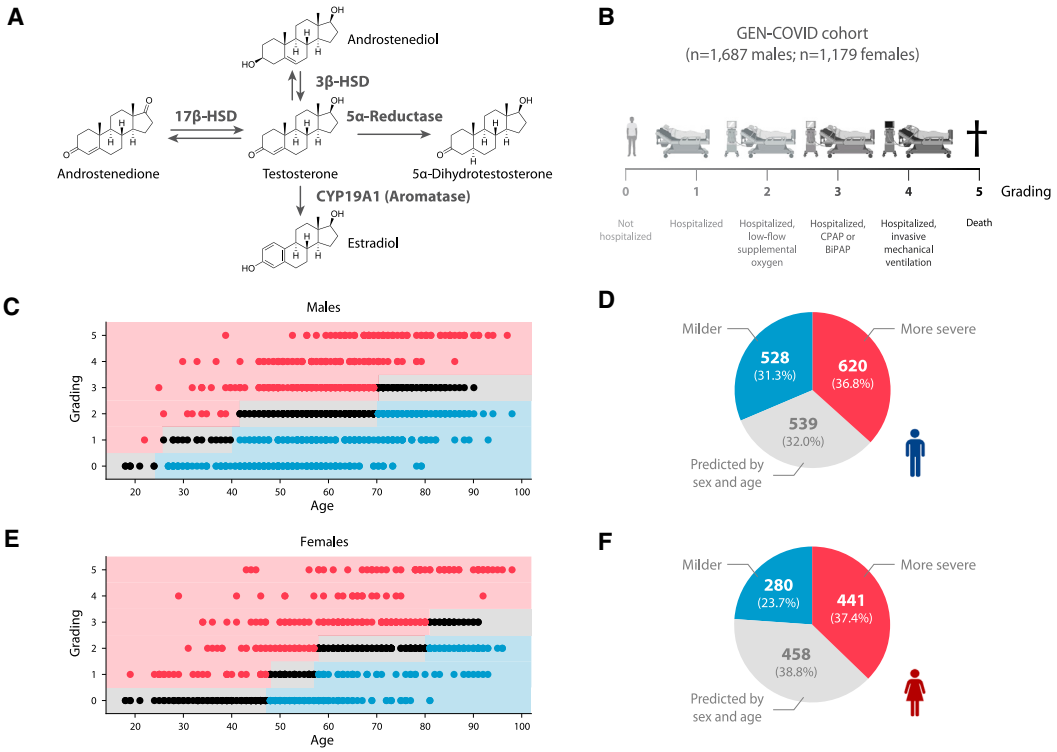

G

Sex	Polymorphism	Genotype	More severe	Milder	Odds Ratio	p-value
Male	CYP19A1 Thr201Met	Met/Met and Thr/Met	55	25	1.96 [1.2-3.16] **	0.006
		Thr/Thr	565	503		
Female	CYP19A1 Thr201Met	Met/Met and Thr/Met	35	19	1.18 [0.66-1.51]	0.567
		Thr/Thr	406	261		
Male	HSD17B1 Gly313Ser	Ser/Ser and Gly/Ser	446	367	1.01 [0.79-1.29]	0.924
		Gly/Gly	215	179		
Female	HSD17B1 Gly313Ser	Ser/Ser and Gly/Ser	343	196	1.02 [0.75-1.39]	0.892
		Gly/Gly	161	94		
Male	SRD5A1 Ala39Gly	Gly/Gly and Ala/Gly	515	403	1.32 [1.02-1.72] *	0.038
		Ala/Ala	142	147		
Female	SRD5A1 Ala39Gly	Gly/Gly and Ala/Gly	397	240	0.77 [0.53-1.11]	0.174
		Ala/Ala	107	50		

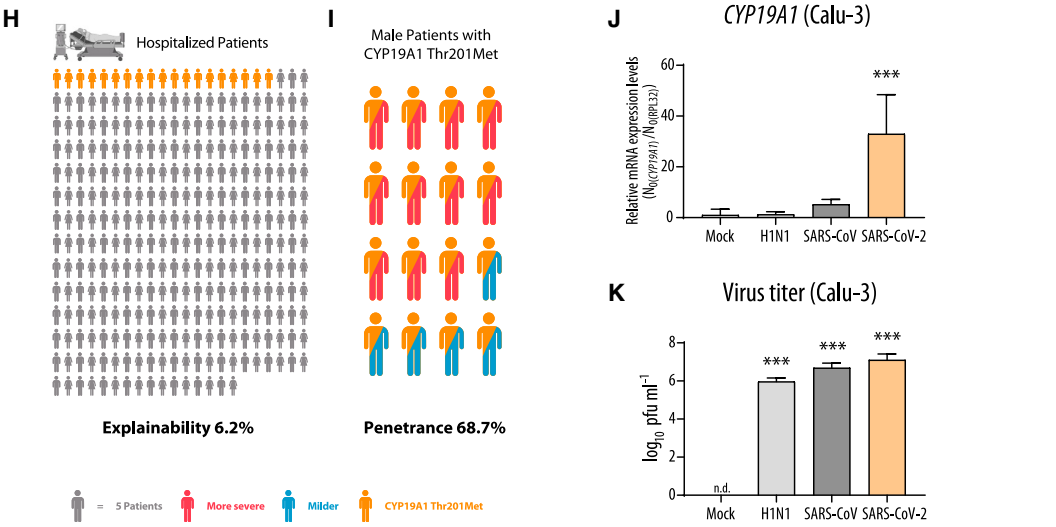

(legend on next page)

pregnancy, and menopause, were associated with changes in lung function.[22,23]

In this study, we sought to identify molecular pathways involved in sex disparities in COVID-19. Therefore we analyzed, in a sex-dependent fashion, whole-exome sequences from large human COVID-19 cohorts to look for alterations in key enzymes involved in sex hormone metabolism. Furthermore, we quantified expression levels of the identified major sex hormone metabolizing enzyme in the lungs of patients who died of COVID-19. Seeking for causalities, we used the golden hamster model as a widely validated preclinical small animal model to study SARS-CoV-2 pathogenesis. As a result, combining human and animal data, we identified CYP19A1 (the testosterone-to-estradiol converting enzyme) as a crucial factor of severe disease outcome upon SARS-CoV-2 infection in males. Treatment of SARS-CoV-2-infected animals with the clinically approved CYP19A1 inhibitor letrozole improved long-term lung health in males, suggesting letrozole as a promising drug candidate for further assessment regarding individualized therapy in humans.

RESULTS

CYP19A1-activity-increasing mutation Thr201Met is associated with the development of severe COVID-19 in male patients

There is ample clinical evidence that low plasma testosterone levels pose a poor prognostic marker for men diagnosed with COVID-19.[11–14,17] However, mechanistic insights into how SARS-CoV-2 infection is associated with testosterone dysregulation in males are lacking. Low testosterone levels may result, for example, from alterations in its direct metabolism that involves major key enzymes. Testosterone is metabolized from its precursors androstenedione or androstenediol by 17β-hydroxysteroid dehydrogenase (17β-HSD) and 3β-HSD, respectively. Testosterone is further metabolized to 5α-dihydrotestosterone by 5α-reductase or is converted to the female sex hormone estradiol by CYP19A1 (also known as aromatase) (Figure 1A). Polymorphisms in these testosterone-metabolizing enzymes were previously reported as leading to low circulating testosterone levels in men.[24–27] Thus, we hypothesized that variations in testosterone metabolic pathways may affect sex-dependent COVID-19 outcome.

To test this hypothesis, we analyzed human exome data obtained from 2,866 SARS-CoV-2-positive male and female patients (GEN-COVID; https://sites.google.com/dbm.unisi.it/gen-covid)[28] regarding polymorphisms in the genes *17β-HSD*, *3β-HSD*, *5α-Reductase*, and *CYP19A1* involved in testosterone metabolism (Figure 1A). We applied a machine-learning approach in combination with a Boolean representation of whole-exome sequencing (WES) data as described previously[28,29] to predict COVID-19 severity defined according to World Health Organization criteria (Figure 1B), which are further presented for males (Figures 1C and 1D) and females (Figures 1E and 1F). One low-frequency (minor allele frequency [MAF] from 1% to 5%) variant Thr201Met and two common (MAF >5%) variants (Gly313Ser and Ala39Gly, respectively) in CYP19A1, HSD17B1, and SRD5A1 genes, all involved in testosterone metabolism, appeared among the features used by the model to predict severity after adjusting for age. Among the variants within these genes, the SRD5A1 Ala39Gly and the CYP19A1 Thr201Met variant were significantly associated with COVID-19 severity in males compared to females. However, the CYP19A1 Thr201Met variant showed the strongest association with COVID-19 severity with an odds ratio of 1.96 in males (95% confidence interval, 1.2–3.16; p value, 0.006) (Figure 1G).

Overall, the Thr201Met variant is expected to contribute to severe COVID-19 in up to 6.2% of all hospitalized male and female patients (Figure 1H). Remarkably, in male patients, the Thr201Met variant showed a calculated penetrance under a monogenic model of 68.7% (Figure 1I). The Thr201Met variant in *CYP19A1* was previously described to increase CYP19A1 enzyme (aromatase) activity in general, resulting in enhanced metabolism of testosterone to estradiol.[30]

In summary, analysis of human genetic data strongly suggest that particularly male patients who carry the CYP19A1 (aromatase)-activity-increasing variant Thr201Met, irrespective of age or other confounders, have a high risk of developing severe COVID-19.

SARS-CoV-2 infection increases *CYP19A1* transcription in lung cell cultures

We next sought to assess whether the expression of the *CYP19A1* gene, in addition to the identified genetically fixed *CYP19A1*-activity-increasing mutation, might be additionally affected by viral infection. This would suggest that besides a fixed genetic component, another dynamic component, such as viral infection, could further affect CYP19A1 function. To assess this hypothesis, we infected human lung cells (Calu-3)

Figure 1. Association analysis of *CYP19A1* gene variation in whole-exome sequencing data of the GEN-COVID cohort

(A) Overview of testosterone metabolism.

(B) Characteristics and COVID-19 severity grading of the GEN-COVID cohort (n = 2,866 patients).

(C and E) Ordered logistic regression (OLR) model in male (C) and female (E) patients, fitted using age to predict the ordinal grading (0, 1, 2, 3, 4, 5) dependent variable. Subjects falling above (severe), below (mild), or matching (intermediate) the expected treatment outcomes according to age are shown as red, blue, and black dots, respectively.

(D and F) Pie charts representing the number of male (D) and female (F) patients falling into "milder," "more severe," and "predicted by sex and age" categories.

(G) Association analysis between low frequency and common variants present in genes involved in testosterone metabolism and COVID-19 severity.

(H and I) Graphical presentation of explainability (H) and penetrance (I) under a monogenic model for the Thr201Met CYP19A1 variant.

(J and K) *CYP19A1* mRNA expression levels (J) and virus titers (K) in Calu-3 cells control-treated (Mock) or infected with H1N1 influenza A virus, SARS-CoV, and SARS-CoV-2 (multiplicity of infection = 0.5) at 24 h post infection (p.i.). A merge of three independent biological replicates, performed in technical triplicates, is shown. Relative *CYP19A1* mRNA expression values in mock-treated cells were set to n.d. (not detectable).

Values are shown as means; error bars are shown as SD. In (G), (J), and (K) statistical significance was assessed by chi-squared test or one-way ANOVA showing significant differences between mock and infected cells (*$p \leq 0.05$, **$p < 0.01$, ***$p < 0.001$).

CellPress
OPEN ACCESS

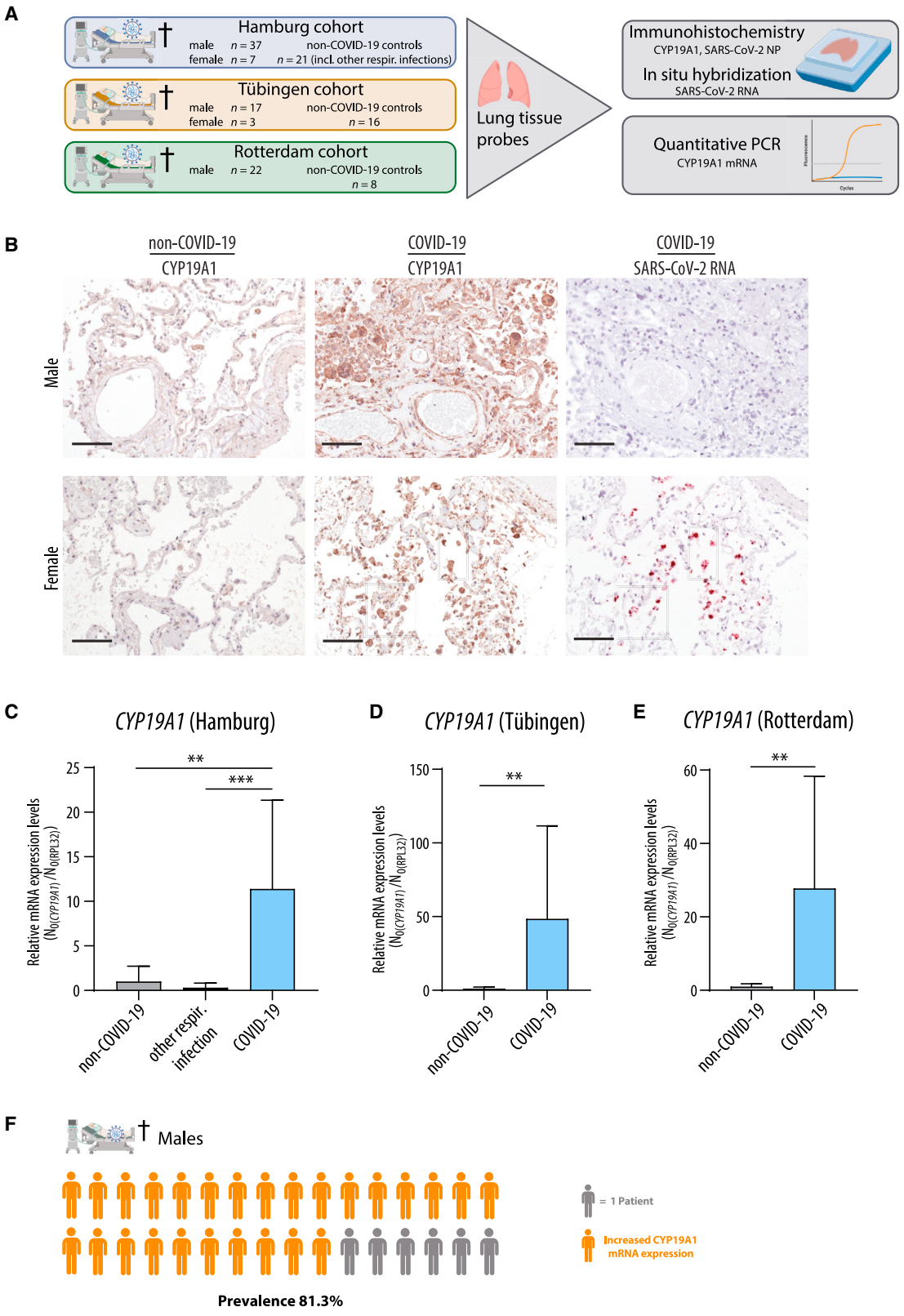

(legend on next page)

with SARS-CoV-2 or with SARS-CoV or H1N1 influenza A virus as controls. *CYP19A1* mRNA expression was increased up to ~40-fold in SARS-CoV-2-infected cells but not in SARS-CoV-infected or H1N1 influenza virus-infected lung cells (Figure 1J), despite similar replication efficacies (Figure 1K).

This finding indicates that SARS-CoV-2 has evolved specific mechanisms not observed in its ancestor or an unrelated respiratory pathogen to upregulate *CYP19A1* expression in the lung, which could increase the risk for severe disease outcome in addition to the presence of CYP19A1-activity-increasing mutations detected in COVID-19 patients.

CYP19A1 mRNA is highly expressed in autopsy-derived lung tissues of male COVID-19 patients

To assess whether increased *CYP19A1* transcription can also be detected in SARS-CoV-2-infected patients, we analyzed autopsy-derived lung material from males and females who died of COVID-19 (n = 86). Therefore, we used three independent study sites for autopsies (Figure 2A). As controls, we analyzed lung material obtained from men and women who were never diagnosed positive for SARS-CoV-2 by qRT-PCR but were diagnosed to have died of other respiratory infections ("other resp. infection") or for other reasons ("non-COVID-19").

At all three study sites (Hamburg, Tübingen, and Rotterdam), CYP19A1 was abundantly expressed in the lungs of COVID-19 males compared to those who died of other respiratory infections or other reasons not related to COVID-19 (Figures 2B–2E). In COVID-19 females, only in two cases was CYP19A1 expression detectable in cells that were still positive for SARS-CoV-2 antigen or RNA (Figure 2B and data not shown). However, owing to the overall very low number of female COVID-19 cases, conclusive interpretation regarding CYP19A1 expression in the female lung is not entirely possible.

In general, CYP19A1 was expressed in epithelial and endothelial cells but most profoundly in macrophages at all three independent study sites. Consecutive staining of the dissected lungs revealed still highly CYP19A1-expressing macrophages in COVID-19 males, albeit SARS-CoV-2 antigen and RNA was expressed at low levels or was no longer detectable at the time point of death (Figure 2B). On the other hand, consecutive staining in COVID-19 females shows SARS-CoV-2 RNA-positive macrophages overlaid with CYP19A1-expressing macrophages (Figure 2B). Quantification of *CYP19A1* mRNA levels revealed a transcriptional increase up to ~10-fold in the male COVID-19 Hamburg cohort, up to ~50-fold in the lungs of deceased COVID-19 males in the Tübingen cohort, and up to ~20-fold in the male COVID-19 Rotterdam cohort (Figures 2C–2E).

These findings show that *CYP19A1* is abundantly expressed on the mRNA and protein level in the lungs of men who died of COVID-19, with a prevalence of 81.3% (Figure 2F). Thus, CYP19A1 expression seems to be still persisting at the time of death, even when most of the virus is already cleared from the lung.

CYP19A1 transcription is highly induced upon SARS-CoV-2 infection in the lung and lung macrophages of male hamsters

CYP19A1 is localized in the endoplasmic reticulum and is expressed in a wide range of tissues, including epithelial cells, endothelial cells, the vascular wall, and macrophages, in various mammalian species.[31–33] The *CYP19A1* gene contains predicted binding sites for key transcription factors, e.g., nuclear factor κB and STAT1, -3, -4, and -6 (Figure 3A). In addition, the *CYP19A1* promoter contains binding sites for sex-hormone-responsive elements, e.g., the androgen receptor (AR), estrogen receptors (ESR-α/-β), and progesterone receptors (PR-α/-β).[34–38] (Figure 3A). To study possible causalities between CYP19A1 and COVID-19, we used the golden hamster model to mimic key aspects of COVID-19.

First, we assessed CYP19A1 expression in the lungs of male and female golden hamsters. We detected increased CYP19A1 protein expression in the male lung compared to the female lung (Figures 3B and S1), in line with previous reports that CYP19A1 is expressed more abundantly in males than in females.[39] Next, we infected male and female hamsters with the same virus dose, using the moderate COVID-19 model in golden hamsters.[40,41] During the first 6 days of acute infection, weight loss was comparable between males and females (Figure 3C). However, during the recovery phase from day 7 until day 14 post infection (p.i.), infected males recovered more slowly than females. While infected females regained their initial weight on day 14 p.i., infected males still showed reduced body weight (Figure 3C).

In the lungs of SARS-CoV-2-infected male hamsters, *CYP19A1* transcription increased up to ~15-fold compared to animals treated with the immunostimulant poly(I:C) or PBS as control at day 3 p.i. (Figure 3D). In the lungs of virus-infected hamsters, cytokines and chemokines were generally induced to similar levels in both sexes (Figure S2). In lung macrophages isolated from uninfected male hamsters, we were able to induce IL-6 expression upon *ex vivo* poly(I:C) treatment as detected in SARS-CoV-2-infected lungs (Figures 3E and S3). In line with this, IL-6 induction correlated with *CYP19A1* mRNA expression in a poly(I:C)-concentration-dependent manner in male lung

Figure 2. *CYP19A1* expression in the lungs of fatal COVID-19 cases

(A) Experimental setup for detecting *CYP19A1* protein and mRNA expression levels in deceased COVID-19 patients and controls from three different study sites.
(B) Detection of CYP19A1 protein expression (immunohistochemistry) and SARS-CoV-2 RNA (*in situ* hybridization) in the lungs from deceased male and female COVID-19 patients or non-COVID-19 controls (representative pictures shown from the University Hospital Tübingen cohort). Scale bars, 100 μm.
(C–E) *CYP19A1* mRNA expression levels in the lungs of deceased male COVID-19 patients, non-COVID-19 controls, and/or deceased patients with other respiratory infections at the University Hospital Hamburg-Eppendorf (C) (non-COVID-19, n = 3; other respiratory infections, n = 11; COVID-19, n = 12), at the University Hospital Tübingen (D) (non-COVID-19, n = 8; COVID-19, n = 9), and at the Erasmus Medical Center Rotterdam (E) (non-COVID-19, n = 4; COVID-19, n = 11). Relative *CYP19A1* mRNA expression values in non-COVID-19 males were set to 1. Values are shown as means; error bars are shown as SD. Statistical significance was assessed by Mann-Whitney test (**p < 0.01, ***p < 0.001).
(F) Visualization of percentage of males who died of COVID-19 with increased pulmonary *CYP19A1* expression at the time of death.

CellPress
OPEN ACCESS

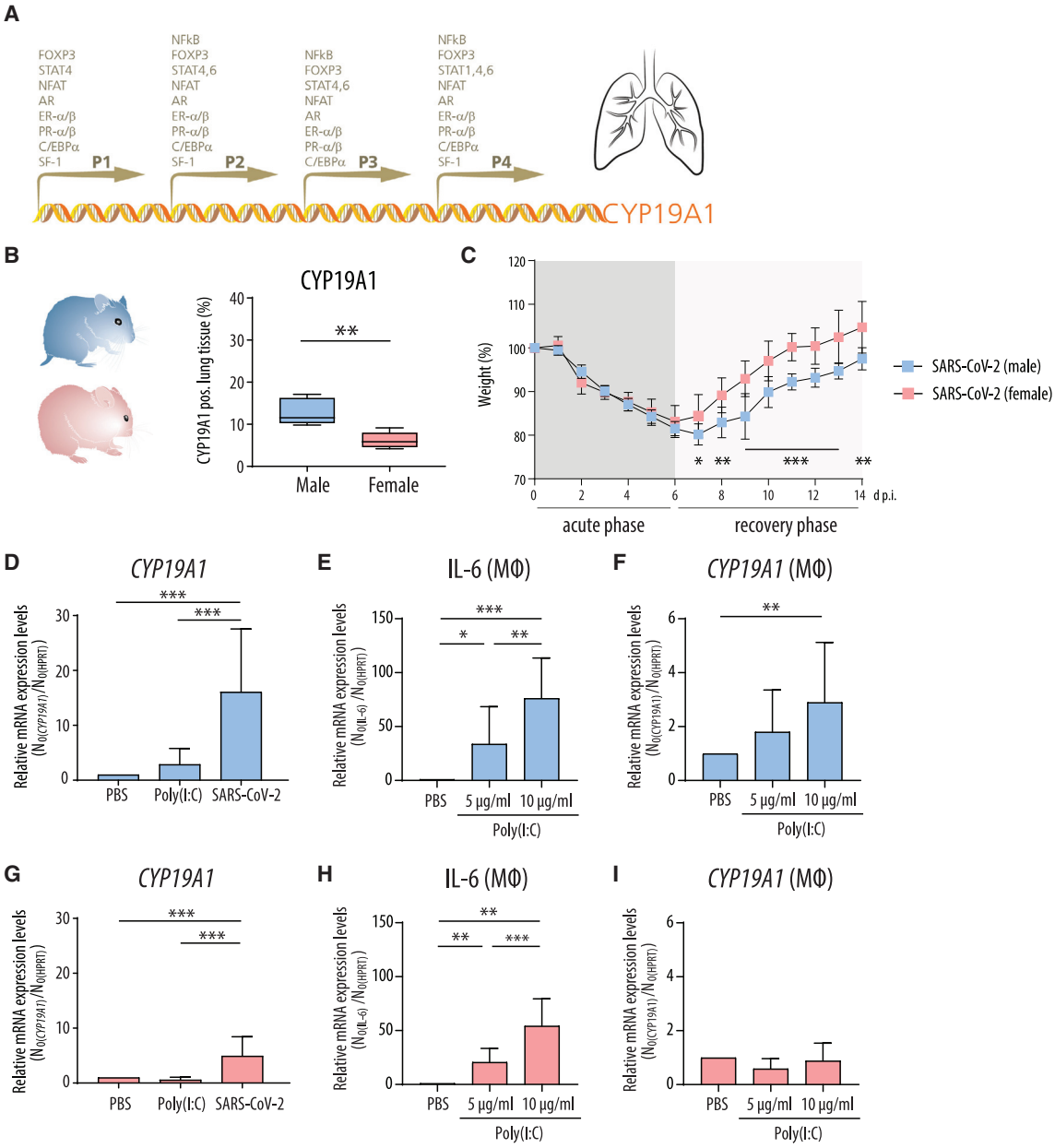

Figure 3. *CYP19A1* expression in the lung of SARS-CoV-2-infected hamsters

(A) Binding sites for transcription factors in the four promoter regions (P1, P2, P3, and P4) of the *CYP19A1* gene.

(B) Quantification of CYP19A1-expressing tissue in the lungs of control-treated (PBS) male and female hamsters (n = 5). Data are shown as a box-and-whisker plot.

(C) Weight loss of male and female hamsters infected with SARS-CoV-2 (n = 10).

(D and G) *CYP19A1* mRNA expression levels measured at day 3 p.i. in the lungs of SARS-CoV-2-infected and control-treated (PBS, Poly(I:C)) male (D) and female (G) golden hamsters (n = 10).

(E, F, H, and I) IL-6 (E and H) and *CYP19A1* (F and I) mRNA expression levels in lung macrophages isolated from uninfected male (E and F) or female (H and I) hamsters upon *ex vivo* PBS or Poly(I:C) treatment (male, n = 11; female, n = 8). Relative mRNA expression values in PBS-treated hamsters or macrophages were set to 1.

Values are shown as means; error bars are shown as SD. Statistical significance was assessed by Mann-Whitney test, unpaired/paired Student's t test, or one-way ANOVA (*$p \leq 0.05$, **$p < 0.01$, ***$p < 0.001$).

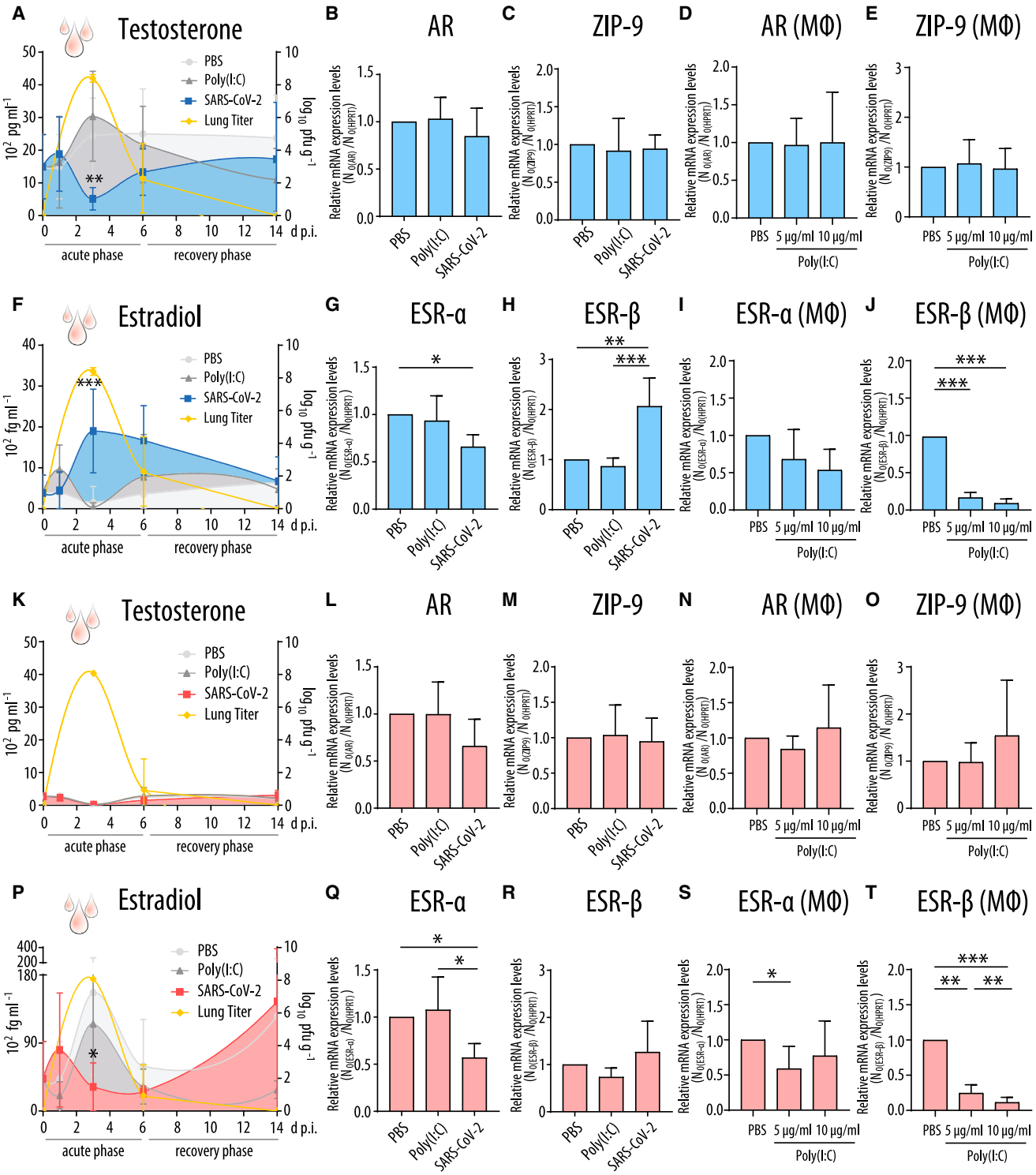

Figure 4. Sex hormones and sex hormone receptor expression in SARS-CoV-2-infected lungs as well as lung macrophages of hamsters

(A, F, K, and P) Testosterone (A and K) and estradiol (F and P) were measured at the indicated time points in SARS-CoV-2-infected or control-treated (PBS, Poly(I:C)) male (A and F) and female (K and P) hamsters (n = 5; day 3 p.i., n = 5–10).

(B, C, G, H, L, M, Q, and R) Androgen receptor (AR) (B and L), zinc transporter 9 (ZIP-9) (C and M), estrogen receptor α (ESR-α) (G and Q), and estrogen receptor β (ESR-β) (H and R) mRNA expression in the lungs of SARS-CoV-2-infected and control-treated (PBS, Poly(I:C)) male (B, C, G, H) and female (L, M, Q, R) hamsters at day 3 p.i. (n = 5; Poly(I:C), n = 4–5).

(legend continued on next page)

macrophages (Figures 3F and S3). In lungs of female hamsters infected with SARS-CoV-2, *CYP19A1* transcription increased up to ~5-fold compared to uninfected females on day 3 p.i. (Figure 3G). In lung macrophages isolated from uninfected females, we were able to induce IL-6 upon *ex vivo* poly(I:C) treatment in a concentration-dependent manner similarly to males (Figure 3H). However, *CYP19A1* transcription could not be induced in female lung macrophages treated with poly(I:C).

These data suggest that SARS-CoV-2 infection specifically induces *CYP19A1* transcription in the male lung while not affecting the expression of other testosterone-converting enzymes (Figure S4). Additional controls, using cells of non-respiratory origin, further strengthened the hypothesis that SARS-CoV-2 infection upregulates *CYP19A1* transcription exclusively in the respiratory tract (Figure S5).

Increased respiratory *CYP19A1* transcription is associated with low testosterone and high estradiol levels in the plasma of SARS-CoV-2-infected male hamsters

To assess whether differential *CYP19A1* induction in the lungs of SARS-CoV-2-infected animals is associated with alterations in circulating sex hormone levels, we quantified testosterone and estradiol levels in the plasma of male and female hamsters at various time points after viral infection.

In infected male hamsters, testosterone levels dropped on day 3 p.i. compared to levels prior to infection by 5-fold, started to recover on day 6 p.i., and were fully recovered on day 14 p.i. compared to males treated with poly(I:C) or PBS (Figure 4A). Virus replication in the male lungs was negatively associated with testosterone levels. Expression of androgen receptors (AR, ZIP-9) was not affected in the lungs of SARS-CoV-2-infected male hamsters on day 3 p.i. or in poly(I:C)-stimulated lung macrophages as compared to controls (PBS, poly(I:C)) (Figures 4B–4E). Conversely, estradiol levels increased in the plasma of infected male animals on day 3 p.i. compared to PBS-treated groups by 13-fold, remained elevated on day 6 p.i., and had mostly recovered on day 14 p.i. (Figure 4F). Estradiol levels were positively associated with virus titers in the lung. Estrogen receptor (ESR-α, ESR-β) expression was significantly changed in virus-infected groups. ESR-α expression was slightly reduced and ESR-β was strongly induced in the lungs of male hamsters upon SARS-CoV-2 infection (Figures 4G and 4H). In lung macrophages of male hamsters, ESR-α levels were not affected, while ESR-β expression was strongly reduced (Figures 4I and 4J).

In infected female hamsters no significant alteration in plasma testosterone levels was detected, in line with the physiologically very low levels of testosterone in young female hamsters as expected (Figure 4K). High virus titers were detected on day 3 p.i. in females, comparable to the virus dynamics detected in males. No alterations in the expression of the androgen receptors AR and ZIP-9 were detected (Figures 4L–4O). Estradiol levels, however, were reduced in SARS-CoV-2-infected female hamsters by 5-fold compared to the respective PBS control group (Figure 4P). Virus titers were negatively associated with estradiol levels in infected female hamsters on day 3 p.i. Estrogen receptor ESR-α expression was reduced in SARS-CoV-2-infected female lungs, while ESR-β expression levels were not affected (Figures 4Q and 4R). In poly(I:C)-treated lung macrophages, ESR-α expression was slightly reduced and ESR-β expression strongly reduced (Figures 4S and 4T).

These findings support the concept that SARS-CoV-2 infection causes dysregulated sex hormone levels in the plasma and ESR-β expression patterns in the lung of male hamsters.

Dysregulated sex hormone metabolism is associated with prolonged respiratory dysfunction in SARS-CoV-2-infected male hamsters

Sex hormones were repeatedly shown to affect lung health.[19–23] Thus, we next measured respiratory function longitudinally in SARS-CoV-2-infected male and female hamsters (Figures 5 and S6).

Respiratory function was more severely impaired in infected males compared to females on day 6 p.i. In both sexes, the tidal volume was reduced on day 6.p.i., which persisted in males until day 14 p.i. (Figures 5A and 5B). Male hamsters compensated this deficit by a higher breathing frequency, resulting in a normal ventilation rate (Figures 5A, 5C, and S6A). In contrast, the breathing frequency remained normal in females that showed a similarly reduced tidal volume as males at the cost of a slightly reduced ventilation rate (Figures 5B, 5D, and S6B). In line with restrictive lung disease, the expiratory flow was enhanced in male hamsters while their inspiratory flow was reduced (Figures 5E, 5G, and 5I). These changes remained visible in part until day 14 p.i. (Figures 5 and S6). Again, infected female hamsters had a normal expiratory flow with a reduction in inspiratory flow only (Figures 5F, 5H, and 5J). Inspiratory and expiratory pauses were shortened in both males and females (Figures S6C–S6F).

Taken together, the results of the comprehensive lung function tests show that SARS-CoV-2-infected female hamsters recover on day 14 p.i. In contrast, infected male hamsters still present an impaired respiratory capacity on day 14 p.i. accompanied by local fibrotic structures (Figure S7).

CYP19A1 inhibitor letrozole improves lung health in SARS-CoV-2-infected male hamsters

Next, we sought to understand whether CYP19A1 acts causally on overall lung health. First, we treated human lung cells (Calu-3) with testosterone in presence or absence of the clinically approved CYP19A1 inhibitor letrozole, followed by infection with SARS-CoV-2 before finally measuring estradiol in the supernatant. Thereby, we confirmed an increase in estradiol levels in the cell supernatant after SARS-CoV-2 infection. Letrozole treatment was able to reverse this effect by significantly reducing estradiol levels in the supernatant (Figure S8). These findings

(D, E, I, J, N, O, S, and T) AR (D and N), ZIP-9 (E and O), ESR-α (I and S), and ESR-β (J and T) mRNA expression in lung macrophages isolated from uninfected male (D, E, I, J) and female (N, O, S, T) hamsters (n = 8–11) upon *ex vivo* PBS or Poly(I:C) treatment.
In (B–E), (G–J), (L–O), and (Q–T), relative hormone receptor mRNA expression values in PBS-treated controls were set to 1. Values are shown as means; error bars are shown as SD. Statistical significance was assessed by one-way ANOVA or paired Student's t test (*p $\leq$ 0.05, **p < 0.01, ***p < 0.001).

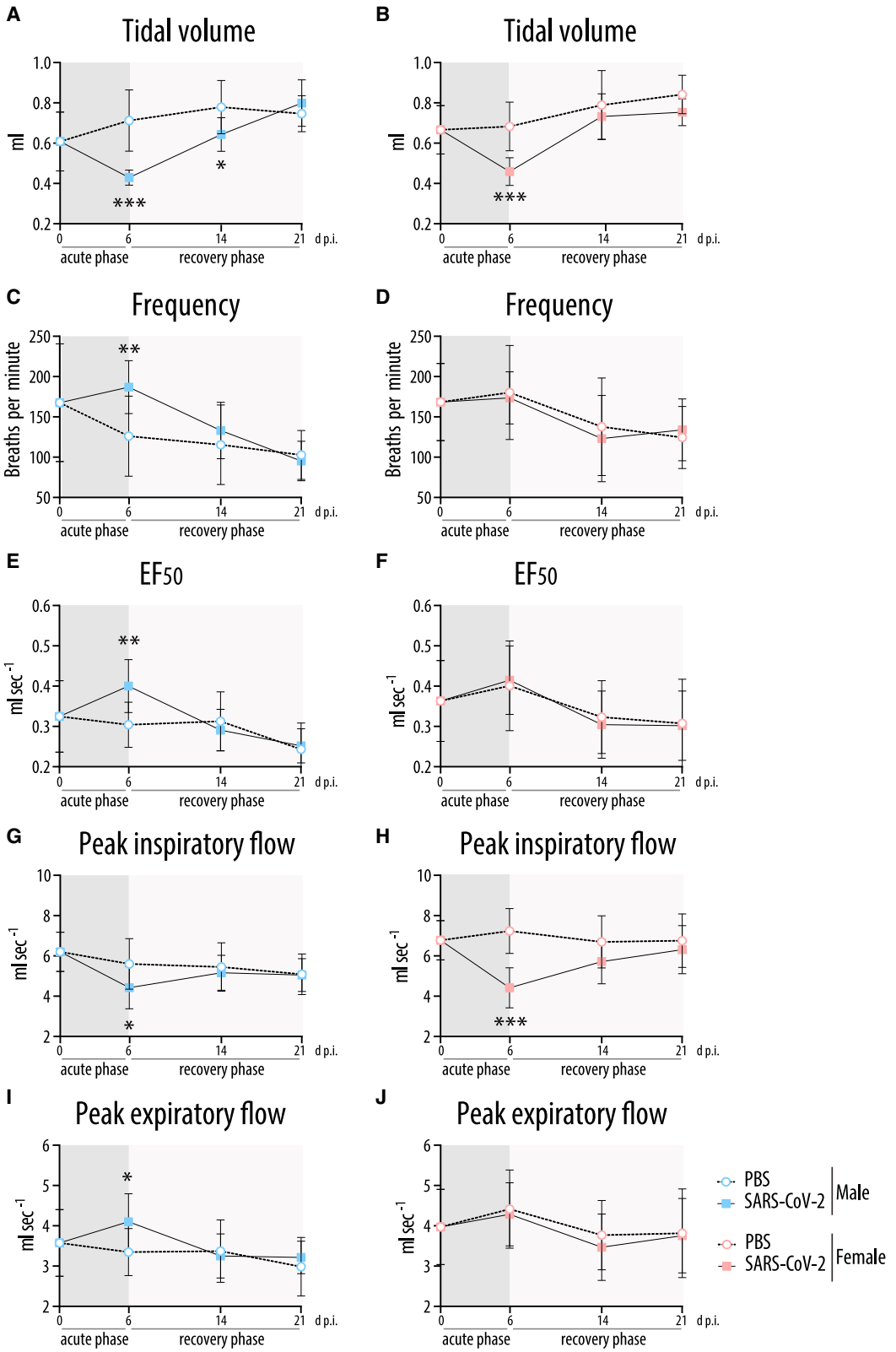

(legend on next page)

support the hypothesis that CYP19A1 expression in the lung is able to convert testosterone to estradiol in a defined setting, which can be inhibited by letrozole.

Therefore, we next treated SARS-CoV-2-infected male and female hamsters with letrozole (Figures 6A and 6B). Oral letrozole treatment is used in humans for the treatment of estrogen-receptor-positive breast cancer in women[42] as well as to treat hypogonadism in men.[43]

Using high-performance liquid chromatography (HPLC) analysis, we confirmed that the applied oral treatment regimen results in comparable doses in the lungs of male and female animals (Figure 6C). While in the male and female lungs letrozole was detected to comparable levels on days 3 and 6 p.i., plasma levels of letrozole were higher in infected females compared to males on days 3 and 6 p.i. (Figure 6D), supporting sex-dependent pharmacokinetics for letrozole that was also reported previously.[45–47]

Letrozole treatment resulted in elevated testosterone levels in virus-infected males, albeit not to a statistically significant extent (Figure 6E). Estradiol levels were significantly reduced upon letrozole treatment in infected males (Figure 6F). Letrozole treatment resulted in a trend toward elevated AR transcription in the lungs of infected males (Figure 6G). However, ESR-β transcription levels were significantly reduced in SARS-CoV-2-infected male hamsters upon letrozole treatment (Figure 6H). No significant changes were detected in ZIP-9 and ESR-α expression levels in infected males upon letrozole treatment (Figures S9A and S9B). In females, letrozole treatment led to significantly increased testosterone levels and a tendency toward reduced estradiol levels (Figures S9C and S9D). None of the androgen or estrogen receptor expression levels were affected in the lungs of infected females upon letrozole treatment (Figures S9E–S9H).

We then assessed whether recovered sex hormone levels might result in improved lung function in SARS-CoV-2-infected males and females. In PBS male and female controls, treatment with letrozole or vehicle did not affect lung function, ruling out an adverse effect in this regard (Figures S10 and S11). In males infected with SARS-CoV-2, letrozole treatment resulted in faster recovery of the tidal volume from day 6 p.i. onward, ultimately attaining the level of the vehicle group. Accordingly, the breathing frequency showed accelerated normalization in letrozole-treated animals, resulting in a longer inspiratory time (Figures 6I–6L and S12). This correlated histologically with fewer collapsed alveoli, fewer immune cell infiltrates in adjacent alveolar spaces, and less alveolar wall thickening in the lungs of SARS-CoV-2-infected males upon letrozole treatment (Figure 6M). In line with this, letrozole-treated males presented fewer fibrotic structures on day 21 p.i. compared to vehicle-treated males (Figure 6N). Overall, these findings were reflected by an increased weight gain of letrozole-treated males compared to vehicle males on day 21 p.i. (Figure 6O). In contrast, letrozole treatment did not improve lung function in SARS-CoV-2-infected females at any time point (Figures S9 and S12). In line with this, neither lung pathology nor weight was significantly improved in letrozole-treated infected females as compared to vehicle controls (Figures S9M–S9O).

These findings show that treatment with the clinically approved CYP19A1 inhibitor letrozole substantially improves male lung health in the hamster model.

Whole-lung transcriptome analysis identifies letrozole-treatment-modified pathways associated with improved lung health in SARS-CoV-2-infected male hamsters

To investigate which pathways might be modulated in SARS-CoV-2-infected male lungs that impair full recovery and how letrozole treatment contributes to improved lung health, we performed whole-lung transcriptomic profiling on day 21 p.i. To this end, we compared male and female hamsters infected with SARS-CoV-2 and treated them with either letrozole or vehicle. As negative controls, we included males and females inoculated with PBS and then treated with letrozole or vehicle. A total of 120 million sequence reads (on average approximately 4 million reads for each of five replicates per condition) amounting to 103 Gb sequence information were generated for all transcriptome libraries. Quality filtering resulted in high-quality sequence reads that were mapped onto the Syrian hamster draft genome sequence. For all conditions, the amount of mapped hamster reads was about 92% of all reads. We found that differential genes were expressed in males and females infected with SARS-CoV-2 (Figures 7A and 7B). Interestingly, the transcriptomic profile significantly changed in the infected male lungs treated with letrozole (Figure 7C) in contrast to letrozole-treated infected females (Figure 7D). In SARS-CoV-2-infected males and females, a total of 256 genes were upregulated, 188 of which were male specific and 57 female specific, with another 11 shared by both sexes (Figures 7A–7E). A total of 56 genes were downregulated in SARS-CoV-2-infected animals with 6 being male specific, 49 female specific, and 1 common gene. Letrozole treatment resulted in the downregulation of 133 out of 199 upregulated genes in infected males (Figure 7F). In contrast, in letrozole-treated infected females, 65 out of 68 genes remained unaltered (Figure 7G). Thus, letrozole treatment results in sex-specific alterations in the transcriptomic profile of the lung. Here, improved lung health in SARS-CoV-2-infected male hamsters upon letrozole treatment was associated with changes in many pathways, among which those involved in lipid and protein processes, e.g., lipid oxidation (gene ontology term GO:0034440), lipid modification (GO:0030258), and protein phosphorylation (GO:0006468) were among the most significant (Figure 7H).

These data show that letrozole treatment can recover most of the dysregulated genes in the lungs of SARS-CoV-2-infected males but not females.

Figure 5. Lung plethysmography in SARS-CoV-2-infected hamsters

Whole-body plethysmography in SARS-CoV-2-infected or control (PBS)-treated male (A, C, E, G, I) and female (B, D, F, H, J) hamsters at the indicated time points (n = 10; day 0 p.i., n = 12): tidal volume (A, B), frequency (C, D), EF_{50} (expiratory flow rate at the point 50% of tidal volume is expired) (E, F), peak inspiratory flow (G, H), and peak expiratory flow (I, J). Values are shown as means; error bars are shown as SD. Statistical significance was assessed by unpaired Student's t test (*$p \leq 0.05$, **$p < 0.01$, ***$p < 0.001$).

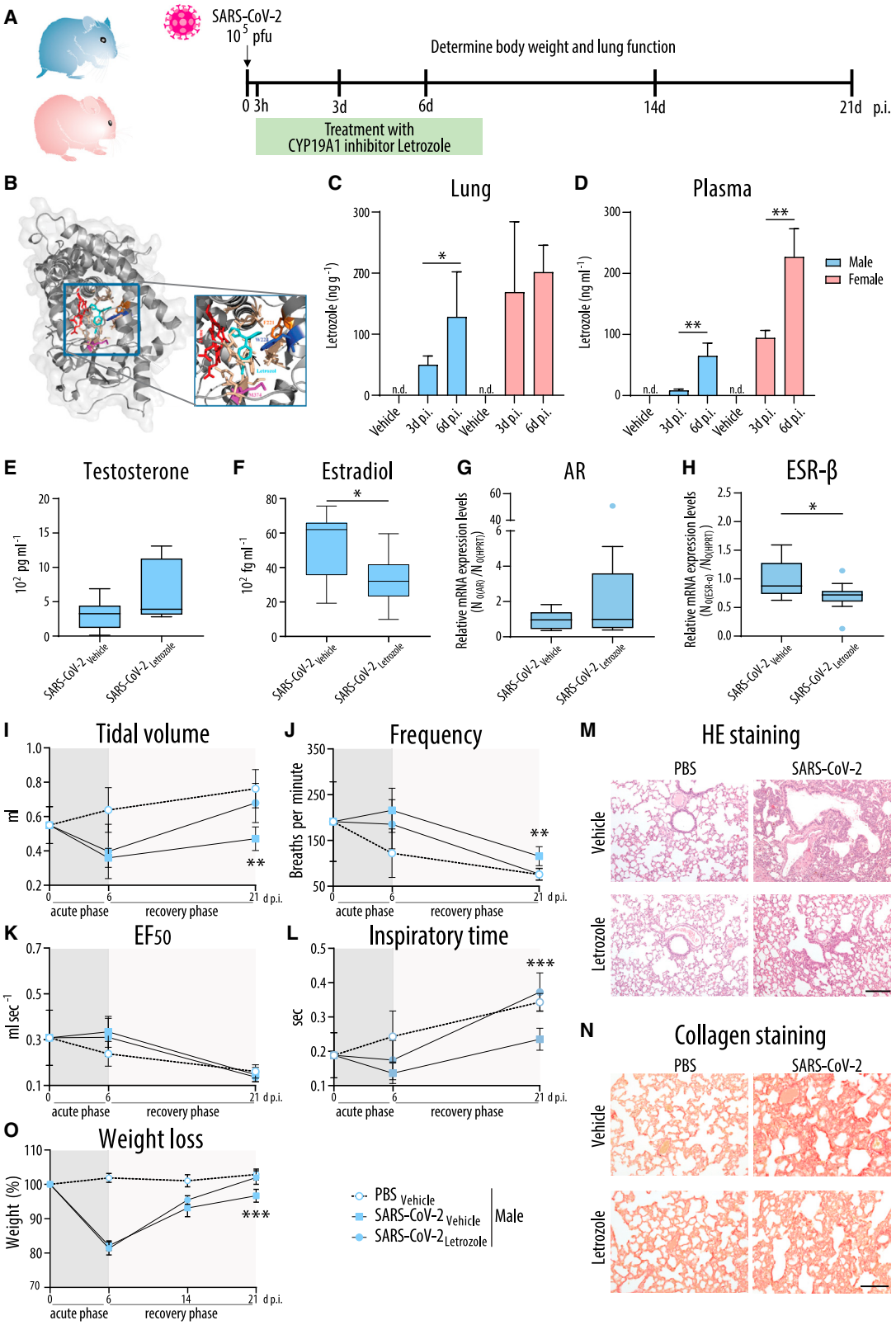

(legend on next page)

CellPress
OPEN ACCESS

DISCUSSION

We herein identified the *CYP19A1* gene as a crucial factor contributing to SARS-CoV-2 pathogenesis in males by analyzing WES data derived from 2,866 COVID-19 patients and autopsy-derived lung tissues from 86 COVID-19 decedents. Men with a CYP19A1-activity-increasing mutation (Thr201Met)[30] were more likely to be hospitalized with severe COVID-19 compared to men who did not possess this mutation or compared to women with COVID-19. Moreover, we found that elevated CYP19A1 expression was still prominent in the lungs of male COVID-19 patients at the time of death, when in most cases viral RNA was no longer detectable.

Using the golden hamster model, we studied in depth a putative causal role of CYP19A1 in sex-dependent disease outcome. We identified a causal role of CYP19A1 in male SARS-CoV-2 pathogenesis in hamsters.

Male and female hamsters infected with SARS-CoV-2 presented comparable weight loss until day 6 p.i. (the acute phase of infection) but showed significant differences from day 7 until 14 p.i. (recovery phase). SARS-CoV-2-infected male hamsters presented delayed weight gain and impaired lung function even 1 week after recovery from SARS-CoV-2 infection.

Impaired male lung health correlated with altered gene expression profiles in the male lung and its macrophages, such as increased *CYP19A1* expression and elevated ESR-β expression, which were further associated with reduced plasma testosterone and elevated plasma estradiol levels. Interestingly, we could also detect SARS-CoV-2 RNA and/or replicating virus in the testes and brain of male hamsters, but expression levels of CYP19A1 were generally not affected or even reduced in some cases (Figures S13 and S14). Thus, altered circulating sex hormone levels correlate mainly with increased CYP19A1 expression levels in the lungs of male hamsters upon SARS-CoV-2 infection. However, viral replication in the testes suggests a potential gonadal hit that likely additionally contributes to overall reduced testosterone levels. Alterations in circulating sex hormone levels detected in male hamsters are in agreement with reduced testosterone and elevated estradiol levels in the plasma of men hospitalized with COVID-19.[11–13] Follow-up studies in men show that even 1 year after initial SARS-CoV-2 diagnosis, 30% of COVID-19 patients still present testosterone levels that are below clinical references.[15]

In female hamsters, we found that respiratory SARS-CoV-2 infection also causes reduced lung function, albeit to a lesser extent when compared to males. SARS-CoV-2 infection reduces plasma estradiol levels in females, which might be explained by viral replication in the ovaries independently of *CYP19A1* expression (Figure S13). Similar to infected male hamsters, SARS-CoV-2 was detected in the brain without affecting *CYP19A1* expression (Figure S14). Most critically ill female COVID-19 patients, however, were post-menopausal,[13] which limits the translation of the data obtained in the young female animals at reproductive age used in this study. However, our findings here, where disease onset in females infected with SARS-CoV-2 correlate with low estradiol levels (in contrast to high estradiol levels in males), would be in line with the generally low estradiol levels in post-menopausal women. Nevertheless, future investigations are needed to understand the role of sex hormones on COVID-19 outcome in pre- compared to post-menopausal women.

Interestingly, low testosterone levels were previously reported to pose a poor prognostic marker in male but not female patients with avian H7N9 influenza A virus infection.[48] However, in contrast to COVID-19, avian H7N9 influenza was not paralleled by significantly elevated estradiol levels suggestive of common but also distinct mechanisms contributing to sex-dependent disease outcome upon respiratory virus infection.

The causal role of *CYP19A1* in male SARS-CoV-2 pathogenesis and male lung health was underpinned by treating infected hamsters with the clinically approved CYP19A1 inhibitor letrozole. SARS-CoV-2-infected male and female hamsters treated with letrozole showed elevated circulating testosterone levels and reduced circulating estradiol levels suggestive of functional CYP19A1 inhibition in both sexes. In males, full recovery of testosterone levels (in contrast to estradiol levels) could not be achieved. One possible reason for this could be the presence of SARS-CoV-2 RNA in the testis of infected males that likely contributes to impaired testosterone synthesis without the involvement of *CYP19A1*. However, reducing circulating estradiol levels as well as ESR-β expression in the lungs of SARS-CoV-2-infected males by letrozole treatment resulted in improved lung health with overall faster recovery in males. Thus, letrozole-treated males showed improved lung function that was reflected by ameliorated lung pathology and accelerated weight gain after virus clearance. In contrast, letrozole treatment did not show any benefit for SARS-CoV-2-infected females. These findings further confirm a causal role for *CYP19A1* in male SARS-CoV-2 pathogenesis.

While these findings might suggest that replacement of testosterone levels could provide an additional treatment option, this

Figure 6. Treatment of SARS-CoV-2-infected hamsters with the CYP19A1 inhibitor letrozole

(A) Timeline of experimental setup for letrozole treatment. Male and female hamsters were control treated with PBS or infected with SARS-CoV-2 and subjected to daily letrozole treatment from 3 h to 8 days p.i.

(B) Docking model of CYP19A1-letrozole complex adapted from Hong et al.[44]

(C and D) Letrozole levels in lung (C) and plasma (D) of male and female hamsters treated with vehicle or letrozole. n.d., not detectable.

(E–H) Testosterone (E), estradiol (F), as well as lung AR (G) and ESR-β (H) mRNA expression at 3 days p.i. (E, F) or 6 days p.i. (G, H) (n = 11). (G and H) SARS-CoV-2-infected and vehicle-treated hamsters were set as 1. Data are shown as a box-and-whisker plot.

(I–L) Whole-body plethysmography in infected male hamsters: Tidal volume (I), frequency (J), EF_{50} (K), and inspiratory time (L) (n = 5–7; day 0 p.i., n = 12).

(M and N) H&E staining (M) or collagen staining with Sirius red (N) of lung sections from infected male hamsters at 21 days p.i. (n = 5–7 per group). Scale bars, 200 μm (M) and 100 μm (N).

(O) Weight loss of infected male hamsters (n = 5–7 per group).

In (C), (D), (I–L), and (O), values are shown as means; error bars are shown as SD. Statistical significance was assessed by Mann-Whitney test or one-way ANOVA (*$p \leq 0.05$, **$p < 0.01$, ***$p < 0.001$).

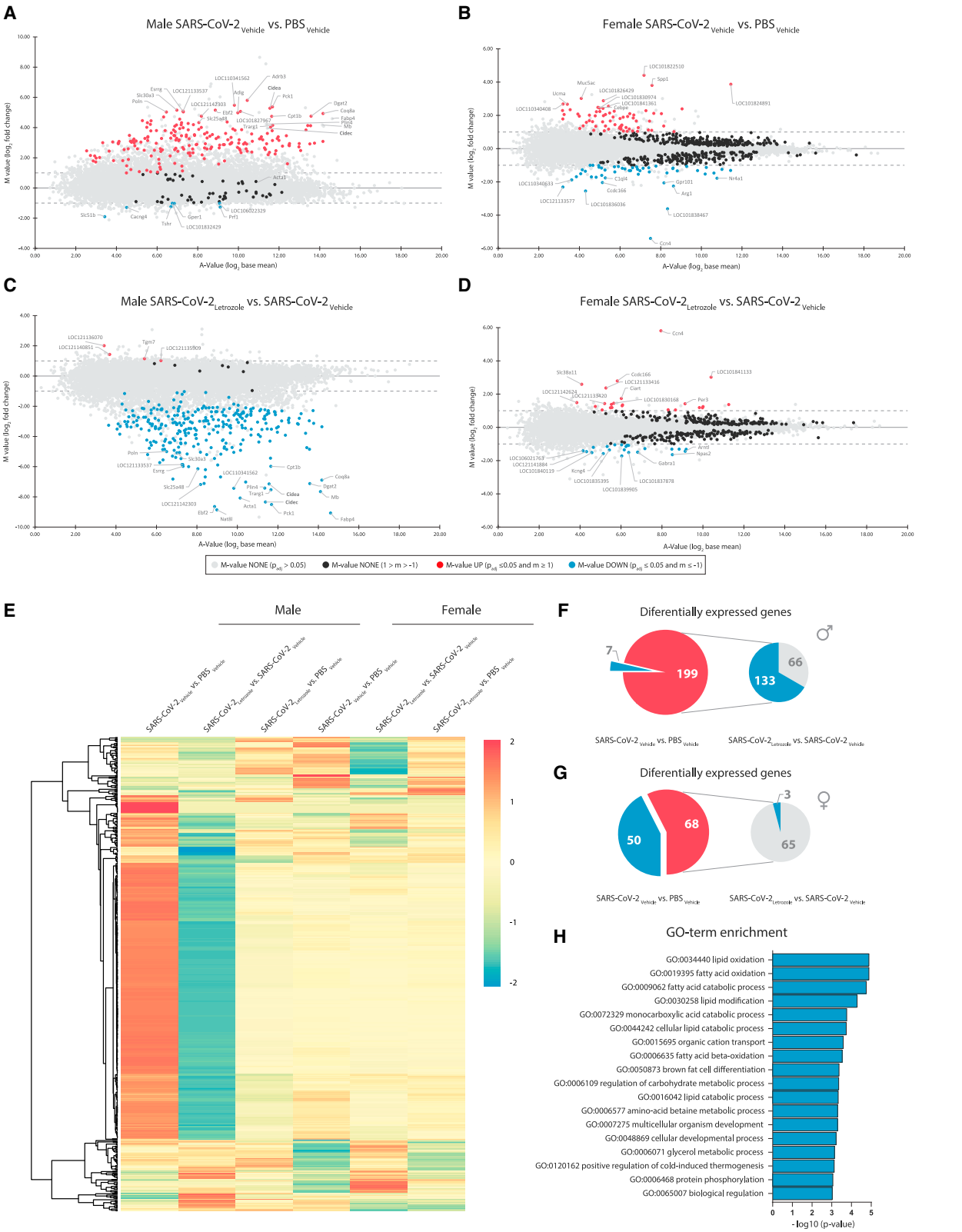

(legend on next page)

should be considered with caution. One reason for this is that *CYP19A1* transcription is likely dependent on testosterone concentration due to the presence of an AR binding site in its promoter region. Indeed, testosterone-dependent *CYP19A1* expression was confirmed in the lungs of male hamsters treated with testosterone (Figures S15A and S15B). Low-dose testosterone treatment increased *CYP19A1* mRNA expression in the lungs of SARS-CoV-2-infected male hamsters, while high-dose testosterone treatment inhibited *CYP19A1* expression in the lungs of infected animals to physiological levels as in uninfected PBS-treated males (Figure S15B). Low-dose testosterone treatment associated with high *CYP19A1* expression caused slightly elevated lung frequency, elevated ESR-β expression, increased weight loss, and reduced survival (Figures S15C–S15F). In contrast, high-dose testosterone treatment associated with inhibited *CYP19A1* expression resulted in reduced lung frequency, reduced ESR-β expression, weight loss, and increased survival compared to low-dose testosterone treatment in SARS-CoV-2-infected male hamsters (Figures S15C–S15F). These findings highlight the complexity of testosterone treatment in infected animals, which could be beneficial or detrimental depending on the dosage used. However, the detection of testosterone-dependent *CYP19A1* expression sheds new light on our current understanding, further highlighting the promising role of CYP19A1-targeted therapy that aims to balance sex hormone levels rather than substituting one hormone alone.

Mechanistically, whole-lung transcriptome analysis of SARS-CoV-2-infected hamsters with letrozole or vehicle treatment revealed key pathways associated with improved male outcome. We identified a series of gene pathways in the lungs of SARS-CoV-2-infected males upon letrozole treatment as compared to vehicle controls. The major pathways that were differentially altered upon letrozole treatment were involved in lipid oxidation, lipid modification, and protein phosphorylation. The prominent involvement of lipid pathways is interesting given that there is evidence that efficient SARS-CoV-2 replication depends on lipid metabolism.[49] Alveolar lipids are known to be involved in pulmonary diseases.[50] Similarly, for both sex steroids their involvement in wound healing has been reported previously.[51] It was reported that ovariectomized rats present diminished fibrosis, while estradiol replacement restored fibrotic response.[52] In mice, testosterone treatment restored asthmatic lung exacerbation by attenuating airway inflammation.[53] Population-based studies further supported this concept by showing strong associations between testosterone levels and lung function in men.[54] Although future studies are required to understand in more detail androgen- and/or estrogen-controlled transcription pathways involved in long-term lung health, our data further support the concept that balanced sex hormone levels are critical for lung health in general (Figure S16).

Besides fixing genetic variations in the *CYP19A1* gene, sex hormone levels can be additionally affected by other dynamic conditions such as age or metabolic comorbidities. Testosterone is produced in the gonads of boys at the age of 10–12 years, peaking in adulthood and steadily declining with increasing age. Age-related testosterone deficiency due to testicular dysfunction (primary hypogonadism) may thus pose another risk factor for reduced lung health as was previously reported in population-based studies.[54] Obesity is another high-risk factor for severe and even fatal COVID-19 outcome. *CYP19A1* is highly expressed in adipose tissue, where it also converts testosterone to estradiol. In obese people, low testosterone and elevated estradiol levels have been reported previously.[43,55,56]

Thus, we propose that the combination of a fixed genetic *CYP19A1* hit (Thr201Met) with several dynamic *CYP19A1* hits (SARS-CoV-2-infection-induced elevated *CYP19A1* transcription in the lung, age-related hypogonadism, and obesity) may orchestrate a deadly quartet in COVID-19 males.

Letrozole is a CYP19A1 inhibitor that is widely and successfully used in treating hypogonadism in men and estrogen-receptor-positive breast cancer in women. Letrozole was reported to inhibit wild-type as well as the Thr201Met variant of the CYP19A1 protein equally as effectively.[30] This suggests that men carrying a heterozygous or homozygous Thr201Met variant would be expected to benefit from letrozole treatment. Letrozole treatment was furthermore shown to normalize serum testosterone levels in obese men with hypogonadism.[43] Thus, beyond the direct effect of letrozole on inhibiting the SARS-CoV-2-infection-induced upregulation of *CYP19A1* and thereby sex hormone dysregulation, patients with additional sex hormone balance-disturbing conditions (CYP19A1 Thr201Met, age, and obesity) might additionally benefit from letrozole treatment upon SARS-CoV-2 infection.

Collectively, these findings highlight that the *CYP19A1* gene is involved in SARS-CoV-2 pathogenesis in males. We identified the clinically approved CYP19A1 inhibitor letrozole as a potential new therapeutic strategy to improve long-term disease outcomes in SARS-CoV-2-infected males.

Limitations of the study

This study has limitations that should be considered. The human genome data identified the CYP19A1-activity-increasing variant Thr201Met as a risk factor for severe COVID-19 in male patients. However, sex hormone levels were not measured within this patient cohort. Thus, future studies are needed that measure sex

Figure 7. Genome-wide transcriptome analysis of SARS-CoV-2-infected hamster lungs treated with the CYP19A1 inhibitor letrozole

(A–D) Genome-wide lung transcriptomic profiles of PBS-control-treated or SARS-CoV-2-infected male (A and C) and female (B and D) hamsters (n = 5), treated with vehicle or letrozole, at 21days p.i. were compared and are shown as ratio/intensity scatterplots (M/A plot [M-value = $\log_2$ fold change; A-value = $\log_2$ base mean]).

(E) Heatmap depicting normalized expression of differentially expressed genes in the lung of male and female hamsters, clustered according to their expression profiles (cutoff $\log_2$ fold change ≥ 1 or ≤ -1, with an adjusted p value of ≤ 0.05).

(F and G) Significant differentially expressed genes in the lung of control (PBS) or SARS-CoV-2-infected male (F) and female (G) hamsters.

(H) Gene ontology term enrichment (biological process) of genes that were significantly downregulated in letrozole-treated SARS-CoV-2-infected male hamsters, compared to the vehicle control group.

hormone levels in patients harboring the CYP19A1-activity-increasing variant Thr201Met in comparison to other variants with unaffected CYP19A1 activity, preferably before and after SARS-CoV-2 infection. Another limitation of the study is that the positive treatment outcome with letrozole in SARS-CoV-2-infected male hamsters cannot be extrapolated to humans. Future investigations are required to evaluate letrozole therapy in COVID-19 patients while taking the complexity of hormonal mode of action into account.

STAR★METHODS

Detailed methods are provided in the online version of this paper and include the following:

- KEY RESOURCES TABLE
- RESOURCE AVAILABILITY
  - Lead contact
  - Materials availability
  - Data and code availability
- EXPERIMENTAL MODEL AND STUDY PARTICIPANT DETAILS
  - GEN-COVID cohort
  - Fatal COVID-19 cases and controls
  - Cells
  - Animals
- METHOD DETAILS
  - Viruses
  - Animal experiments
  - Histology and immunohistochemistry in fatal COVID-19 cases
  - *In situ* hybridization (ISH)
  - Plethysmography
  - Histology and immunohistochemistry in hamsters
  - Determination of virus titers and viral RNA levels
  - Measurement of hormone and cytokine/chemokine levels
  - Infection of human cells with respiratory viruses
  - Aromatase activity in SARS-CoV-2-infected Calu-3 cells
  - Isolation and poly(I:C) treatment of lung macrophages from golden hamsters
  - RNA isolation
  - Determination of mRNA expression levels by real-time quantitative PCR (RT-qPCR)
  - Letrozole detection by high-performance liquid chromatography (HPLC)
  - Differential gene expression analysis by stranded mRNA-Seq preparation and sequencing of cDNA libraries
  - Transcript mapping and differential gene expression analysis
- QUANTIFICATION AND STATISTICAL ANALYSIS

SUPPLEMENTAL INFORMATION

Supplemental information can be found online at https://doi.org/10.1016/j.xcrm.2023.101152.

ACKNOWLEDGMENTS

This study is dedicated to the memory of my academic mentor Hans Dieter Klenk (*06.25.1938, †06.01.2021), a pioneer in influenza research on interspecies transmission. He will be dearly missed.

This study was supported by various grants obtained from the Federal Ministry of Health, Germany (BMG; ZMV I 1-2520COR501 to G.G.), the Federal Ministry of Education and Research, Germany (BMBF; project no. 03COV06B to G.G.; no. 01KI1723G to W.B.; no. 01KX2121 to F.H., P.L., A.H., and B.O.), the Ministry for Science and Culture of Lower Saxony (14-76103-184-CORONA-15/20 to W.B. and M.v.K.-B.), the Ministry of Science, Research and the Arts Baden-Württemberg and the Deutsche Herzstiftung (to K.K.), and ZonMw, the Netherlands (project no. 10430 01 201 0016 to J.T.). We thank all staff of the Core Facility Small Animal Models of the Leibniz Institute of Virology, particularly Ursula Müller and Oliver Strauch for their excellent support with the golden hamster model. We thank the NGS team of the Omics CF NGS and CeBiTec as well as the technical staff of the CeBiTec Technology Platform Genomics, particularly Eva Schulte-Bernd, Yvonne Kutter, and Katharina Hanuschka for technical assistance. We thank Kristin Hartmann and Martin Müller from the Leibniz Institute of Virology in Hamburg for technical assistance. This study is part of the Italian GEN-COVID Multicenter Study (https://sites.google.com/dbm.unisi.it/gen-covid) aimed at identifying the COVID-19 host genetic bases. Specimens were provided by the COVID-19 Biobank of Siena, part of the Genetic Biobank of Siena, member of Telethon Network of Genetic Biobanks, BBMRI-IT, EuroBioBank, and RD-Connect. CINECA consortium and Network for Italian Genomes (http://www.nig.cineca.it) provided computational resources and support. We thank private donors for the support provided to A.R. (Department of Medical Biotechnologies, University of Siena, D.L n.18 of March 17, 2020) and the GEN-COVID Multicenter Study Group (https://www.covid19hg.org/). We also thank the following projects: MIUR-Dipartimenti di Eccellenza 2018–2020; Bando Ricerca COVID-19 Toscana; Intesa San Paolo-2020 charity; Italian Ministry of University and Research - Bando FISR 2020 - HACKTHECOV; Instituto Buddista Italiano Soka Gakkai - PAT-COVID; and EU project H2020-SC1-FA-DTS-2018-2020 - INTERVENE).

AUTHOR CONTRIBUTIONS

G.G. designed the study and wrote the manuscript. S.S.B., S.B., N.K.M., and B.S. performed all animal experiments, analyzed the data, and revised the manuscript. F. Stoll, A.A.J., T. Bai, M.Z., A.L., J.R., H.J., Z.M., K.B., V.P.d.R., M.v.K.-B., C.S., and V.K.-B. assisted with the animal experiments and performed molecular analysis. N.K.M., S.S.B., B.S., S.B., Z.S., M.W., and S.K.-E. performed and/or interpreted data obtained from lung function experiments. A.A.J. isolated and treated lung macrophages from golden hamsters. G.B., K.B., M.d.l.R., D.S., T.G., and W.B. performed histopathological and immunohistochemical analysis of the animal organs. C.K. and F.R. performed letrozole HPLC measurement in plasma and lung tissue of letrozole-treated golden hamsters. T. Busche, D.W., and J.K. performed RNA-sequencing and transcriptomic data analysis. M.S., D.J., A.N., and S. Kluge provided clinical samples from COVID-19 patients for SARS-CoV-2 virus isolation. K.K., M. Schroeder., F.H., S. Krasemann, P.L., A.H., B.O., L.L., L.B., T.P.P.v.d.B., B.L., D.v.R., J.v.d.T., K.K., and M. Sauter sampled and analyzed the lungs of fatal COVID-19 cases. K.N. and A.C.M. supported the analysis of transcriptomic data. N.S. performed structural analysis. F. Sommer supported the design of letrozole treatment studies. T.W. supported the evaluation of the human cohort data. GEN-COVID Multicenter Study, M.B., and A.R. provided and curated clinical data. C.F., S.F., and A.R. performed WES data analysis and statistical data analysis. All authors approved the manuscript.

DECLARATION OF INTERESTS

Method for predicting the course of a viral disease. Inventors: G.G. and S.S.-B. Filing date: 04.30.2021. Pending patent applications: Europe (EP21722231.4), USA (US17995728), Japan (JP2022-566073), China (CN202180031796.5).

INCLUSION AND DIVERSITY

We support inclusive, diverse, and equitable conduct of research.

Received: July 12, 2022
Revised: May 10, 2023
Accepted: July 18, 2023
Published: August 11, 2023

REFERENCES

1. Dong, E., Du, H., and Gardner, L. (2020). An interactive web-based dashboard to track COVID-19 in real time. Lancet Infect. Dis. *20*, 533–534. https://doi.org/10.1016/S1473-3099(20)30120-1.
2. Williamson, E.J., Walker, A.J., Bhaskaran, K., Bacon, S., Bates, C., Morton, C.E., Curtis, H.J., Mehrkar, A., Evans, D., Inglesby, P., et al. (2020). Factors associated with COVID-19-related death using OpenSAFELY. Nature *584*, 430–436. https://doi.org/10.1038/s41586-020-2521-4.
3. Clark, A., Jit, M., Warren-Gash, C., Guthrie, B., Wang, H.H.X., Mercer, S.W., Sanderson, C., McKee, M., Troeger, C., Ong, K.L., et al. (2020). Global, regional, and national estimates of the population at increased risk of severe COVID-19 due to underlying health conditions in 2020: a modelling study. Lancet Global Health *8*, e1003–e1017. https://doi.org/10.1016/S2214-109X(20)30264-3.
4. Jin, J.M., Bai, P., He, W., Wu, F., Liu, X.F., Han, D.M., Liu, S., and Yang, J.K. (2020). Gender Differences in Patients With COVID-19: Focus on Severity and Mortality. Front. Public Health *8*, 152. https://doi.org/10.3389/fpubh.2020.00152.
5. Bhopal, S.S., and Bhopal, R. (2020). Sex differential in COVID-19 mortality varies markedly by age. Lancet *396*, 532–533. https://doi.org/10.1016/S0140-6736(20)31748-7.
6. Goodman, K.E., Magder, L.S., Baghdadi, J.D., Pineles, L., Levine, A.R., Perencevich, E.N., and Harris, A.D. (2021). Impact of Sex and Metabolic Comorbidities on COVID-19 Mortality Risk Across Age Groups: 66,646 Inpatients Across 613 U.S. Hospitals. Clin. Infect. Dis. *73*, e4113–e4123. https://doi.org/10.1093/cid/ciaa1787.
7. Krieger, N., Chen, J.T., and Waterman, P.D. (2020). Excess mortality in men and women in Massachusetts during the COVID-19 pandemic. Lancet *395*, 1829. https://doi.org/10.1016/S0140-6736(20)31234-4.
8. Haitao, T., Vermunt, J.V., Abeykoon, J., Ghamrawi, R., Gunaratne, M., Jayachandran, M., Narang, K., Parashuram, S., Suvakov, S., and Garovic, V.D. (2020). COVID-19 and Sex Differences: Mechanisms and Biomarkers. Mayo Clin. Proc. *95*, 2189–2203. https://doi.org/10.1016/j.mayocp.2020.07.024.
9. Decaroli, M.C., and Rochira, V. (2017). Aging and sex hormones in males. Virulence *8*, 545–570. https://doi.org/10.1080/21505594.2016.1259053.
10. Dhindsa, S., Zhang, N., McPhaul, M.J., Wu, Z., Ghoshal, A.K., Erlich, E.C., Mani, K., Randolph, G.J., Edwards, J.R., Mudd, P.A., and Diwan, A. (2021). Association of Circulating Sex Hormones With Inflammation and Disease Severity in Patients With COVID-19. JAMA Netw. Open *4*, e2111398. https://doi.org/10.1001/jamanetworkopen.2021.11398.
11. Infante, M., Pieri, M., Lupisella, S., D'Amore, L., Bernardini, S., Fabbri, A., Iannetta, M., Andreoni, M., and Morello, M. (2021). Low testosterone levels and high estradiol to testosterone ratio are associated with hyperinflammatory state and mortality in hospitalized men with COVID-19. Eur. Rev. Med. Pharmacol. Sci. *25*, 5889–5903. https://doi.org/10.26355/eurrev_202110_26865.
12. Salonia, A., Pontillo, M., Capogrosso, P., Gregori, S., Tassara, M., Boeri, L., Carenzi, C., Abbate, C., Cignoli, D., Ferrara, A.M., et al. (2021). Severely low testosterone in males with COVID-19: A case-control study. Andrology *9*, 1043–1052. https://doi.org/10.1111/andr.12993.
13. Schroeder, M., Schaumburg, B., Mueller, Z., Parplys, A., Jarczak, D., Roedl, K., Nierhaus, A., de Heer, G., Grensemann, J., Schneider, B., et al. (2021). High estradiol and low testosterone levels are associated with critical illness in male but not in female COVID-19 patients: a retrospective cohort study. Emerg. Microb. Infect. *10*, 1807–1818. https://doi.org/10.1080/22221751.2021.1969869.
14. Salonia, A., Pontillo, M., Capogrosso, P., Gregori, S., Carenzi, C., Ferrara, A.M., Rowe, I., Boeri, L., Larcher, A., Ramirez, G.A., et al. (2022). Testosterone in males with COVID-19: A 7-month cohort study. Andrology *10*, 34–41. https://doi.org/10.1111/andr.13097.
15. Salonia, A., Pontillo, M., Capogrosso, P., Pozzi, E., Ferrara, A.M., Cotelessa, A., Belladelli, F., Corsini, C., Gregori, S., Rowe, I., et al. (2023). Testosterone in males with COVID-19: a 12-month cohort study. Andrology *11*, 17–23. https://doi.org/10.1111/andr.13322.
16. Muehlenbein, M.P., Gassen, J., Shattuck, E.C., and Sparks, C.S. (2023). Lower testosterone levels are associated with higher risk of death in men. Evol. Med. Public Health *11*, 30–40. https://doi.org/10.1093/emph/eoac044.
17. Toscano-Guerra, E., Martínez-Gallo, M., Arrese-Muñoz, I., Giné, A., Díaz-Troyano, N., Gabriel-Medina, P., Riveiro-Barciela, M., Labrador-Horrillo, M., Martinez-Valle, F., Montalvá, A.S., et al. (2022). Recovery of serum testosterone levels is an accurate predictor of survival from COVID-19 in male patients. BMC Med. *20*, 129. https://doi.org/10.1186/s12916-022-02345-w.
18. Wierman, M.E. (2007). Sex steroid effects at target tissues: mechanisms of action. Adv. Physiol. Educ. *31*, 26–33. https://doi.org/10.1152/advan.00086.2006.
19. Townsend, E.A., Miller, V.M., and Prakash, Y.S. (2012). Sex differences and sex steroids in lung health and disease. Endocr. Rev. *33*, 1–47. https://doi.org/10.1210/er.2010-0031.
20. Seaborn, T., Simard, M., Provost, P.R., Piedboeuf, B., and Tremblay, Y. (2010). Sex hormone metabolism in lung development and maturation. Trends Endocrinol. Metabol. *21*, 729–738. https://doi.org/10.1016/j.tem.2010.09.001.
21. Wulfsohn, N.L., Politzer, W.M., and Henrico, J.S. (1964). Testosterone Therapy in Bronchial Asthma. S. Afr. Med. J. *38*, 170–172.
22. Fuentes, N., and Silveyra, P. (2018). Endocrine regulation of lung disease and inflammation. Exp. Biol. Med. (Maywood, NJ, U. S.) *243*, 1313–1322. https://doi.org/10.1177/1535370218816653.
23. Triebner, K., Matulonga, B., Johannessen, A., Suske, S., Benediktsdóttir, B., Demoly, P., Dharmage, S.C., Franklin, K.A., Garcia-Aymerich, J., Gullón Blanco, J.A., et al. (2017). Menopause Is Associated with Accelerated Lung Function Decline. Am. J. Respir. Crit. Care Med. *195*, 1058–1065. https://doi.org/10.1164/rccm.201605-0968OC.
24. Jakobsson, J., Palonek, E., Lorentzon, M., Ohlsson, C., Rane, A., and Ekström, L. (2007). A novel polymorphism in the 17beta-hydroxysteroid dehydrogenase type 5 (aldo-keto reductase 1C3) gene is associated with lower serum testosterone levels in caucasian men. Pharmacogenomics J. *7*, 282–289. https://doi.org/10.1038/sj.tpj.6500419.
25. Ellis, J.A., Panagiotopoulos, S., Akdeniz, A., Jerums, G., and Harrap, S.B. (2005). Androgenic correlates of genetic variation in the gene encoding 5alpha-reductase type 1. J. Hum. Genet. *50*, 534–537. https://doi.org/10.1007/s10038-005-0289-x.
26. Huhtaniemi, I.T., Pye, S.R., Holliday, K.L., Thomson, W., O'Neill, T.W., Platt, H., Payne, D., John, S.L., Jiang, M., Bartfai, G., et al. (2010). Effect of polymorphisms in selected genes involved in pituitary-testicular function on reproductive hormones and phenotype in aging men. J. Clin. Endocrinol. Metab. *95*, 1898–1908. https://doi.org/10.1210/jc.2009-2071.
27. Shiota, M., Fujimoto, N., Tsukahara, S., Ushijima, M., Takeuchi, A., Kashiwagi, E., Inokuchi, J., Tatsugami, K., Uchiumi, T., and Eto, M. (2019). The impact of genetic polymorphism on CYP19A1 in androgen-deprivation therapy among Japanese men. Cancer Chemother. Pharmacol. *83*, 933–938. https://doi.org/10.1007/s00280-019-03811-8.
28. Daga, S., Fallerini, C., Baldassarri, M., Fava, F., Valentino, F., Doddato, G., Benetti, E., Furini, S., Giliberti, A., Tita, R., et al. (2021). Employing a systematic approach to biobanking and analyzing clinical and genetic

data for advancing COVID-19 research. Eur. J. Hum. Genet. *29*, 745–759. https://doi.org/10.1038/s41431-020-00793-7.

29. Picchiotti, N., Benetti, E., Fallerini, C., Daga, S., Baldassarri, M., Fava, F., Zguro, K., Valentino, F., Doddato, G., Giliberti, A., et al. (2021). Post-Mendelian genetic model in COVID-19. MedRxive. https://doi.org/10.1101/2021.01.27.21250593.
30. Payne, E.J., Ingley, E., Dick, I.M., Wilson, S.G., Bond, C.S., and Prince, R.L. (2009). In vitro kinetic properties of the Thr201Met variant of human aromatase gene CYP19A1: functional responses to substrate and product inhibition and enzyme inhibitors. J. Clin. Endocrinol. Metab. *94*, 2998–3002. https://doi.org/10.1210/jc.2008-2309.
31. Nathan, L., Shi, W., Dinh, H., Mukherjee, T.K., Wang, X., Lusis, A.J., and Chaudhuri, G. (2001). Testosterone inhibits early atherogenesis by conversion to estradiol: critical role of aromatase. Proc. Natl. Acad. Sci. USA *98*, 3589–3593. https://doi.org/10.1073/pnas.051003698.
32. Diano, S., Horvath, T.L., Mor, G., Register, T., Adams, M., Harada, N., and Naftolin, F. (1999). Aromatase and estrogen receptor immunoreactivity in the coronary arteries of monkeys and human subjects. Menopause *6*, 21–28.
33. Nebert, D.W., Wikvall, K., and Miller, W.L. (2013). Human cytochromes P450 in health and disease. Philos. Trans. R. Soc. Lond. B Biol. Sci. *368*, 20120431. https://doi.org/10.1098/rstb.2012.0431.
34. Enjuanes, A., Garcia-Giralt, N., Supervía, A., Nogués, X., Ruiz-Gaspà, S., Bustamante, M., Mellibovsky, L., Grinberg, D., Balcells, S., and Díez-Pérez, A. (2005). Functional analysis of the I.3, I.6, pII and I.4 promoters of CYP19 (aromatase) gene in human osteoblasts and their role in vitamin D and dexamethasone stimulation. Eur. J. Endocrinol. *153*, 981–988. https://doi.org/10.1530/eje.1.02032.
35. Kamat, A., Graves, K.H., Smith, M.E., Richardson, J.A., and Mendelson, C.R. (1999). A 500-bp region, approximately 40 kb upstream of the human CYP19 (aromatase) gene, mediates placenta-specific expression in transgenic mice. Proc. Natl. Acad. Sci. USA *96*, 4575–4580. https://doi.org/10.1073/pnas.96.8.4575.
36. Sebastian, S., Takayama, K., Shozu, M., and Bulun, S.E. (2002). Cloning and characterization of a novel endothelial promoter of the human CYP19 (aromatase P450) gene that is up-regulated in breast cancer tissue. Mol. Endocrinol. *16*, 2243–2254. https://doi.org/10.1210/me.2002-0123.
37. Toda, K., Terashima, M., Kawamoto, T., Sumimoto, H., Yokoyama, Y., Kuribayashi, I., Mitsuuchi, Y., Maeda, T., Yamamoto, Y., Sagara, Y., et al. (1990). Structural and functional characterization of human aromatase P-450 gene. Eur. J. Biochem. *193*, 559–565. https://doi.org/10.1111/j.1432-1033.1990.tb19372.x.
38. Zhao, Y., Mendelson, C.R., and Simpson, E.R. (1995). Characterization of the sequences of the human CYP19 (aromatase) gene that mediate regulation by glucocorticoids in adipose stromal cells and fetal hepatocytes. Mol. Endocrinol. *9*, 340–349. https://doi.org/10.1210/mend.9.3.7776980.
39. Cisternas, C.D., Cabrera Zapata, L.E., Arevalo, M.A., Garcia-Segura, L.M., and Cambiasso, M.J. (2017). Regulation of aromatase expression in the anterior amygdala of the developing mouse brain depends on ERbeta and sex chromosome complement. Sci. Rep. *7*, 5320. https://doi.org/10.1038/s41598-017-05658-6.
40. Imai, M., Iwatsuki-Horimoto, K., Hatta, M., Loeber, S., Halfmann, P.J., Nakajima, N., Watanabe, T., Ujie, M., Takahashi, K., Ito, M., et al. (2020). Syrian hamsters as a small animal model for SARS-CoV-2 infection and countermeasure development. Proc. Natl. Acad. Sci. USA *117*, 16587–16595. https://doi.org/10.1073/pnas.2009799117.
41. Sia, S.F., Yan, L.M., Chin, A.W.H., Fung, K., Choy, K.T., Wong, A.Y.L., Kaewpreedee, P., Perera, R.A.P.M., Poon, L.L.M., Nicholls, J.M., et al. (2020). Pathogenesis and transmission of SARS-CoV-2 in golden hamsters. Nature *583*, 834–838. https://doi.org/10.1038/s41586-020-2342-5.
42. Goss, P.E., Ingle, J.N., Martino, S., Robert, N.J., Muss, H.B., Piccart, M.J., Castiglione, M., Tu, D., Shepherd, L.E., Pritchard, K.I., et al. (2003). A randomized trial of letrozole in postmenopausal women after five years of tamoxifen therapy for early-stage breast cancer. N. Engl. J. Med. *349*, 1793–1802. https://doi.org/10.1056/NEJMoa032312.
43. de Boer, H., Verschoor, L., Ruinemans-Koerts, J., and Jansen, M. (2005). Letrozole normalizes serum testosterone in severely obese men with hypogonadotropic hypogonadism. Diabetes Obes. Metabol. *7*, 211–215. https://doi.org/10.1111/j.1463-1326.2004.00397.x.
44. Hong, Y., Rashid, R., and Chen, S. (2011). Binding features of steroidal and nonsteroidal inhibitors. Steroids *76*, 802–806. https://doi.org/10.1016/j.steroids.2011.02.037.
45. Arora, P., Gudelsky, G., and Desai, P.B. (2021). Gender-based differences in brain and plasma pharmacokinetics of letrozole in sprague-dawley rats: Application of physiologically-based pharmacokinetic modeling to gain quantitative insights. PLoS One *16*, e0248579. https://doi.org/10.1371/journal.pone.0248579.
46. Liu, X.D., Xie, L., Zhong, Y., and Li, C.X. (2000). Gender difference in letrozole pharmacokinetics in rats. Acta Pharmacol. Sin. *21*, 680–684.
47. Wempe, M.F., Buchanan, C.M., Buchanan, N.L., Edgar, K.J., Hanley, G.A., Ramsey, M.G., Skotty, J.S., and Rice, P.J. (2007). Pharmacokinetics of letrozole in male and female rats: influence of complexation with hydroxybutenyl-beta cyclodextrin. J. Pharm. Pharmacol. *59*, 795–802. https://doi.org/10.1211/jpp.59.6.0006.
48. Bai, T., Chen, Y., Beck, S., Stanelle-Bertram, S., Mounogou, N.K., Chen, T., Dong, J., Schneider, B., Jia, T., Yang, J., et al. (2022). H7N9 avian influenza virus infection in men is associated with testosterone depletion. Nat. Commun. *13*, 6936. https://doi.org/10.1038/s41467-022-34500-5.
49. Zickler, M., Stanelle-Bertram, S., Ehret, S., Heinrich, F., Lange, P., Schaumburg, B., Mounogou, N., Beck, S., Jaeckstein, M., Mann, O., et al. (2021). Replication of SARS-CoV-2 in Adipose Tissue Determines Organ and Systemic Lipid Metabolism in Hamsters and Humans (SSRN). https://papers.ssrn.com/sol3/papers.cfm?abstract_id=3939147.
50. Agudelo, C.W., Samaha, G., and Garcia-Arcos, I. (2020). Alveolar lipids in pulmonary disease. Lipids Health Dis. *19*, 122. https://doi.org/10.1186/s12944-020-01278-8.
51. Gilliver, S.C., Ruckshanthi, J.P.D., Hardman, M.J., Nakayama, T., and Ashcroft, G.S. (2008). Sex dimorphism in wound healing: the roles of sex steroids and macrophage migration inhibitory factor. Endocrinology *149*, 5747–5757. https://doi.org/10.1210/en.2008-0355.
52. Carey, M.A., Card, J.W., Voltz, J.W., Germolec, D.R., Korach, K.S., and Zeldin, D.C. (2007). The impact of sex and sex hormones on lung physiology and disease: lessons from animal studies. Am. J. Physiol. Lung Cell Mol. Physiol. *293*, L272–L278. https://doi.org/10.1152/ajplung.00174.2007.
53. Cephus, J.Y., Stier, M.T., Fuseini, H., Yung, J.A., Toki, S., Bloodworth, M.H., Zhou, W., Goleniewska, K., Zhang, J., Garon, S.L., et al. (2017). Testosterone Attenuates Group 2 Innate Lymphoid Cell-Mediated Airway Inflammation. Cell Rep. *21*, 2487–2499. https://doi.org/10.1016/j.celrep.2017.10.110.
54. Lenoir, A., Fuertes, E., Gómez-Real, F., Leynaert, B., van der Plaat, D.A., and Jarvis, D. (2020). Lung function changes over 8 years and testosterone markers in both sexes: UK Biobank. ERJ Open Res. *6*, 00070-2020. https://doi.org/10.1183/23120541.00070-2020.
55. Cohen, P.G. (1999). The hypogonadal-obesity cycle: role of aromatase in modulating the testosterone-estradiol shunt–a major factor in the genesis of morbid obesity. Med. Hypotheses *52*, 49–51. https://doi.org/10.1054/mehy.1997.0624.
56. Cohen, P.G. (2008). Obesity in men: the hypogonadal-estrogen receptor relationship and its effect on glucose homeostasis. Med. Hypotheses *70*, 358–360. https://doi.org/10.1016/j.mehy.2007.05.020.
57. Otte, A., Sauter, M., Daxer, M.A., McHardy, A.C., Klingel, K., and Gabriel, G. (2015). Adaptive Mutations That Occurred during Circulation in Humans of H1N1 Influenza Virus in the 2009 Pandemic Enhance Virulence in Mice. J. Virol. *89*, 7329–7337. https://doi.org/10.1128/JVI.00665-15.

58. Ruijter, J.M., Ramakers, C., Hoogaars, W.M.H., Karlen, Y., Bakker, O., van den Hoff, M.J.B., and Moorman, A.F.M. (2009). Amplification efficiency: linking baseline and bias in the analysis of quantitative PCR data. Nucleic Acids Res. *37*, e45. https://doi.org/10.1093/nar/gkp045.

59. Wibberg, D., Andersson, L., Tzelepis, G., Rupp, O., Blom, J., Jelonek, L., Pühler, A., Fogelqvist, J., Varrelmann, M., Schlüter, A., and Dixelius, C. (2016). Genome analysis of the sugar beet pathogen Rhizoctonia solani AG2-2IIIB revealed high numbers in secreted proteins and cell wall degrading enzymes. BMC Genom. *17*, 245. https://doi.org/10.1186/s12864-016-2561-1.

60. Eden, E., Navon, R., Steinfeld, I., Lipson, D., and Yakhini, Z. (2009). GOrilla: a tool for discovery and visualization of enriched GO terms in ranked gene lists. BMC Bioinf. *10*, 48. https://doi.org/10.1186/1471-2105-10-48.

61. Synopsis, C.-T.T. (2021). WHO R&D Blue Print. WHO R&D Blue Print. https://www.who.int/publications/i/item/covid-19-therapeutic-trial-synopsis.

62. Bösmüller, H., Traxler, S., Bitzer, M., Häberle, H., Raiser, W., Nann, D., Frauenfeld, L., Vogelsberg, A., Klingel, K., and Fend, F. (2020). The evolution of pulmonary pathology in fatal COVID-19 disease: an autopsy study with clinical correlation. Virchows Arch. *477*, 349–357. https://doi.org/10.1007/s00428-020-02881-x.

63. Jelovac, D., Macedo, L., Goloubeva, O.G., Handratta, V., and Brodie, A.M.H. (2005). Additive antitumor effect of aromatase inhibitor letrozole and antiestrogen fulvestrant in a postmenopausal breast cancer model. Cancer Res. *65*, 5439–5444. https://doi.org/10.1158/0008-5472.CAN-04-2782.

64. Sabnis, G., Goloubeva, O., Gilani, R., Macedo, L., and Brodie, A. (2010). Sensitivity to the aromatase inhibitor letrozole is prolonged after a "break" in treatment. Mol. Cancer Therapeut. *9*, 46–56. https://doi.org/10.1158/1535-7163.MCT-09-0696.

65. Horiuchi, S., Oishi, K., Carrau, L., Frere, J., Møller, R., Panis, M., and tenOever, B.R. (2021). Immune memory from SARS-CoV-2 infection in hamsters provides variant-independent protection but still allows virus transmission. Sci. Immunol. *6*, eabm3131. https://doi.org/10.1126/sciimmunol.abm3131.

66. Hegde, A.R., Padya, B.S., Soman, S., and Mutalik, S. (2021). A simple, precise, and sensitive HPLC method for quantification of letrozole in rat plasma: development, validation, and preclinical pharmacokinetics. J. Anal. Sci. Technol. *12*, 25. https://doi.org/10.1186/s40543-021-00276-4.

67. Verwaaijen, B., Wibberg, D., Kröber, M., Winkler, A., Zrenner, R., Bednarz, H., Niehaus, K., Grosch, R., Pühler, A., and Schlüter, A. (2017). The Rhizoctonia solani AG1-IB (isolate 7/3/14) transcriptome during interaction with the host plant lettuce (Lactuca sativa L.). PLoS One *12*, e0177278. https://doi.org/10.1371/journal.pone.0177278.

68. Zrenner, R., Genzel, F., Verwaaijen, B., Wibberg, D., and Grosch, R. (2020). Necrotrophic lifestyle of Rhizoctonia solani AG3-PT during interaction with its host plant potato as revealed by transcriptome analysis. Sci. Rep. *10*, 12574. https://doi.org/10.1038/s41598-020-68728-2.

69. Kim, D., Paggi, J.M., Park, C., Bennett, C., and Salzberg, S.L. (2019). Graph-based genome alignment and genotyping with HISAT2 and HISAT-genotype. Nat. Biotechnol. *37*, 907–915. https://doi.org/10.1038/s41587-019-0201-4.

70. Dyer, N.P., Shahrezaei, V., and Hebenstreit, D. (2019). LiBiNorm: an htseq-count analogue with improved normalisation of Smart-seq2 data and library preparation diagnostics. PeerJ *7*, e6222. https://doi.org/10.7717/peerj.6222.

71. Love, M.I., Huber, W., and Anders, S. (2014). Moderated estimation of fold change and dispersion for RNA-seq data with DESeq2. Genome Biol. *15*, 550. https://doi.org/10.1186/s13059-014-0550-8.

STAR★METHODS

KEY RESOURCES TABLE

REAGENT or RESOURCE	SOURCE	IDENTIFIER
Antibodies		
Rabbit polyclonal anti-Aromatase (CYP19A1)	Abcam	Cat# ab18995; RRID:AB_444718
Monoclonal mouse antibody anti-SARS-CoV-2 Nucleocapsid	Synaptic Systems	Cat# HS-452 011; RRID:AB_2891261
Rabbit Anti-CD31	Acris Antibodies	Cat# AP15436PU-N; RRID:AB_1927004
Anti-CD204, MSR1 monoclonal antibody clone SRA-E5	Abnova Corporation	Cat# MAB1710; RRID:AB_ 1678864
Von Willebrand Factor VIII	Dako Agilent Pathology Solutions	Cat# A0082; RRID: AB_2315602
Monoclonal antibodies anti-Smooth Muscle Actin	Dako Agilent Pathology Solutions	Cat# M0851; RRID: AB_2313736
Polyclonal rabbit anti-CD3	Dako Agilent Pathology Solutions	Cat# A0452; RRID: AB_2335677
SARS-CoV-2 Nucleocapsid antibody	Sino Biological	Cat# 40143-MM05; RRID: AB_2827977
Anti-mouse CD68 antibody clone: FA-11	BioLegend	Cat# 137002; RRID:AB_2044004
Purified Rat Anti-Mouse CD16/CD32 (Mouse BD Fc Block™) Clone 2.4G2	BD Bioscience	Cat# 553141; RRID:AB_394656
Virus strains		
SARS-CoV-2/Germany/Hamburg/01/2020	Isolated from patients; this paper	ENA study PRJEB41216, sample ERS5312751
SARS-CoV (Frankfurt 1)	Institute of Virology Charité, Berlin, Germany	N/A
A/Hamburg/NY1580/09 (H1N1)	Isolated from patients; Otte et al.[57]	https://doi.org/10.1128/JVI.00665-15
Biological samples		
Lung tissue samples of deceased COVID-19 patients	University Hospital Hamburg-Eppendorf, Mendeley Data	Table S1 https://doi.org/10.17632/4xytrnhx76.1
Lung tissue samples of deceased COVID-19 patients	University Hospital Tübingen, Mendeley Data	Table S1 https://doi.org/10.17632/4xytrnhx76.1
Lung tissue samples of deceased COVID-19 patients	Erasmus Medical Center Rotterdam, Mendeley Data	Table S1 https://doi.org/10.17632/4xytrnhx76.1
Chemicals, peptides, and recombinant proteins		
Letrozole	Sigma-Aldrich GmbH	Cat# L6545
Testosterone enanthate	LGC Standards GmbH	MM1119.00–0250
True Nuclear Transcription Buffer Set	BioLegend	Cat# 424401
Desoxyribonuklease (Dnase I)	STEMCELL	Cat# 07470
Poly(I:C)	Sigma-Aldrich	Cat# P9582
Collagenase type 1 (C0130)	STEMCELL	Cat# 07416
Critical commercial assays		
RealStar® SARS-CoV-2 RT-PCR Kit RUO	Altona Diagnostics	Cat# 821005
QIAamp Viral RNA Mini Kit	Qiagen	Cat# 52904
InnuPREP RNA Mini Kit 2.0	IST Innuscreen	845-KS-2040250
Multi-Species Hormone Magnetic Bead Panel	Merck	Cat# MSHMAG-21K
Estradiol ELISA	Calbiotech	Cat# ES380S Cat# ES180S-100
DetectX® Testosterone ELISA Kit	Arbor Assay	Cat# AAY-K032-H
DetectX® 17β-Estradiol ELISA Kit	Arbor Assay	Cat# AAY-K030-H

(*Continued on next page*)

Continued

REAGENT or RESOURCE	SOURCE	IDENTIFIER
RNAscope™ Probe- V-nCoV2019-S-sense	Advanced Cell Diagnostics	Cat# 845701
RNAscope 2.5 HD Detection Kit	Advanced Cell Diagnostics	Cat# 322350
Deposited data		
Genome-wide transcriptomic data of the lungs of SARS-CoV-2-infected hamsters	This paper	EBI ArrayExpress server: E-MTAB-13100
Demographic information of deceased COVID-19 patients and controls	This paper	Table S1 https://doi.org/10.17632/4xytrnhx76.1
Overview of RNAseq data	This paper	Table S2 https://doi.org/10.17632/4w5z7crgsv.1
Gene ontology term enrichment for biological processes	This paper	Table S3 https://doi.org/10.17632/4y3h9kp4y8.1
Experimental models: Cell lines		
MDCK II	ATCC	Cat# CRL-2936, RRID:CVCL_B034
VeroE6	ATCC	Cat# CCL-81, RRID:CVCL_0059
Calu-3	ATCC	Cat# HTB-55
CaCo-2	ATCC	Cat# HTB-37 RRID:CVCL_0025
A-498	ATCC	Cat# HTB-44 RRID:CVCL_1056
Huh-7	Prof. Dr.Thomas Dobner, Leibniz Institute of Virology, Hamburg, Germany	N/A
DAOY	ATCC	Cat# HTB-186 RRID:CVCL_1167
Experimental models: Organisms/strains		
Syrian golden hamster (Mesocricetus auratus), RjHan:AURA	Janvier Labs	Cat# HAMST
Oligonucleotides		
Oligonucleotides sequences	This paper; Mendeley Data	Table S4 https://doi.org/10.17632/8yr83bz9b3.1
Software and algorithms		
GraphPad Prism	Dotmatics	Version 9.0.1
MyAssays	MyAssays	MyAssays Ltd 2021
FinePointe Software System	Data Sciences International	FinePointe v2.9.0
LightCycler® 96 Software	Roche	Version v1.1.0.1320
LinReg PCR Software	Ruijter et al.[58]	https://doi.org/10.1093/nar/gkp045; Version v2018.0
Visiopharm Software	Visiopharm, Hørsholm, Denmark	N/A
Data analysis of cDNA libraries	Described in Wibberg et al.[59]	https://doi.org/10.1186/s12864-016-2561-1
GOrilla	Eden et al.[60]	https://doi.org/10.1186/1471-2105-10-48
Other		
Syrian golden hamster (Mesocricetus auratus) whole genome	NCBI	RefSeq: JAFVMI010000001

RESOURCE AVAILABILITY

Lead contact

Further information and requests for resources, data and reagents should be directed to and will be fulfilled by the lead contact, Prof. Dr. Guelsah Gabriel (guelsah.gabriel@leibniz-liv.de).

Materials availability

All unique/stable reagents generated in this study are available from the lead contact Prof. Dr. Guelsah Gabriel with a completed material transfer agreement.

Data and code availability

The published article includes all datasets generated or analyzed during this study. Differential gene expression data by stranded mRNA-Seq preparation and sequencing of cDNA libraries from this study are available on the EBI ArrayExpress server (www.ebi.ac.uk/biostudies/arrayexpress), with the accession number E-MTAB-13100. This paper does not report original code. Any additional information required to reanalyze the data reported in this paper is available from the lead contact upon request.

EXPERIMENTAL MODEL AND STUDY PARTICIPANT DETAILS

GEN-COVID cohort

The post-Mendelian model uses an integrated polygenic score (IPGS) to predict COVID-19 disease severity. The model was previously trained over the GEN-COVID cohort and validated using several independent COVID-19 cohorts.[27–29] Briefly, the IPGS used to predict COVID-19 severity is a weighted average of selected features representing whole exome sequencing (WES) data in a binary format. Feature selection is performed using the least absolute shrinkage and selection operator (LASSO) over a series of logistic models trained to predict a phenotype of COVID-19 severity adjusted by age and gender (male or female was defined as self or physician reporting). Patients of the GEN-COVID cohort were first graded using the modified version of WHO COVID-19 Outcome Scale used for severity grading, as follows: 5. death; 4. hospitalized receiving invasive mechanical ventilation; 3. hospitalized, receiving continuous positive airway pressure (CPAP) or bilevel positive airway pressure (BiPAP) ventilation; 2. hospitalized, receiving low-flow supplemental oxygen; 1. hospitalized, not receiving supplemental oxygen; and 0. not hospitalized.[61] Then, two Ordered Logistic Regression (OLR) models were fitted using age to predict the ordinal grading (0, 1, 2, 3, 4, 5) dependent variable, separately for male and female cohorts. In this way, it was possible to assign to each patient clinical classification equal to 0 (milder), if the actual patient grading was below the one predicted by the OLR; or equal to 1 (more severe), if the grading was above the OLR prediction. The patients with a predicted grading equal to the actual grading were excluded from the following analyses in order to compare patients where the genetic contribution toward the more severe/milder phenotype is expected to be more relevant. In order to evaluate the significance of the association between Thr201Met CYP19A1 variant and COVID-19 severity, the Chi-Square Test was used.

Fatal COVID-19 cases and controls

Autopsy-derived lung material from male and female patients, who died of COVID-19, were obtained from three independent study sites: Hamburg, Tübingen and Rotterdam. Lung biopsies from patients how were tested negative for SARS-CoV-2 RNA in qRT-PCR were used as controls. For all deceased patients at the University Hospital Tübingen, ethical approval had been obtained from the next of kin (097/2021BO2).[62]

Cells

Calu-3 (ATCC HTB-55), Huh-7 (kindly provided by Thomas Dobner, Leibniz Institute of Virology, Hamburg, Germany), CaCo-2 (ATCC HTB-37), A-498 (ATCC HTB-44) and DAOY cells (ATCC HTB-186) were cultured in the manufacturer's recommended medium.

Animals

Male and female golden hamsters (8–12 weeks old) were purchased from Janvier. All animals were kept under standard housing conditions (21 ± 2°C, 40–50% humidity, food and water *ad libitum*) with a 12:12 light–dark cycle at the Leibniz Institute of Virology in Hamburg, Germany.

METHOD DETAILS

Viruses

The SARS-CoV-2 strain (SARS-CoV-2/Germany/Hamburg/01/2020; ENA study PRJEB41216 and sample ERS5312751) was isolated from COVID-19 patient material. Briefly, VeroE6 cells were inoculated with 200 μL of a human nasopharyngeal swab of a confirmed patient with COVID-19 in Hamburg and propagated for three serial passages in VeroE6 cells. The SARS-CoV (Frankfurt 1) was also grown and titrated in VeroE6 cells. VeroE6 were cultivated in DMEM (Sigma-Aldrich GmbH) with 2% fetal bovine serum (FBS), 1% penicillin-streptomycin and 1% L-glutamine at 37°C for virus propagation. The 2009 pandemic H1N1 influenza A virus (A/Hamburg/NY1580/09; H1N1)[57] was grown and titrated in MDCK II cells. MDCK II cells were cultivated in MEM (Sigma-Aldrich GmbH) with 0.2% bovine serum albumin (BSA), 1% penicillin-streptomycin and 1% L-glutamine and 1 μg ml^{-1} L-1-tosylamido-2-phenylethyl chloromethyl ketone (TPCK) trypsin (Sigma-Aldrich GmbH) at 37°C. All cells were tested negative for Mycoplasma sp. by PCR. All infection experiments with SARS-CoV and SARS-CoV-2 were performed in the biosafety level 3 (BSL-3) laboratory at the Leibniz Institute of Virology in Hamburg, Germany.

Animal experiments

For SARS-CoV-2 infection, male and female hamsters were anesthetized with 150 mg/kg ketamine and 10 mg kg^{-1} xylazine by intraperitoneal injection. The animals were intranasally inoculated with 10^5 plaque-forming units (p.f.u.) SARS-CoV-2, mock infected with PBS or were administered with 1 mg kg^{-1} poly(I:C). Letrozole dosing was calculated for male and female hamsters by taking

sex-specific half times into consideration as reported before.[45–47,63,64] For letrozole treatment, male and female hamsters received a final dose of 0.36 mg kg^{-1} d^{-1} or 0.18 mg kg^{-1} d^{-1} letrozole, respectively, (dissolved in DMSO, Sigma-Aldrich GmbH) diluted in sterile saline (Braun), respectively, by oral gavage (stainless-steel gavaging needles) at 3 h and day 1–3 post infection (p.i.). As control, hamsters were treated by oral gavage with DMSO as vehicle. To reduce stress induced by oral gavaging according to animal welfare regulations, after day 4 p.i. until day 8 p.i., hamsters were offered letrozole or DMSO as a vehicle control via water gel packages (Necta) supplemented with 1% glucose and a final concentration of 0.0018 mg mL-1 or 0.0036 mg mL^{-1} letrozole for female and male hamsters, respectively. For testosterone treatment, male hamsters received 1 mg kg^{-1} or 10 mg kg^{-1} testosterone enanthate (dissolved in sesame oil) by subcutaneous injection at 3 h and 3 days p.i. As control, PBS-treated or infected male hamsters were treated subcutaneously with sesame oil as vehicle.

Body weight was monitored daily up to 14 or 21 days post infection (d p.i.). On day 1, 3, 6, 14 or 21 p.i., five to ten animals per group were euthanized by intraperitoneal injection of an overdose of pentobarbital (800 mg/kg). Blood was drawn by cardiac puncture and collected in EDTA tubes. Blood was centrifuged for 10 min at 3,000 g and 4°C, and the plasma was stored at −80°C. Lungs, brains and gonads were homogenized in 1x PBS and supernatants were stored at −80°C. For histopathological examination, lungs, brains and gonads were fixed by immersion in 10% neutral-buffered formalin and embedded in paraffin. For total RNA isolation, lungs, brains and gonads were incubated in RNAprotect Tissue Reagent (QIAGEN), for at least 24 h at 4°C and stored at −80°C.

All animal experiments were performed in strict accordance with the guidelines of German animal protection law and were approved by the relevant German authority (Behörde für Gesundheit und Verbraucherschutz; protocols N 032/2020, N 103/2020 and N 108/2022).

Histology and immunohistochemistry in fatal COVID-19 cases

For immunohistochemical detection of CYP19A1 in the lungs of deceased male and female COVID-19 patient's tissue probes were fixed in 4% phosphate-buffered formaldehyde and embedded in paraffin. Demographic information of deceased COVID-19 patients and controls are listed in Table S1, available at Mendeley Data: https://doi.org/10.17632/4xytrnhx76.1.

For immunohistochemistry at the University Hospital Hamburg-Eppendorf, sections were cut at 2 μm. After dewaxing and inactivation of endogenous peroxidases (PBS/3% hydrogen peroxide), antibody specific antigen retrieval was performed using the Ventana Benchmark XT machine (Ventana, Tuscon, Arizona, USA). Sections were incubated with anti-CYP19A1 (1:400) or anti-SARS-CoV-2 nucleoprotein antibody (1:2,000). For detection of specific binding, the Ultra View Universal DAB Detection Kit (Ventana, Roche) was used, which contains secondary antibodies, DAB stain and counter staining reagent for detection of nuclei. Staining were evaluated by an experience pathologist and representative images were taken with a Leica DMD108 digital microscope.

For immunohistochemistry at the University Hospital Tübingen, immunohistochemical analysis was performed by using the polyclonal antibody directed against CYP19A1 (1:400) on an automated immunostainer following the manufacturer's protocol (Benchmark; Ventana Medical Systems, Tucson, AZ) and using the ultraView detection system (Ventana) and diaminobenzidine as substrate.

For immunohistochemistry at the Erasmus Medical Center Rotterdam, immunohistochemistry was performed with an automated, validated and accredited staining system (Ventana, Tuscon, Arizona, USA) using optiview universal DAB detection Kit. In brief, following deparaffinization and heat-induced antigen retrieval for 32 min with CC1 the tissue samples were incubated with rabbit-*anti*-human CYP19A1 (1:400) for 32 min. Incubation was followed by hematoxylin II counter stain for 12 min and then a blue coloring reagent for 8 min according to the manufactures instructions (Ventana, Tuscon, Arizona, USA).

In situ hybridization (ISH)

To detect SARS-CoV-2 RNA, lung tissue sections were hybridized using specific probes for SARS-CoV-2 (ACD, Newark, CA, USA) followed by the RNAscope 2.5 HD Detection Kit Red from ACD (Newark, CA, USA) according to the manufacturer's protocol.

Plethysmography

Respiratory function was assessed using an unrestrained barometric whole-body plethysmography. In brief, Syrian golden hamsters infected with SARS-CoV-2 or mock infected with PBS were placed in a sealed cylindrical Buxco WBP chamber (Rat WBP standard chamber) on day 0, 6, 14 and/or 21 p.i., and changes in pressure caused by tidal breathing movements were measured using a volumetric flow transducer (FP WBP Flow Transducer w/T&HF, Data Sciences International) and amplified. Flow fluctuations were recorded using FinePointe Software System (v2.9.0, Data Sciences International). At the beginning of each session, the plethysmograph was calibrated. Several parameters were obtained, including breath frequency (breaths/min), tidal volume (Ti, ml), expiratory flow rate at the point 50% of tidal volume is expired (EF50, ml/s), peak inspiratory flow rate (PIFb, ml/s), peak expiratory flow rate (PEFb, ml/s), minute volume (mL/min), end inspiratory pause (EIP, ms), end expiratory pause (EEP, ms), inspiratory time (Ti, sec) and expiratory time (Te, sec). Measurements were performed for 10 min, after 20 min (females) or 30 min (males) acclimatization periods.

Histology and immunohistochemistry in hamsters

Tissues were routinely embedded in paraffin and evaluated via light microscopy of hematoxylin and eosin (HE) as well as Azan stained slides.

Immunohistochemical detection of SARS-CoV-2 nucleoprotein (NP), CYP19A1, cluster of differentiation (CD) 204, von-Willebrandt-factor (vWF), CD31, CD3 and smooth muscle actin (SMA) in the golden hamster lungs was performed using the EnVision+ System (Dako Agilent Pathology Solutions). Serial sections of tissue were dewaxed and rehydrated in isopropanol and 96% ethanol followed by blockage of endogenous peroxidase by incubation in 85% ethanol with 0.5% H_2O_2 for 30 min at room temperature. Antigen retrieval was performed by incubation in citrate (10 mM citric acid, 0.05% Tween 20) or citrate-Na_2H_2EDTA buffer (10 mM citric acid, 2 mM Na_2H_2EDTA, 0.05% Tween 20) for 20 min in a microwave at 800 W, followed by 20 min at room temperature. Sections were afterward transferred to Shandon Coverplates (Thermo Electron GmbH) and stained with either polyclonal antibodies directed against CYP19A1 (1:500), CD31 (Acris, 1:100), CD204 (Abnova Corporation, 1:500) and vWF (Dako Agilent Pathology Solutions, 1:500) or monoclonal antibodies against SMA (Dako Agilent Pathology Solutions, 1:100), CD3 (Dako Agilent Pathology Solutions, 1:100) and SARS-CoV-2 NP (Sino Biological, 1:32,000) over night at 4°C. Antibodies were diluted in 1x PBS containing 1% BSA and addition of 0.3% Triton X-100 for the CYP19A1, SMA and SARS-CoV-2 NP stainings. Sections were subsequently rinsed, and the peroxidase-labeled polymer was applied as secondary antibody for 30 min. Visualization of the reaction was accomplished by incubation in chromogen 3,3-diaminobenzidine tetrahydrochloride (DAB, 0.05%) and 0.03% H_2O_2 in 1x PBS for 5 min and afterward counterstained with Mayer's hematoxylin for 1 min. For negative controls, the primary antibody was replaced by either rabbit normal serum (1:3,000) or ascites fluid from Balb/c mice (1:1,000). The serial stainings were afterward analyzed by light microscopy.

For the detection of collagen, picro sirius red stain kit (PSR-1-IFU, Sky tekLogan, Utah, USA) was used according to the instructions of the manufacturer.

For the quantification of Azan positive collagen fiber content in the lungs and CYP19A1 expressing tissue in lungs and gonads, slides were digitized using the Hamamatsu NanoZoomer S210 (Hamamatsu Photonics, Herrsching am Ammersee, Germany) slide scanner. Image analysis was performed on the whole-slide images. Initially lung tissue was detected using a specifically trained Bayesian classifier followed by DAB positive and negative (tissue) pixel count for CYP19A1 staining or Azan positive and negative pixel count for collagen detection using the Visiopharm Software (Visiopharm, Hørsholm, Denmark). Percentage of CYP19A1 positive tissue and Azan positive collagen fiber content was calculated for each lung section present on a slide individually and a median expression value was calculated for each animal.

Determination of virus titers and viral RNA levels

Homogenization of organs was performed in 1 mL 1x PBS with 5 sterile, stainless steel beads (Ø 2 mm, Retsch) at 30 Hz for 10 min in the mixer mill MM400 (Retsch).

For determination of the virus titer, tissue homogenates and cell culture supernatants were titrated for SARS-CoV and SARS-CoV-2 on VeroE6 cells and for H1N1 on MDCK cells in 10-fold serial dilutions for 30 min at 37°C and overlaid with MEM (Sigma-Aldrich GmbH) supplemented with 0.2% BSA, 1% L-glutamine, 1% penicillin-streptomycin, 1.25% Avicel and 1 $\mu g\ mL^{-1}$ Trypsin-TPCK (only for H1N1). After 72 h p.i., cells were washed with 1x PBS, fixed with 4% paraformaldehyde and the plaques were visualized by crystal violet staining.

Viral RNA was isolated from homogenized organs using the QIAamp Viral RNA Mini Kit (QIAGEN) according to the manufacturer's instructions. SARS-CoV-2 RNA levels were then determined by quantitative reverse transcription real-time PCR (qRT-PCR) using the RealStar SARS-CoV-2 RT-PCR Kit RUO (Altona Diagnostics). An internal control provided by the kit was used as a sample preparation control as well as an extended dry spin step for 10 min at 17,000 g at room temperature.

Measurement of hormone and cytokine/chemokine levels

Testosterone levels were measured in plasma samples using a custom-made MILLIPLEX MAP Multi-Species Hormone Magnetic Bead Panel (Merck), according to the manufacturer's instructions in a Bio-Plex 200 System with high-throughput fluidics (HTF; Bio-Rad). Estradiol levels in plasma samples were analyzed by ELISA following the manufacturer's instructions. Female hamsters in diestrus were excluded from estradiol analysis. Testosterone and Estradiol levels (Arbor Assays) in cell culture supernatants were measured by ELISA following the manufacturer's instructions. All ELISAs were measured on an Infinite M Nano ELISA microplate reader (Tecan).

A panel of 13 cytokines and chemokines (eotaxin, macrophage inflammatory protein 1α and 1β (MIP-1α, -1β), interferon-γ (IFN-γ), interleukin-2 (IL-2), interleukin-6 (IL-6), interleukin-10 (IL-10), interleukin-12 (IL-12(p70)), interleukin-13 (IL-13), interleukin-1β (IL-1β), monocyte chemoattractant protein-1 (MCP-1), tumor necrosis factor alpha (TNF-α), and vascular endothelial growth factor (VEGF)) was measured in homogenized lungs using a custom-made Bio-Plex Pro Mouse Cytokine multiplex (Bio-Rad) according to the manufacturer's instructions in a Bio-Plex 200 System with high-throughput fluidics (HTF; Bio-Rad). Values measured below detection limit were set to the lower limit of detection specified in the manufacturer's instruction.

Infection of human cells with respiratory viruses

Calu-3, Huh-7, CaCo-2, A-498 and DAOY cells were seeded in 6-well plates. After 24 h, cells were infected with SARS-CoV, SARS-CoV-2 or H1N1 at a multiplicity of infection (MOI) of 0.5 in 500 μL EMEM with 1% penicillin-streptomycin, 1% L-glutamine and 2% FBS or EMEM with 1% penicillin-streptomycin, 1% L-glutamine and 0.4% BSA, respectively, for 45 min at 37°C. After washing twice with 1x PBS, 2 mL of infection medium EMEM with 1% penicillin-streptomycin, 1% L-glutamine and 2% FBS or EMEM with

1% penicillin-streptomycin, 1% L-glutamine, 0.2% BSA and 1 μg/mL TPCK-treated Trypsin (Sigma-Aldrich GmbH) were added and the cells were incubated for 24 h at 37°C.

Aromatase activity in SARS-CoV-2-infected Calu-3 cells

Calu-3 were seeded in 6-well plates. After 24 h, cells were infected with SARS-CoV-2 at an MOI of 0.01 in 500 μL EMEM with 1% penicillin-streptomycin, 1% L-glutamine and 2% charcoal-stripped FBS for 45 min at 37°C. At 24 h p.i., cells were treated with 100 nM testosterone and 1 μM letrozole or as control with DMSO. Testosterone and estradiol levels were measured in cell culture supernatants at 24 h post treatment and 48 h p.i.

Isolation and poly(I:C) treatment of lung macrophages from golden hamsters

Male and female hamsters were euthanized by intraperitoneal injection of an overdose of pentobarbital (800 mg/kg). Lungs were perfused with PBS and digested with 2 mL of collagenase (1 mg mL^{-1}) and deoxyribonuclease (0.5 mg mL^{-1}) for 1 h at 37°C.[65] After the digestion, lung cells were filtered through a 40 μm filter, resuspended and seeded in 12-well plate. Isolated macrophages were cultivated in RPMI medium (Sigma-Aldrich) with 10% FBS, 0.5% penicillin-streptomycin and 1% L-glutamine. After 7–10 days, macrophage cell purity was determined via FACS analysis using anti-mouse CD68 antibody (BioLegend). Cells were incubated with FC block antibody (2.4G2: BD Bioscience) and then fixed for 1 h at RT with True Nuclear Transcription Buffer Set (BioLegend). Cells were stained with CD68 antibody (BioLegend) in Perm Buffer (BioLegend) for 45 min at 4°C. Cells were acquired with Cytek Aurora (Biosciences). The expression of CD68 was assessed with FlowJo software (Treestar). Poly(I:C) treatment was started with >85% CD68 positive macrophage cultures. Macrophages were treated with 5 μg mL^{-1} and 10 μg mL^{-1} poly(I:C) or as a control treated with PBS for 24 h at 37°C.

RNA isolation

RNAprotect-fixed tissues were homogenized in 1 mL TRIZOL (Invitrogen) with 5 sterile, stainless steel beads (Ø 2 mm, Retch) at 30 Hz for 10 min in the mixer mill MM400 (Retsch). Cells were lysed in 500 μL or 1 mL TRIZOL (Invitrogen) per well, according to the well size, incubated for 5 min at RT. The cell lysate was resuspended and transferred into a fresh tube. 125 μL or 250 μL chloroform were added respectively to each sample, vortexed for 30 s and subsequently centrifuged for 15 min at 13,000 g.

Total RNA was isolated from homogenized tissues and the aqueous phase of the lysed cells using the innuPREP RNA Mini Kit 2.0 (Analytik Jena) according to the manufacturer's instructions with an additional on column DNase I treatment using the RNase-free DNase Set (QIAGEN).

Total RNA from formalin-fixed, paraffin-embedded human lung tissue sections was purified using the RNeasy@ FFPE Kit (Qiagen) according to the manufacturer's instructions. The RNA was eluted in RNase-free water and mixed with 1 U μl^{-1} RiboLock RNase inhibitor (Thermo Fisher Scientific).

Determination of mRNA expression levels by real-time quantitative PCR (RT-qPCR)

The cDNA synthesis was performed using random nonamer primers (Gene Link, pd(N)9, final concentration: 5 μM), SuperScript III Reverse Transcriptase (Thermo Fisher Scientific) according to the manufacturer's instructions and 2 μg total RNA. The cDNA was generated using the GeneAmp PCR System 9700 (Applied Biosystems; cycle: 25°C for 5 min, 50°C for 60 min, 70°C for 15 min, 4°C hold). Reactions were set up with PCR grade Water (Roche) in LightCycler 480 Multiwell Plate 96 Reaction Plates (Roche). Briefly, 2 μL of cDNA template were added to 10 μL FastStart Essential DNA Green Master (Roche) and 300 nM of forward and reverse primer, respectively. RT-qPCR runs were conducted using LightCycler 96 Real-Time PCR System (Roche) with endpoint fluorescence detection: 10 min at 95°C and 45 amplification cycles (15 s at 95°C, 10 s at 65°C and 20 s at 72°C). Analysis was performed in duplicates for each gene. Negative controls and samples without reverse transcriptase were included to detect contaminations.

Relative expression values were determined using a modified E–ΔΔCt method. Rn-values were exported from the LightCycler 96 Software (Roche) to Microsoft Office Excel 2016 and N0-value for the starting concentration of the transcript in the original sample were obtained with LinReg PCR Software v2018.0.[58] The averaged N_0-value of the gene of interest (GOI) was then normalized with the average N_0-value for HPRT ($N_{0(HPRT)}$) or RPL32 ($N_{0(RPL32)}$) of the respective sample. The relative $N_{0(GOI)}/N_{0(HPRT)}$- or $N_{0(GOI)}/N_{0(RPL32)}$-expression values of the biological replicates are presented.

In hamsters, HPRT (Hypoxanthin phosphoribosyltransferase 1) was used as a reference gene for analyses of mRNA expression levels in the lung as well as in the brain. YWHAZ (Tyrosine 3-Monooxygenase/Tryptophan 5-Monooxygenase Activation Protein Zeta) was used as a reference gene for analyses of mRNA expression levels in the gonads. In human samples, RPL32 (ribosomal protein L32) was used as a reference gene for analyses of mRNA expression levels in the lung as well as in the colon. β-actin (ACTB) was used as a reference for analyses of mRNA expression levels gene in the liver as well as in the kidney and cytochrome *c*1 (CYC1) was used as reference for the brain. The primer sequences used for RT-qPCR are listed in Table S4, available at Mendeley Data: https://doi.org/10.17632/8yr83bz9b3.1.

Letrozole detection by high-performance liquid chromatography (HPLC)

Concentration of letrozole in plasma and lung tissue was measured using an isocratic high-performance liquid chromatography (HPLC) system (Shimadzu, Duisburg, Germany) and was based on the method published before.[66]

For extraction of letrozole, serum and supernatant of lung tissue lysate were mixed with 0.1% *o*-Phosphoric acid and icecold acetonitrile was added. Following centrifugation (serum: 10 min, 15,000 rpm 10°C; lung: 20 min, 15,000 rpm, 4°C; Multifuge 1 S-R, Heraeus, Hanau, Germany) the supernatant was filtered through a 0.2 μm centrifugal filter unit (15 min, 3,500 rpm at 4°C, VWR International, Radnor, USA). Filtrates were frozen at −30°C until HPLC injection.

Measurements were performed using the following HPLC equipment: an LC-20 AT pump, degasser unit DGU-20A, oven CTO-20A set at 35°C, UV detector SPD-20A set at 240nm, CBM-20A prominence controller (Shimadzu, Kyoto, Japan). The mobile phase consisted of 20 mM ammonium acetate (pH 5.5) and acetonitrile (60:40, v/v). The flow rate was 1 mL/min and the injections were carried out through a 20 μL loop. Separations were obtained on a pre column and a main column (Nucleosil 120-5, C18, 50/4 and Nucleosil 120-5 C18, 250/4, Macherey und Nagel, Düren, Germany). Letrozole 96% (Sigma Aldrich GmbH) was used as an internal control. Linearity of letrozole: 0.01 μg/mL serum – 20.0 μg/mL serum and 0.068 μg/g lung – 77.85 μg/g lung. LLOQ of letrozol: 0.01 μg/mL serum and 0.068 μg/g lung.

Differential gene expression analysis by stranded mRNA-Seq preparation and sequencing of cDNA libraries

Preparation of stranded cDNA libraries was performed with Illumina Stranded mRNA Prep, Ligation kit, starting with 1000 ng total RNA according to the manufacturer's instructions.

Sequencing of the prepared stranded cDNA libraries was performed on an Illumina NextSeq 550 platform (Illumina Inc., San Diego, U.S.A.). In total, 30 cDNA libraries were paired-end sequenced in rapid mode with 2 × 75 cycles in two runs. Data analysis and base calling were accomplished with an in-house software platform as recently described.[59]

In total, 103 Gb sequence data were obtained for the 30 cDNA libraries, with an average of about 3.3 Gb (lowest 2.8 Gb) per library. The sequencing raw data for all libraries has been made available on the EBI ArrayExpress server (www.ebi.ac.uk/arrayexpress), with the accession number E-MTAB-13100.

Transcript mapping and differential gene expression analysis

Read mapping and analyses were carried out as described recently with modifications.[67,68] In brief, the obtained reads were quality filtered (>Q30), trimmed and subsequently mapped to the 2.0 version of the Mesocricetus auratus (Syrian golden hamster) genome (RefSeq: JAFVMI010000001:JAFVMI010007057) using HISAT2 v.2.1.0[69] with default settings. Two mismatches were allowed to handle possible sequencing errors and allelic variants of the diploid genome. The mapping data is available on the EBI ArrayExpress server (www.ebi.ac.uk/arrayexpress), with the accession number E-MTAB-13100. For transcript abundance analysis, resulting datasets were imported into LibiNorm[70] producing files that contain read count information, the normalized expression for each gene, calculated as TPM (Transcripts Per Million) values, with the RNA length used having been adjusted based on the bias that was identified for RNA of that length. In total, nine differential expression analyses with five replicates per groups were performed with DESeq2.[71] An overview of the comparisons can be found in Table S2 available at Mendeley Data: https://doi.org/10.17632/4w5z7crgsv.1. For DESeq2 calculations, the genes were counted as differentially expressed with an adjusted p-value of less than 0.05 and a minimum fold change of 1 or more. Gene Ontology (GO) term enrichment was performed with GOrilla[60] including all genes with a p-value of less than 0.05 and a minimum fold change of 1 or more (Table S3, available at Mendeley Data: https://doi.org/10.17632/4y3h9kp4y8.1).

QUANTIFICATION AND STATISTICAL ANALYSIS

All data were analyzed with Microsoft Office Excel 2016 and GraphPad Prism (version 9.0.1) using ordinary one-way analysis of variance (ANOVA) followed by Tukey's multiple comparisons test, ordinary two-way ANOVA followed by uncorrected Fisher's LSD test, unpaired or paired Student's *t* test, or Mann-Whitney test as indicated in the respective legends. Statistical significance was defined as $p \leq 0.05$ (*$p \leq 0.05$, **$p < 0.01$, ***$p < 0.001$). Outlier calculation were performed by using GraphPad outlier calculator. Additionally, ELISA data were evaluated using the "Four Parameter Logistic Curve" online data analysis tool, MyAssays Ltd., 25 th October 2012, http://www.myassays.com/four-parameter-logistic-curve.assay.

Cell Reports Medicine, Volume *4*

Supplemental information

CYP19A1 mediates severe SARS-CoV-2 disease outcome in males

Stephanie Stanelle-Bertram, Sebastian Beck, Nancy Kouassi Mounogou, Berfin Schaumburg, Fabian Stoll, Amirah Al Jawazneh, Zoé Schmal, Tian Bai, Martin Zickler, Georg Beythien, Kathrin Becker, Madeleine de la Roi, Fabian Heinrich, Claudia Schulz, Martina Sauter, Susanne Krasemann, Philine Lange, Axel Heinemann, Debby van Riel, Lonneke Leijten, Lisa Bauer, Thierry P.P. van den Bosch, Boaz Lopuhaä, Tobias Busche, Daniel Wibberg, Dirk Schaudien, Torsten Goldmann, Anna Lüttjohann, Jenny Ruschinski, Hanna Jania, Zacharias Müller, Vinicius Pinho dos Reis, Vanessa Krupp-Buzimkic, Martin Wolff, Chiara Fallerini, Margherita Baldassarri, Simone Furini, Katrina Norwood, Christopher Käufer, Nina Schützenmeister, Maren von Köckritz-Blickwede, Maria Schroeder, Dominik Jarczak, Axel Nierhaus, Tobias Welte, Stefan Kluge, Alice C. McHardy, Frank Sommer, Jörn Kalinowski, Susanne Krauss-Etschmann, Franziska Richter, Jan von der Thüsen, Wolfgang Baumgärtner, Karin Klingel, Benjamin Ondruschka, GEN-COVID Multicenter Study Group, Alessandra Renieri, and Gülsah Gabriel

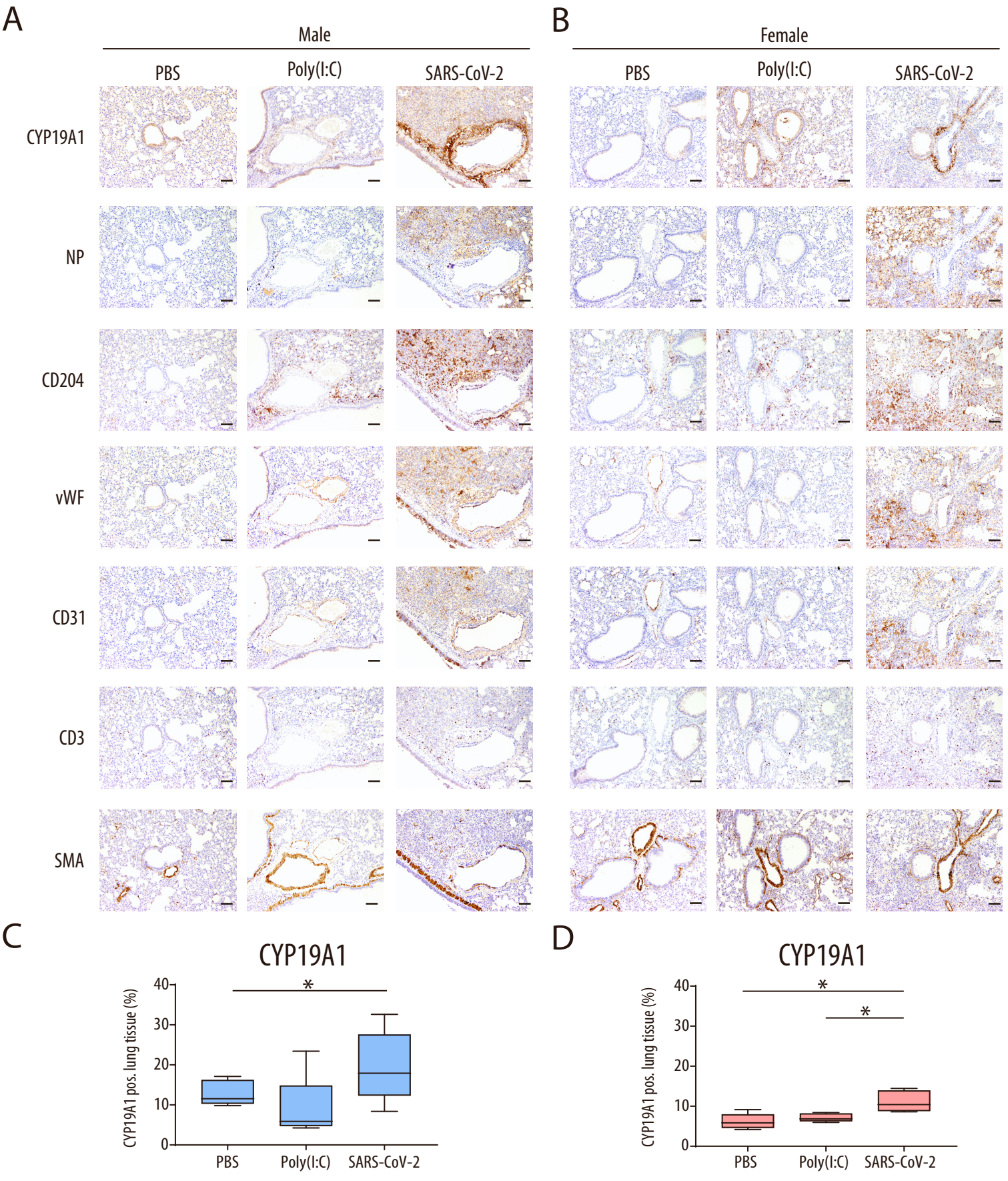

Figure S1. CYP19A1 protein expression in the lungs of SARS-CoV-2 infected male and female golden hamsters, Related to Figure 3.

(A, B) Immunohistochemistry of serial sections from the lungs of SARS-CoV-2 infected and control treated (PBS, Poly(I:C)) male (A) and female (B) golden hamsters for CYP19A1, SARS-CoV-2 NP, macrophages (CD204), endothelial cells (vWF and CD31), T cells (CD3) and smooth muscle actin (SMA). Representative pictures of each group are shown ($n = 5$). Scale bar, 100 µm. (C, D) Quantification of CYP19A1 expressing tissue in the lungs of SARS-CoV-2 infected and control treated (PBS, Poly(I:C)) male (C) and female (D) golden hamsters ($n = 5$). Data from PBS treated animals are also shown in Figure 3B. Data are shown as a box and whisker plot. Statistical significance was assessed by one-way ANOVA (*$p \leq 0.05$).

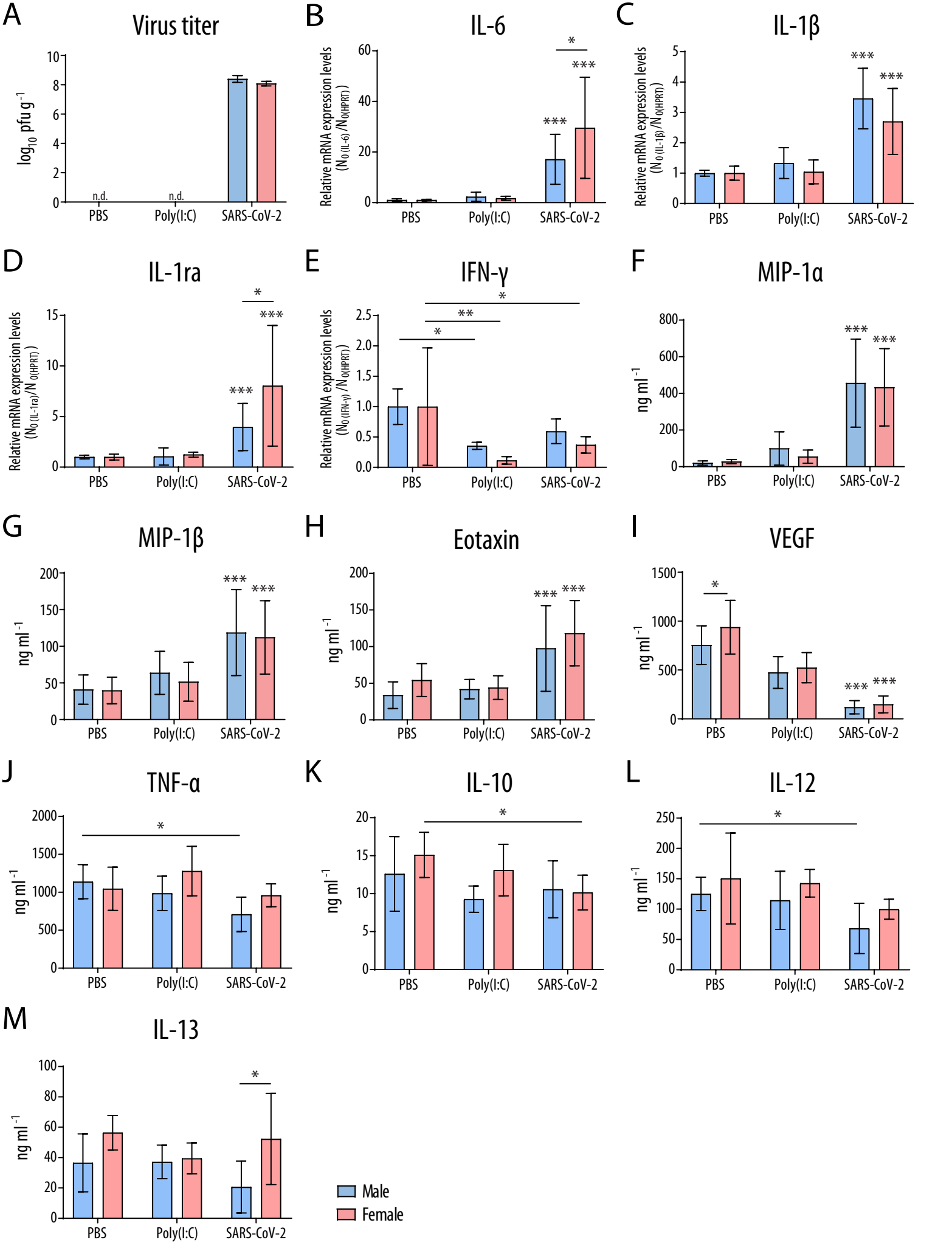
A
Virus titer
log10 pfu g-1
n.d.
n.d.
PBS
Poly(I:C)
SARS-CoV-2
B
IL-6
Relative mRNA expression levels (N0 (IL-6) /N0(HPRT))
C
IL-1β
Relative mRNA expression levels (N0 (IL-1β) /N0(HPRT))
D
IL-1ra
Relative mRNA expression levels (N0 (IL-1ra)/N0(HPRT))
E
IFN-γ
Relative mRNA expression levels (N0 (IFN-γ) /N0(HPRT))
F
MIP-1α
ng ml-1
G
MIP-1β
ng ml-1
H
Eotaxin
ng ml-1
I
VEGF
ng ml-1
J
TNF-α
ng ml-1
K
IL-10
ng ml-1
L
IL-12
ng ml-1
M
IL-13
ng ml-1
Male
Female

Figure S2. Virus replication and immune response in lungs of SARS-CoV-2 infected male and female golden hamsters, Related to Figure 3.

(A) Viral lung titers of infected male and female golden hamsters on day 3 p.i. (*n* = 5). Data of viral lung titers are also shown in Figure 4A, F, K and P. (B-E) IL-6 (B), IL-1β (C), IL-1 receptor antagonist (ra) (D) and IFN-γ (E) mRNA expression levels in SARS-CoV-2 infected male and female golden hamsters at day 3 p.i. (*n* = 5, male Poly(I:C): *n* = 4). Relative mRNA expression values in PBS treated hamsters were set to 1 after normalization against HPRT. (F-M) MIP-1α (*n* = 5) (F), MIP-1β (*n* = 5) (G), eotaxin (*n* = 5; male Poly(I:C): *n* = 4) (H), VEGF (*n* = 4; SARS-CoV-2: *n* = 3) (I), TNF-α (*n* = 5) (J), IL-10 (*n* = 5) (K), IL-12 (*n* = 5) (L) and IL-13 (*n* = 5) (M) protein expression levels in SARS-CoV-2 infected male and female golden hamsters at day 3 p.i.. Values are shown as means; error bars are shown as SD. Statistical significance was assessed by two-way ANOVA (*$p \leq 0.05$, **$p<0.01$, ***$p<0.001$).

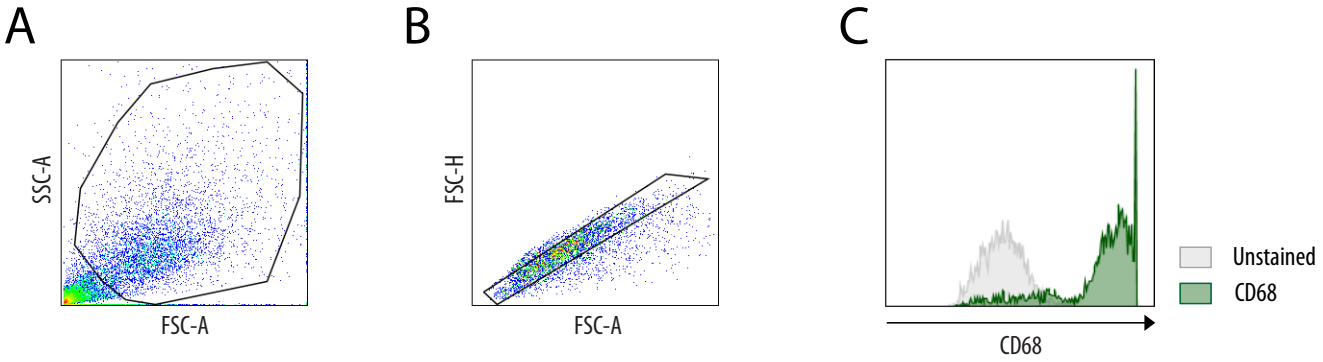

Figure S3. Characterization of ex vivo lung macrophages of golden hamsters, Related to Figure 3.

(A-C) Macrophages were isolated from the lung of a male hamster and their purity was assessed using fluorescence-activated cell sorting (FACS). Shown is the FACS gating strategy, including the removal of dead cells (A) and cell aggregates (B) via the use of forward and side scatter characteristics. Macrophages were stained using the macrophage marker protein CD68 (C).

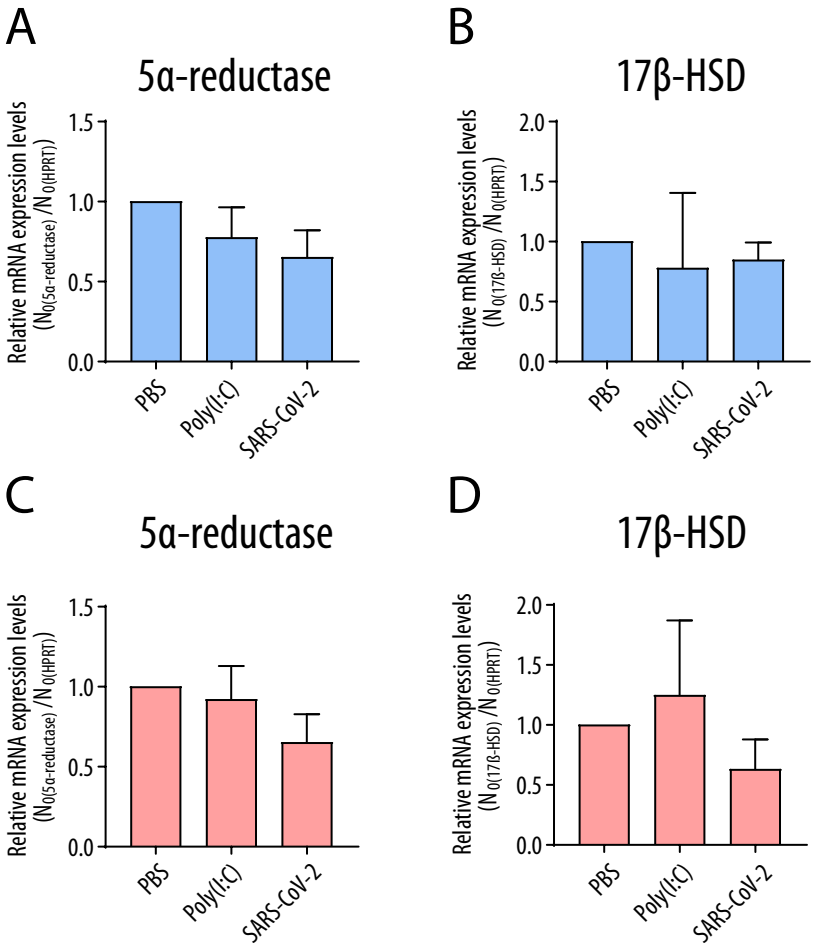

Figure S4. 5α-reductase and 17β-hydroxysteroid-dehydrogenase levels in the lungs of SARS-CoV-2 infected of male and female golden hamsters, Related to Figure 3.

(A, C) 5α-reductase mRNA expression levels measured in the lungs of SARS-CoV-2 infected and control treated (PBS, Poly(I:C)) male (A) and female (C) golden hamsters at day 3 p.i.. (B, D) 17β-hydroxysteroid-dehydrogenase (17β-HSD) mRNA expression levels measured in the lungs of SARS-CoV-2 infected and control treated (PBS, Poly(I:C)) male (B) and female (D) golden hamsters at day 3 p.i.. Relative mRNA expression values in PBS treated hamsters were set to 1 after normalization against HPRT. Values are shown as means; error bars are shown as SD (n = 5, male Poly(I:C): n = 4).

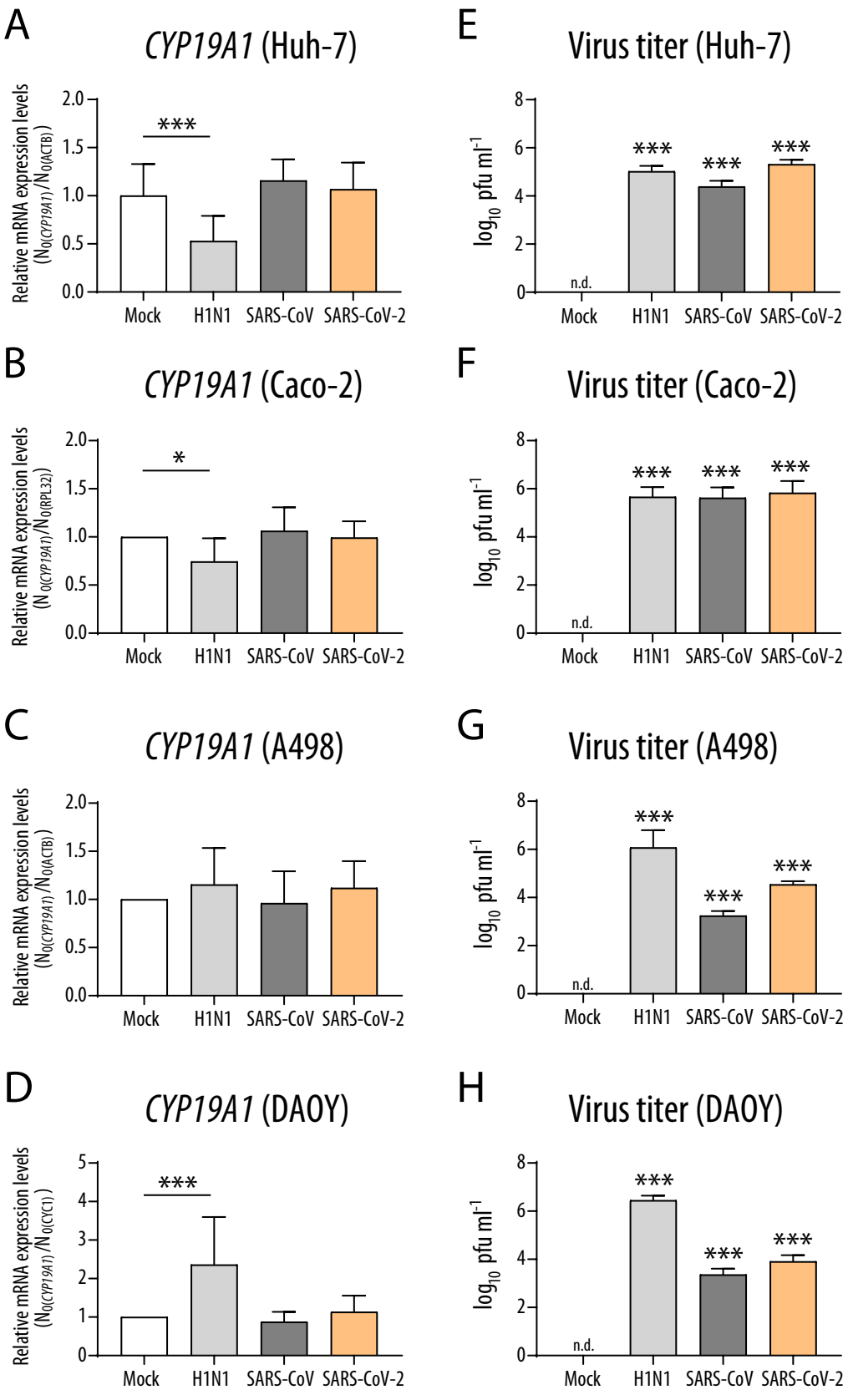

Figure S5. CYP19A1 mRNA expression in non-respiratory cell lines after respiratory virus infection, Related to Figure 3.

CYP19A1 mRNA expression levels (A-D) and virus titers (E-H) in Huh-7 (A, E), Caco-2 (B, F), A498 (C, G) and DAOY (D, H) cells control treated (Mock) or infected with H1N1 influenza A virus, SARS-CoV and SARS-CoV-2 (MOI 0.5) at 24 h p.i.. Shown is a merge of two to three independent biological replicates, each performed in technical triplicates. Relative CYP19A1 mRNA expression values in Mock treated cells were set to 1 after normalization against the cell type specific housekeeping genes ACTB (A, C), RPL32 (B) or CYC1 (D). n.d., not detected. Values are shown as means; error bars are shown as SD. Statistical significance was assessed by one-way ANOVA with multiple comparisons showing significant differences between Mock and infected cells (*$p \leq 0.05$, **$p<0.01$, ***$p<0.001$).

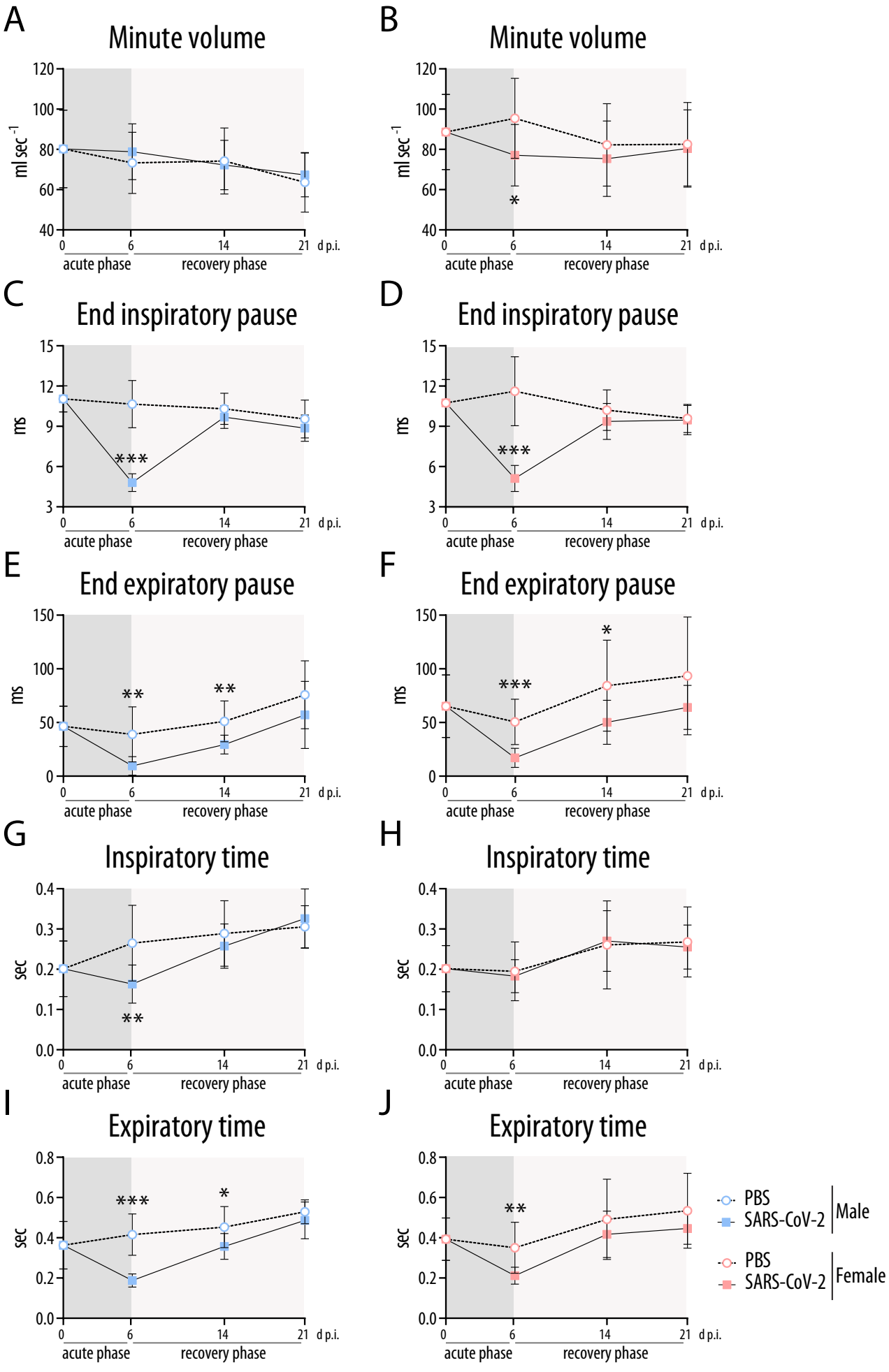
A
Minute volume
ml sec -1
120
100
80
60
40
0
6
14
21
d p.i.
acute phase
recovery phase
B
Minute volume
ml sec -1
*
C
End inspiratory pause
ms
15
12
9
6
3
***
D
End inspiratory pause
ms
***
E
End expiratory pause
ms
150
100
50
0
**
**
F
End expiratory pause
ms
***
*
G
Inspiratory time
sec
0.4
0.3
0.2
0.1
0.0
**
H
Inspiratory time
sec
I
Expiratory time
sec
0.8
0.6
0.4
0.2
0.0
***
*
J
Expiratory time
sec
**
PBS
SARS-CoV-2
Male
PBS
SARS-CoV-2
Female

Figure S6: Lung plethysmography in SARS-CoV-2 infected male and female golden hamsters, Related to Figure 5.

Whole-body plethysmography assessment of lung function parameters in SARS-CoV-2 infected or control (PBS) treated male (A, C, E, G, I) and female hamsters (B, D, F, H, J) at the indicated time points (n = 10; day 0 p.i. n = 12): Minute volume (A, B), end inspiratory pause (C, D), end expiratory pause (E, F), inspiratory time (G, H) and expiratory time (I, J). Values are shown as means; error bars are shown as SD. Statistical significance was assessed by unpaired Student´s t-test (*$p \leq 0.05$, **$p<0.01$, ***$p<0.001$).

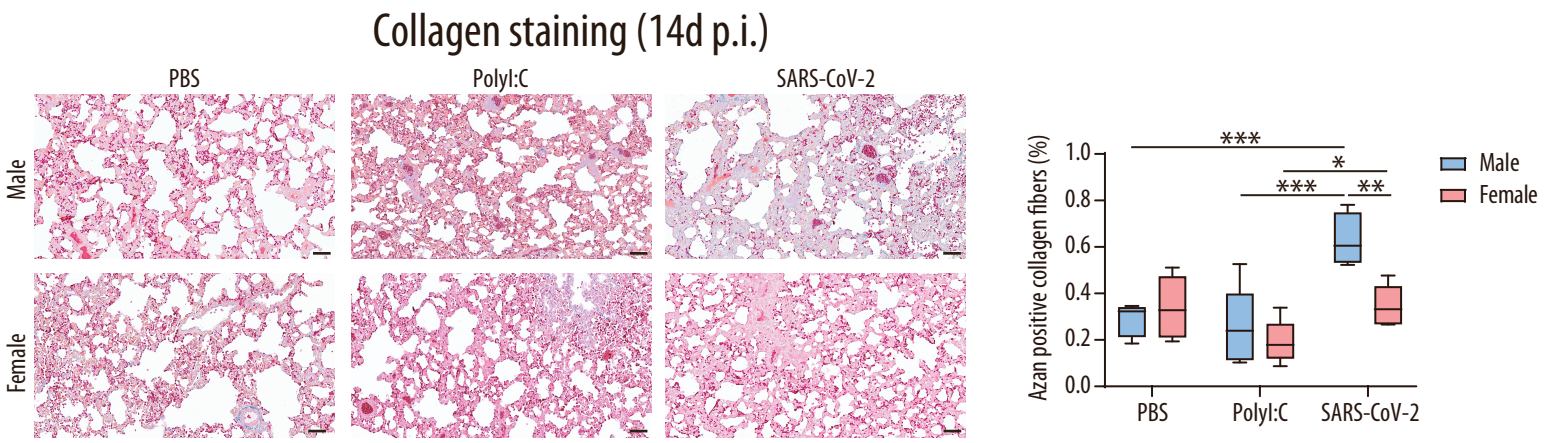

Figure S7. Lung histopathology of SARS-CoV-2 infected golden hamsters, Related to Figure 5.

Collagen staining with Azan of lung sections (left panel) and quantification thereof (right panel) from control (PBS) or SARS-CoV-2 infected male and female golden hamsters at day 14 p.i. (n = 4-5). Scale bar, 50 µm. Values are shown as means; error bars are shown as SD. Statistical significance was assessed by two-way ANOVA (*$p \leq 0.05$, **$p<0.01$, ***$p<0.001$).

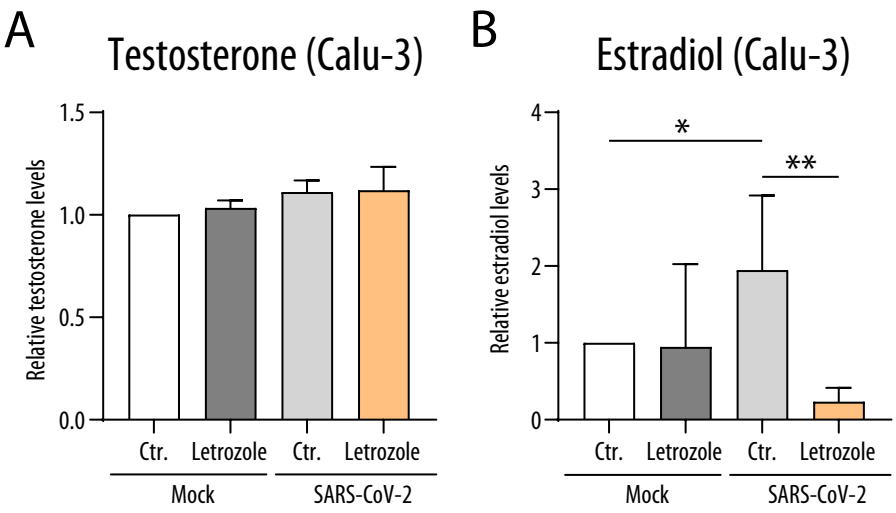

Figure S8. CYP19A1 activity in human lung cells upon SARS-CoV-2 infection, Related to Figure 6.

Testosterone (A) and estradiol (B) levels were measured in supernatants of Calu-3 cells either mock-infected (PBS) or infected with SARS-CoV-2 (MOI 0.01). After 24 h p.i., cells were treated with testosterone (100 nM) and the CYP19A1 inhibitor letrozole (1 μM) or as a control with DMSO (Ctr.). Samples were collected and analyzed 24 h post treatment. Shown is a merge of two to three independent biological replicates, each performed in technical triplicates. Values are shown as means; error bars are shown as SD. Statistical significance was assessed by unpaired Student's t-test (*$p \leq 0.05$, **$p<0.01$).

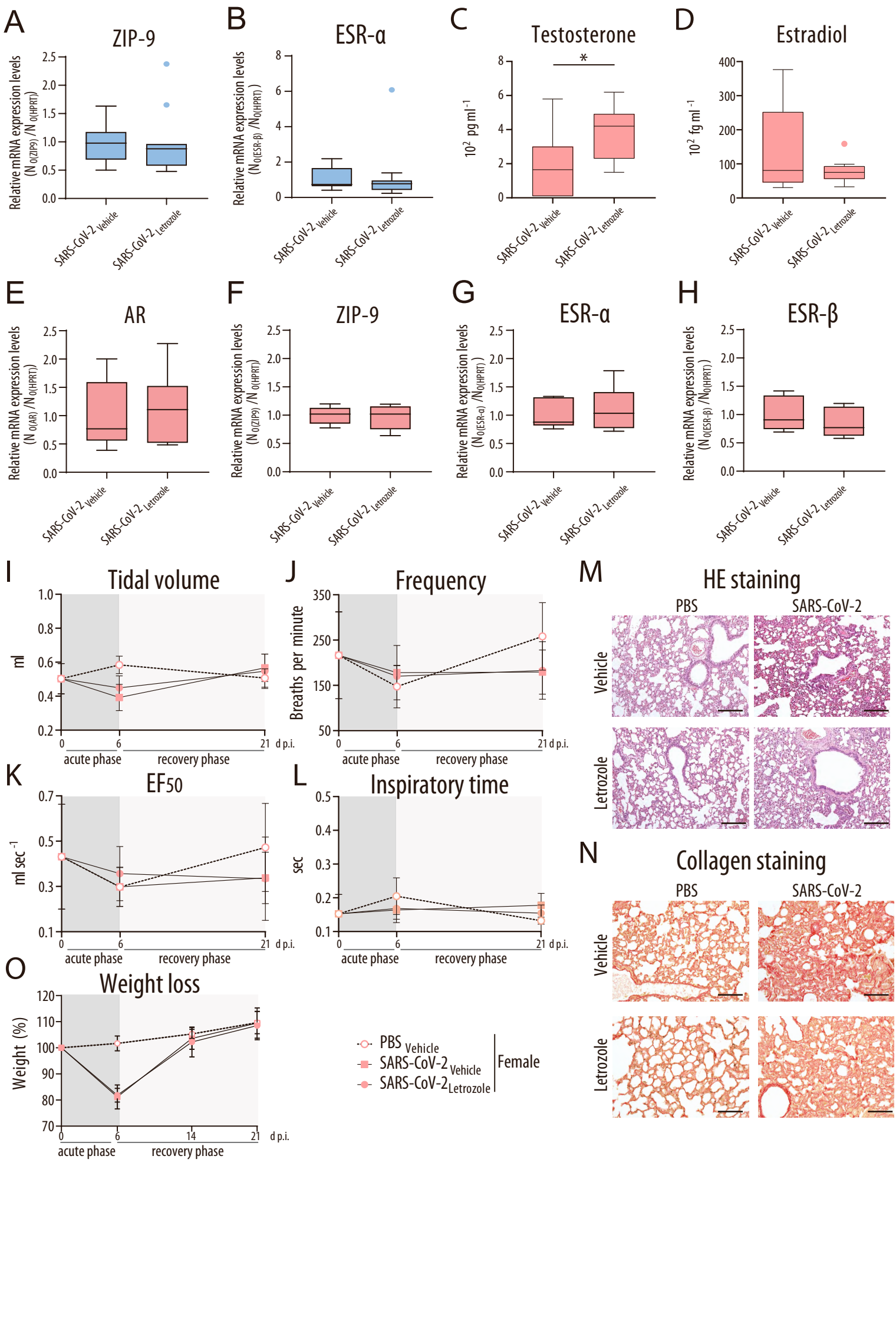
A
ZIP-9
Relative mRNA expression levels
B
ESR-α
C
Testosterone
D
Estradiol
E
AR
F
ZIP-9
G
ESR-α
H
ESR-β
SARS-CoV-2 Vehicle
SARS-CoV-2 Letrozole
I
Tidal volume
ml
J
Frequency
Breaths per minute
K
EF50
ml sec-1
L
Inspiratory time
sec
O
Weight loss
Weight (%)
acute phase
recovery phase
d p.i.
PBS Vehicle
SARS-CoV-2 Vehicle
SARS-CoV-2 Letrozole
Female
M
HE staining
PBS
SARS-CoV-2
Vehicle
Letrozole
N
Collagen staining

Figure S9. SARS-CoV-2 infected male and female hamsters treated with the CYP19A1 inhibitor letrozole, Related to Figure 6. (A, B) ZIP-9 (A) and ESR-α (B) mRNA expression levels measured in the lungs of SARS-CoV-2 infected male golden hamsters at day 6 p.i. (*n* = 11). SARS-CoV-2 infected and vehicle treated hamsters were set as 1. (C, D) Testosterone (C) and estradiol (D) levels were measured in SARS-CoV-2 infected female golden hamsters, treated either with vehicle or letrozole, at 3 d p.i. (*n* = 11). (E-H) AR (E), ZIP-9 (F), ESR-α (G) and ESR-β (H) mRNA expression levels measured in the lungs of SARS-CoV-2 infected female golden hamsters at day 6 p.i. (*n* = 6). SARS-CoV-2 infected and vehicle treated hamsters were set as 1 after normalization against HPRT. Data are shown as a box and whisker plot. (I-L) Whole-body plethysmography in control (PBS) or SARS-CoV-2 infected female golden hamsters, treated either with vehicle or letrozole: Tidal volume (I), frequency (J), EF50 (K) and inspiratory time (L) (*n* = 5-7; day 0 p.i. *n* = 12). (M, N) HE staining (M) or collagen staining with Sirius Red (N) of lung sections from control (PBS) or SARS-CoV-2 infected female golden hamsters, treated either with vehicle or letrozole, at 21 d p.i. Scale bar, 200 µm (M) or 100 µm (N) (*n* = 5-7 per group). (O) Weight loss of control (PBS) or SARS-CoV-2 infected female golden hamsters, treated either with vehicle or letrozole, over a time course of 21 days (*n* = 5-7 per group). (A-L, O) Values are shown as means; error bars are shown as SD. Statistical significance was assessed by Mann-Whitney test (*$p \leq 0.05$).

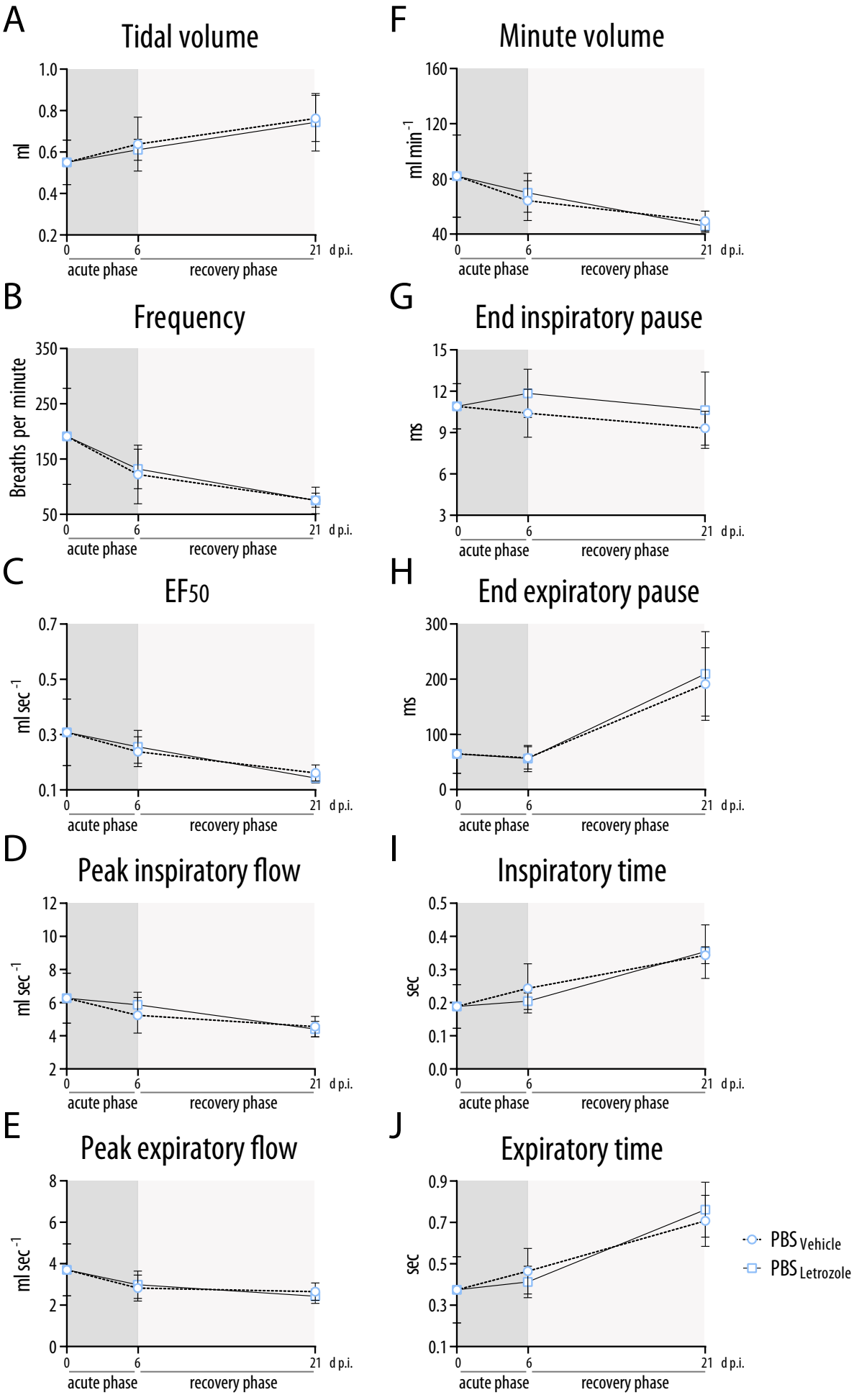
A
Tidal volume
ml
1.0
0.8
0.6
0.4
0.2
B
Frequency
Breaths per minute
350
250
150
50
C
EF50
ml sec-1
0.7
0.5
0.3
0.1
D
Peak inspiratory flow
ml sec-1
12
10
8
6
4
2
E
Peak expiratory flow
ml sec-1
8
6
4
2
0
F
Minute volume
ml min-1
160
120
80
40
G
End inspiratory pause
ms
15
12
9
6
3
H
End expiratory pause
ms
300
200
100
0
I
Inspiratory time
sec
0.5
0.4
0.3
0.2
0.1
0.0
J
Expiratory time
sec
0.9
0.7
0.5
0.3
0.1
0
6
21
d p.i.
acute phase
recovery phase
PBS Vehicle
PBS Letrozole

Figure S10. Lung plethysmography in PBS control infected male golden hamsters treated with the CYP19A1 inhibitor letrozole, Related to Figure 6.

Whole-body plethysmography assessment of lung function parameters in control (PBS) infected male hamsters, treated either with vehicle or letrozole, at the indicated time points (n = 5-7; day 0 p.i. n = 12): Tidal volume (A), frequency (B), EF50 (C), peak inspiratory flow (D), peak expiratory flow (E), minute volume (F), end inspiratory pause (G), end expiratory pause (H), inspiratory time (I) and expiratory time (J). Values are shown as means; error bars are shown as SD.

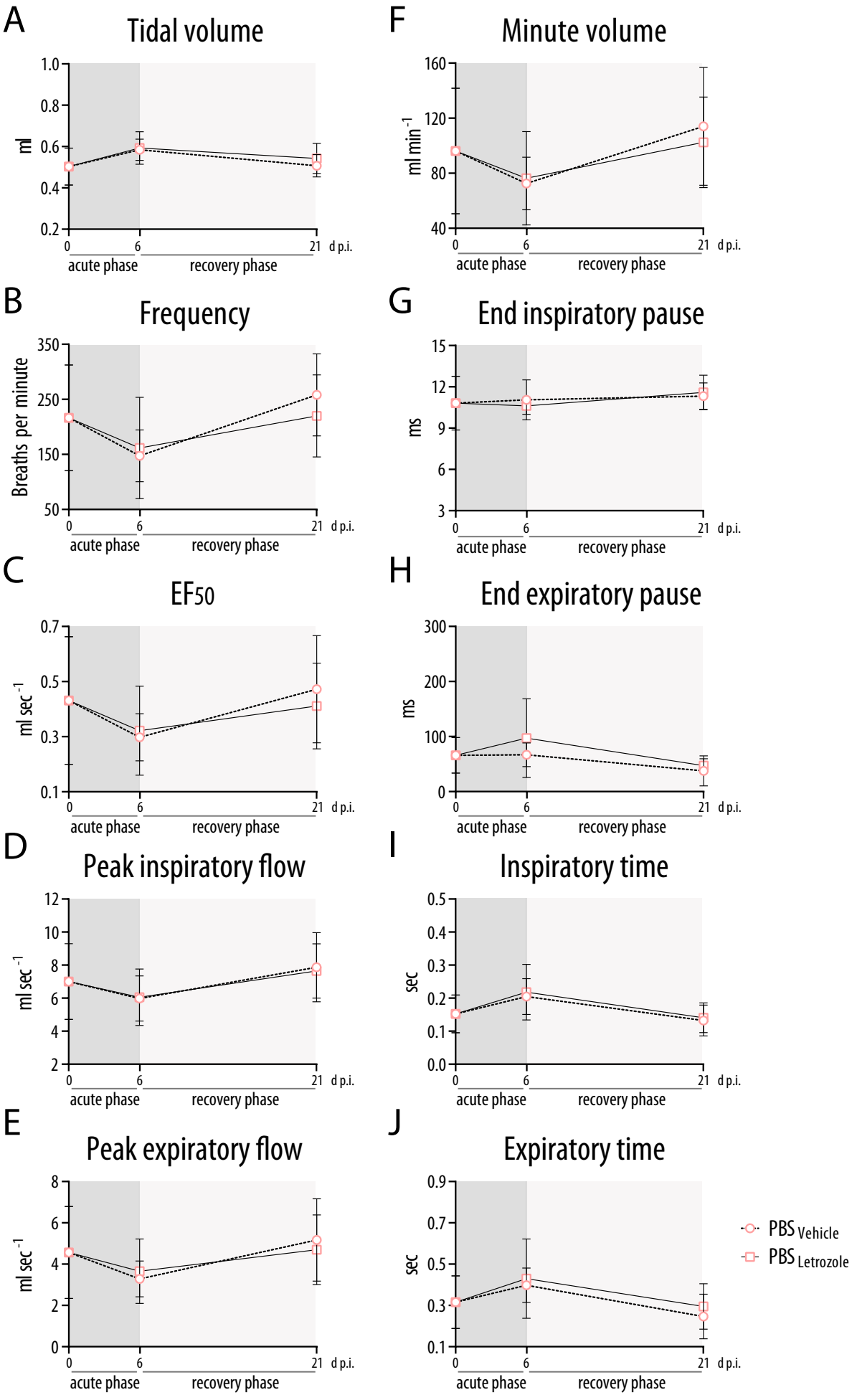
A
Tidal volume
ml
1.0
0.8
0.6
0.4
0.2
0
6
21
d p.i.
acute phase
recovery phase
F
Minute volume
ml min-1
160
120
80
40
B
Frequency
Breaths per minute
350
250
150
50
G
End inspiratory pause
ms
15
12
9
6
3
C
EF50
ml sec-1
0.7
0.5
0.3
0.1
H
End expiratory pause
ms
300
200
100
0
D
Peak inspiratory flow
ml sec-1
12
10
8
6
4
2
I
Inspiratory time
sec
0.5
0.4
0.3
0.2
0.1
0.0
E
Peak expiratory flow
ml sec-1
8
6
4
2
0
J
Expiratory time
sec
0.9
0.7
0.5
0.3
0.1
PBS Vehicle
PBS Letrozole

Figure S11. Lung plethysmography in PBS control infected female golden hamsters treated with the CYP19A1 inhibitor letrozole, Related to Figure 6.

Whole-body plethysmography assessment of lung function parameters in control (PBS) infected female hamsters, treated either with vehicle or letrozole, at the indicated time points (n = 5-7; day 0 p.i. n = 12): Tidal volume (A), frequency (B), EF50 (C), peak inspiratory flow (D), peak expiratory flow (E), minute volume (F), end inspiratory pause (G), end expiratory pause (H), inspiratory time (I) and expiratory time (J). Values are shown as means; error bars are shown as SD.

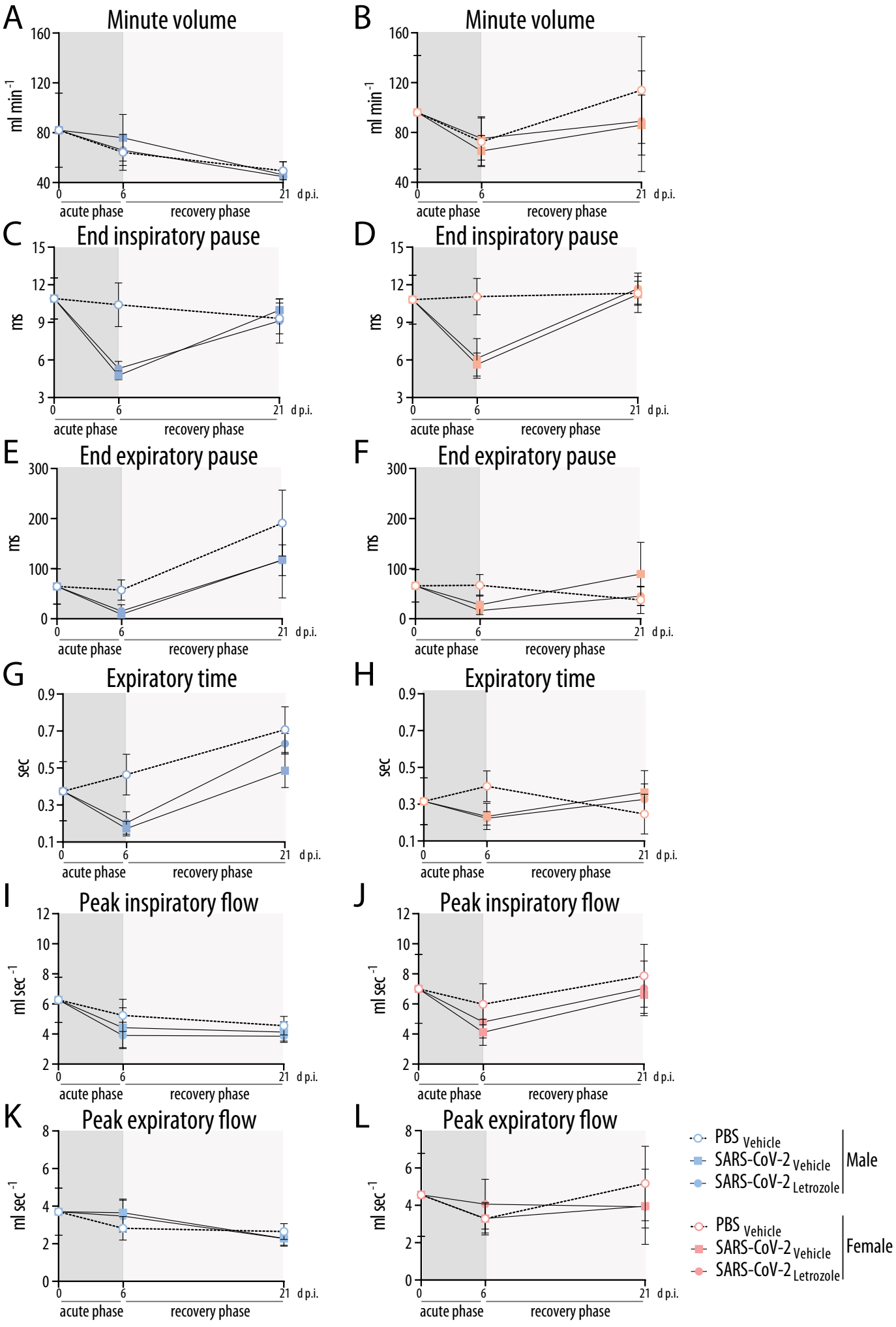
A
Minute volume
ml min-1
160
120
80
40
0
6
21
d p.i.
acute phase
recovery phase
B
Minute volume
C
End inspiratory pause
ms
15
12
9
6
3
D
End inspiratory pause
E
End expiratory pause
300
200
100
0
F
End expiratory pause
G
Expiratory time
sec
0.9
0.7
0.5
0.3
0.1
H
Expiratory time
I
Peak inspiratory flow
ml sec-1
12
10
8
6
4
2
J
Peak inspiratory flow
K
Peak expiratory flow
L
Peak expiratory flow
PBS Vehicle
SARS-CoV-2 Vehicle
SARS-CoV-2 Letrozole
Male
PBS Vehicle
SARS-CoV-2 Vehicle
SARS-CoV-2 Letrozole
Female

Figure S12. Lung plethysmography in SARS-CoV-2 infected male and female golden hamsters treated with the CYP19A1 inhibitor letrozole, Related to Figure 6.

Whole-body plethysmography assessment of lung function parameters in SARS-CoV-2 infected or control (PBS) infected male (A, C, E, G, I, K) and female hamsters (B, D, F, H, J, L), treated either with vehicle or letrozole, at the indicated time points (n = 5-7; day 0 p.i. n = 12): Minute volume (A, B), end inspiratory pause (C, D), end expiratory pause (E, F), expiratory time (G, H), peak inspiratory flow (I, J) and peak expiratory flow (K, L). Values are shown as means; error bars are shown as SD.

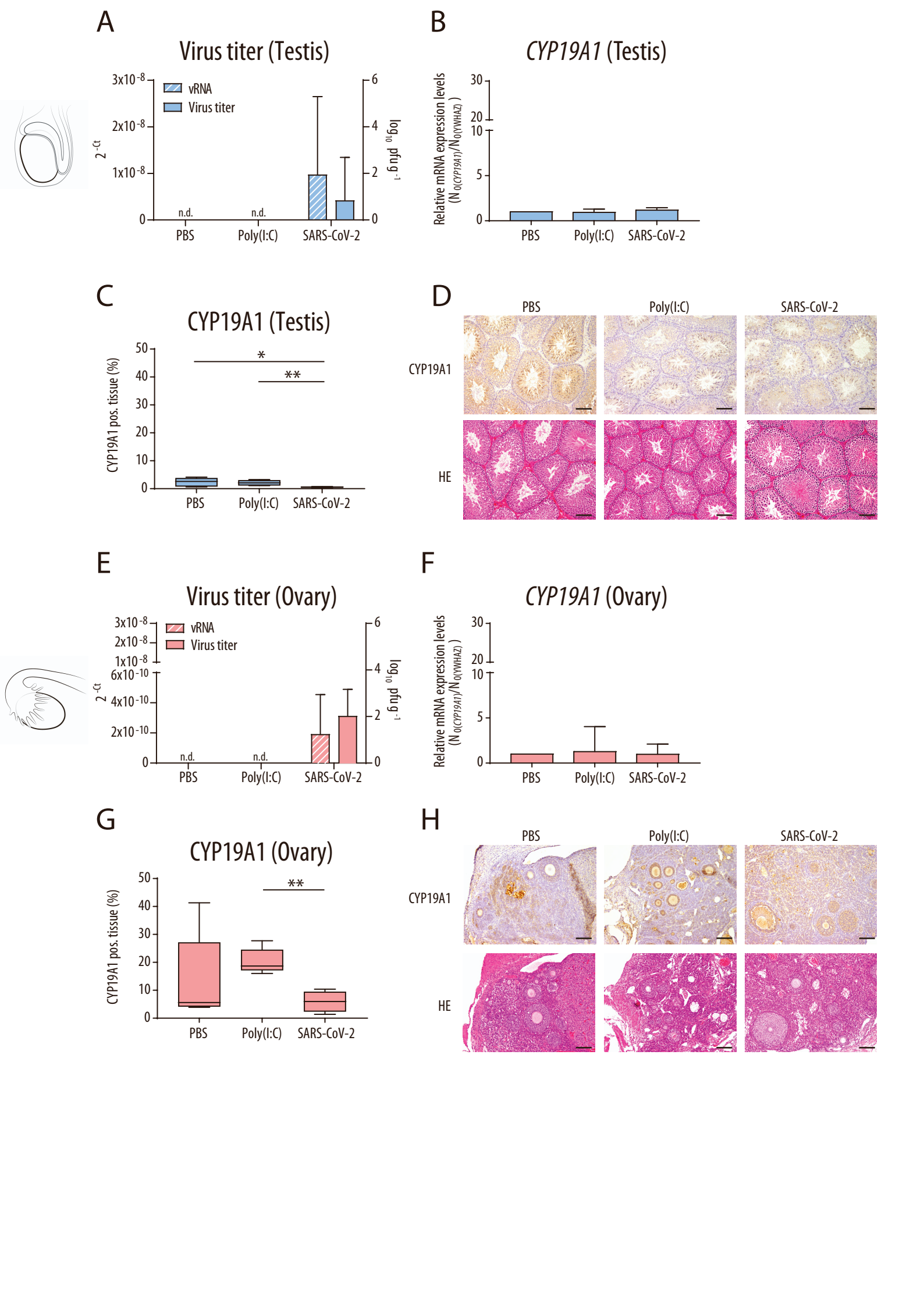
A
Virus titer (Testis)
vRNA
Virus titer
2-Ct
log10 pfu g-1
n.d.
n.d.
PBS
Poly(I:C)
SARS-CoV-2
B
CYP19A1 (Testis)
Relative mRNA expression levels
C
CYP19A1 (Testis)
CYP19A1 pos. tissue (%)
*
**
D
CYP19A1
HE
E
Virus titer (Ovary)
F
CYP19A1 (Ovary)
G
CYP19A1 (Ovary)
H

Figure S13. Virus titer and CYP19A1 expression in the gonads of SARS-CoV-2 infected male and female golden hamsters, Related to Figure 3.

(A, E) Viral mRNA and virus titer detected in the testis of SARS-CoV-2 infected and control treated (PBS, Poly(I:C)) male (A) and ovaries of female (E) golden hamsters at day 3 d p.i. (n = 5). n.d., not detectable. (B, F) CYP19A1 mRNA expression levels measured in the testis of SARS-CoV-2 infected and control treated (PBS, Poly(I:C)) male (B) and ovaries of female (F) golden hamsters at day 3 p.i. (n = 5). Relative CYP19A1 mRNA expression values in PBS treated hamsters were set to 1 after normalization against YWHAZ. (C, G) Quantification of CYP19A1 protein expressing tissue in the testis of SARS-CoV-2 infected and control treated (PBS, Poly(I:C)) male (C) and ovaries of female (G) golden hamsters at day 3 p.i. (n = 5). (D, H) CYP19A1 protein expression detected by immunohistochemistry in the testis of SARS-CoV-2 infected and control treated (PBS, Poly(I:C)) male (D) and ovaries of female (H) golden hamsters. Consecutive slides were also stained with HE. Representative pictures of each group are shown (n = 5). Scale bar, 100 µm. (A, B, E, F) Values are shown as means; error bars are shown as SD. (C,G) Values are shown as a box and whisker plot. Statistical significance was assessed by one-way ANOVA (*$p \leq 0.05$, **$p<0.01$).

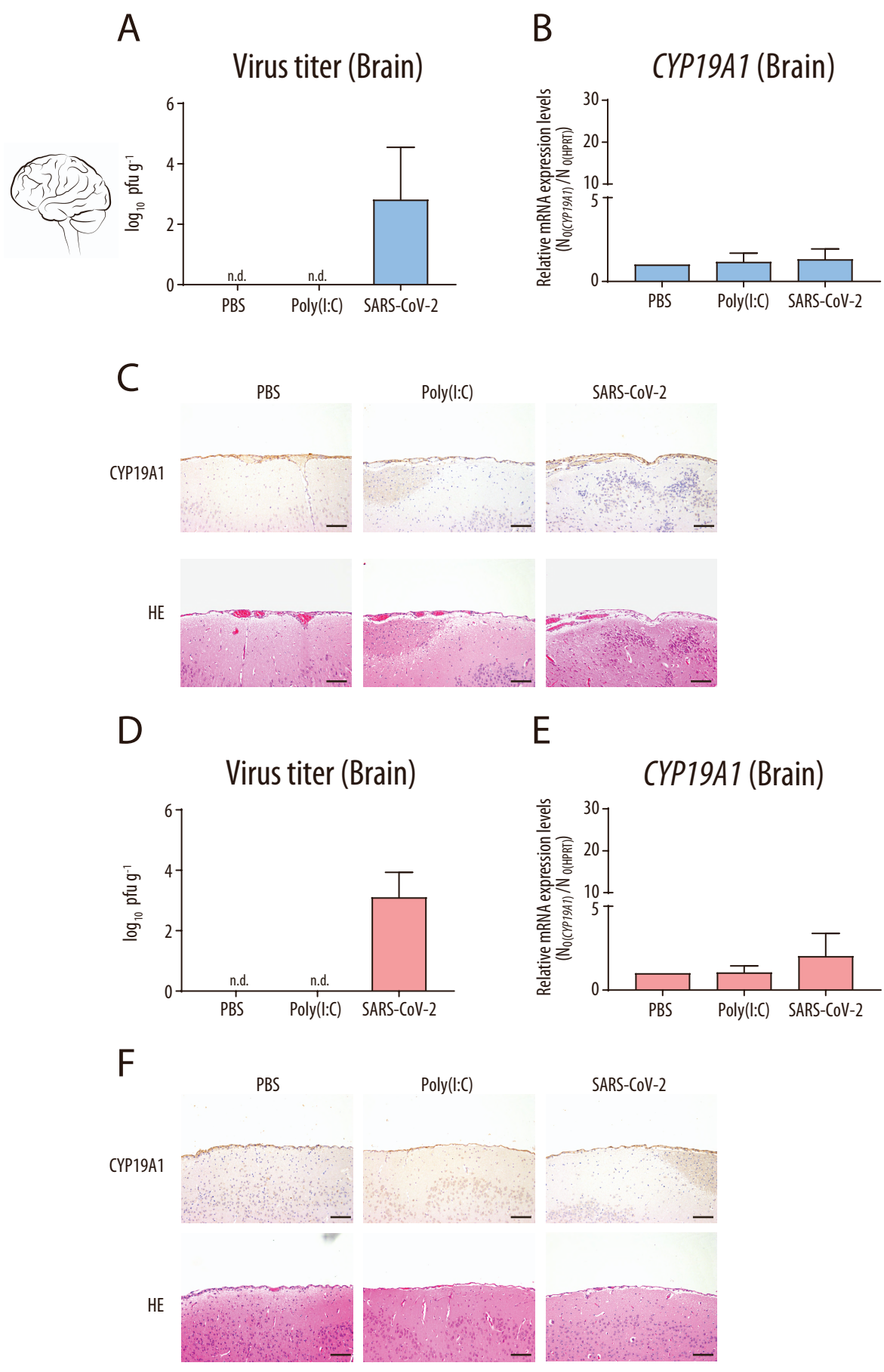
A
Virus titer (Brain)
log10 pfu g-1
6
4
2
0
n.d.
n.d.
PBS
Poly(I:C)
SARS-CoV-2
B
CYP19A1 (Brain)
Relative mRNA expression levels
(N0(CYP19A1)/N0(HPRT))
30
20
10
5
0
PBS
Poly(I:C)
SARS-CoV-2
C
PBS
Poly(I:C)
SARS-CoV-2
CYP19A1
HE
D
Virus titer (Brain)
log10 pfu g-1
6
4
2
0
n.d.
n.d.
PBS
Poly(I:C)
SARS-CoV-2
E
CYP19A1 (Brain)
Relative mRNA expression levels
(N0(CYP19A1)/N0(HPRT))
30
20
10
5
0
PBS
Poly(I:C)
SARS-CoV-2
F
PBS
Poly(I:C)
SARS-CoV-2
CYP19A1
HE

Figure S14. Virus titer and CYP19A1 expression in the brains of SARS-CoV-2 infected male and female golden hamsters, Related to Figure 3.

(A, D) Virus titer detected in the brains of SARS-CoV-2 infected and control treated (PBS, Poly(I:C)) male (A) and female (D) golden hamsters at day 3 p.i. (*n* = 5). n.d., not detectable. (B, E) CYP19A1 mRNA expression levels measured in the brains of SARS-CoV-2 infected and control treated (PBS, Poly(I:C)) male (B) and female (E) golden hamsters at day 3 p.i. (*n* = 5). Relative CYP19A1 mRNA expression values in PBS treated hamsters were set to 1 after normalization against HPRT. (C, F) CYP19A1 protein expression detected by immunohistochemistry in the brains of SARS-CoV-2 infected and control treated (PBS, Poly(I:C)) male (C) and female (F) golden hamsters. Consecutive slides were also stained with HE. Representative pictures of each group are shown (*n* = 5). Scale bar, 100 μm. (A, B, D, E) Values are shown as means; error bars are shown as SD.

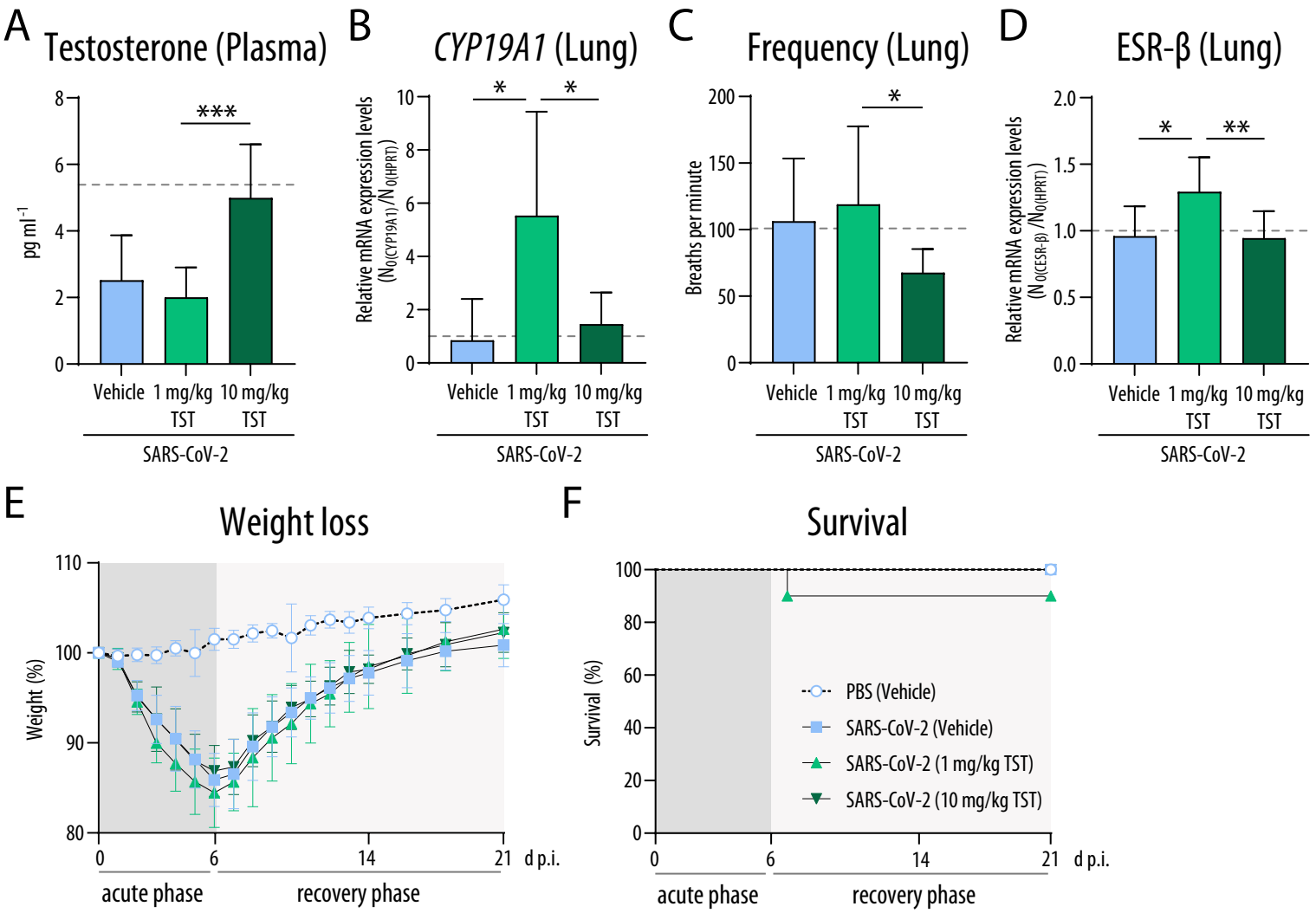

Figure S15. Effect of testosterone treatment on CYP19A1 expression and SARS-CoV-2 pathogenesis in male golden hamsters, Related to Figures 3, 4 and 5.

Male golden hamsters were infected with SARS-CoV-2 and either treated with vehicle, 1mg/kg or 10 mg/kg testosterone (TST). As control, male golden hamsters were inoculated with PBS and treated with vehicle (grey dash line). (A-D) Testosterone levels (A), CYP19A1 mRNA expression levels in the lungs (B), frequency as a lung function parameter measured by whole-body plethysmography (C) and ESR-β mRNA expression levels in the lungs (D) were determined in all groups at day 21 p.i. (n = 10; SARS-CoV-2 treated with 1 mg/kg TST: n = 9). (B, D) Relative CYP19A1 and ESR-β mRNA expression values in PBS and vehicle treated hamsters were set to 1 after normalization against HPRT. (E, F) weight loss (E) and survival (F) of control treated as well as SARS-CoV-2 infected and TST treated male golden hamsters over a time course of 21 days (n = 10 per group). Values are shown as means; error bars are shown as SD. Statistical significance was assessed by unpaired Student´s t-test (*p ≤ 0.05, **p<0.01, ***p<0.001).

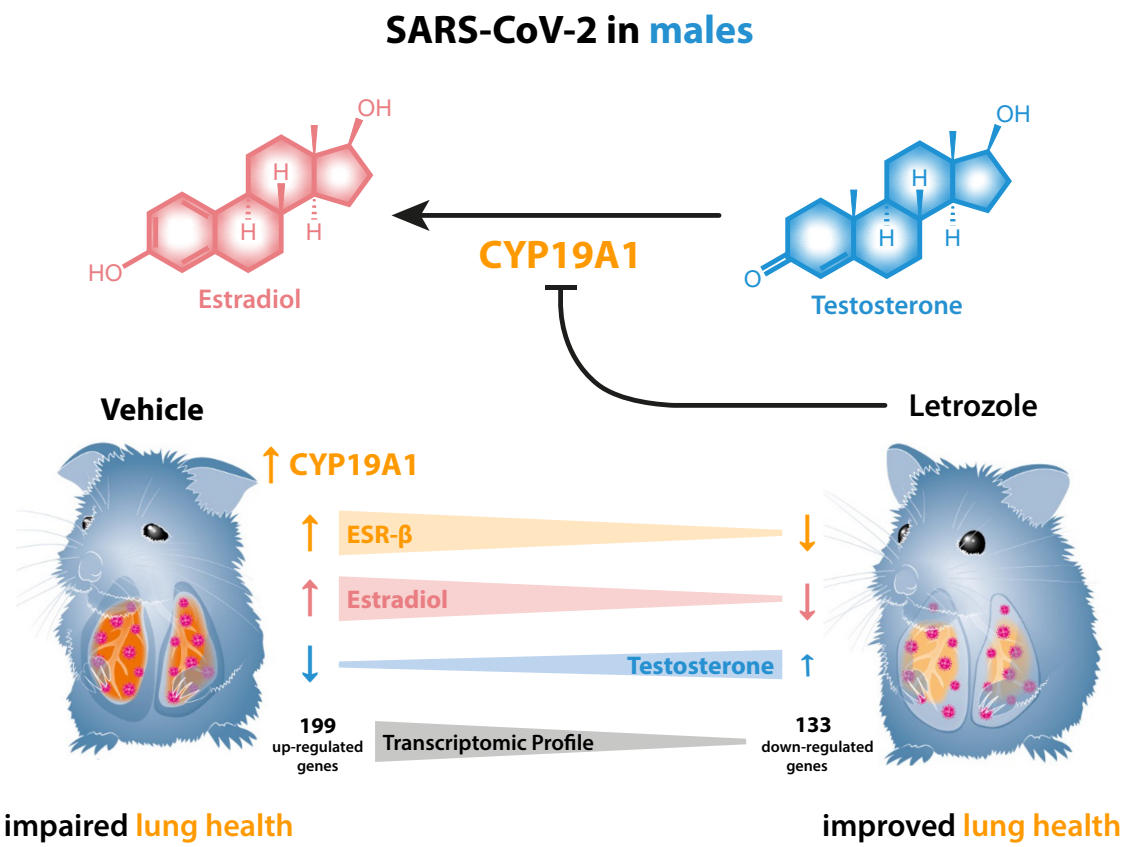

Figure S16. Summary Model: Letrozole mediated improved lung health in SARS-CoV-2 infected males, Related to Figure 6. Treatment of hamsters with the CYP19A1 inhibitor letrozole results in reduced estradiol and ESR-ß levels, while testosterone levels are elevated. Letrozole treatment results in the downregulation of 133 genes in SARS-CoV-2 infected males, as compared to the SARS-CoV-2 infected, vehicle-treated control group. In summary, reduced estradiol levels, reduced ESR-ß expression and elevated testosterone levels are associated with improved overall lung health in SARS-CoV-2 infected, letrozole-treated male hamsters.